Titre: Title:	3D Printing of Multifunctional Chitosan-Based Hydrogels and Nanocomposites
Auteur: Author:	Qinghua Wu
Date:	2018
Type:	Mémoire ou thèse / Dissertation or Thesis
Référence: Citation:	Wu, Q. (2018). 3D Printing of Multifunctional Chitosan-Based Hydrogels and Nanocomposites [Thèse de doctorat, École Polytechnique de Montréal]. PolyPublie. https://publications.polymtl.ca/3176/

Document en libre accès dans PolyPublie
Open Access document in PolyPublie

URL de PolyPublie: PolyPublie URL:	https://publications.polymtl.ca/3176/
Directeurs de recherche: Advisors:	Marie-Claude Heuzey, & Daniel Therriault
Programme: Program:	Génie chimique

UNIVERSITÉ DE MONTRÉAL

3D PRINTING OF MULTIFUNCTIONAL CHITOSAN-BASED HYDROGELS AND
NANOCOMPOSITES

QINGHUA WU

DÉPARTEMENT DE GÉNIE CHIMIQUE

ÉCOLE POLYTECHNIQUE DE MONTRÉAL

THÈSE PRÉSENTÉE EN VUE DE L'OBTENTION

DU DIPLÔME DE PHILOSOPHIAE DOCTOR

(GÉNIE CHIMIQUE)

JUIN 2018

UNIVERSITÉ DE MONTRÉAL

ÉCOLE POLYTECHNIQUE DE MONTRÉAL

Cette thèse intitulée :

3D PRINTING OF MULTIFUNCTIONAL CHITOSAN-BASED HYDROGELS AND
NANOCOMPOSITES

présentée par : WU Qinghua

en vue de l'obtention du diplôme de : Philosophiae Doctor

a été dûment acceptée par le jury d'examen constitué de :

M. LABERGE LEBEL Louis, Ph. D., président

Mme HEUZEY Marie-Claude, Ph. D., membre et directrice de recherche

M.THERRIAULT Daniel, Ph. D., membre et codirecteur de recherche

M. ABDELLAH Ajji, Ph. D., membre

Mme DEMARQUETTE Nicole Raymonde, Ph. D., membre externe

DEDICATION

"Stay foolish, for fun."

ACKNOWLEDGEMENTS

RÉSUMÉ

La capacité de produire des micro- ou nanostructures complexes dans des matériaux mous est importante pour diverses applications telles que l'ingénierie tissulaire, les capteurs, l'administration de médicaments et les dispositifs médicaux. Dans les tissus vivants, les micro-environnements peuvent affecter l'alignement et l'organisation des cellules, conduisant à la complexité structurelle et fonctionnelle des tissus natifs. Les hydrogels d'origine naturelle sont une classe de matières molles qui sont exceptionnellement attrayantes pour les applications biomédicales, car ils simulent l'environnement aqueux des matrices extracellulaires. Cependant, des structures d'hydrogel d'origine naturelle contrôlées avec précision sont difficiles à obtenir par la plupart des méthodes de fabrication classiques, et même avec la fabrication additive. Malgré les progrès récents dans le domaine de la fabrication additive, des défis importants persistent pour fabriquer des hydrogels avec des structures ordonnées et des propriétés mécaniques et biologiques adéquates pour imiter les tissus natifs.

En outre, les déchets électroniques et la pollution environnementale constituent un problème sérieux en raison de la demande constante d'appareils électroniques plus récents et plus puissants. De nombreux polymères et composants toxiques non biodégradables sont présents dans l'électronique traditionnelle (tels que les condensateurs et les circuits intégrés), et des solvants toxiques (tels que l'isopropanol, l'acétone et le trichloréthylène) sont parfois utilisés dans leur fabrication. Avec l'importance croissante du développement durable, il est de la plus haute priorité pour les entreprises de l'industrie électronique de développer et de fabriquer une électronique respectueuse de l'environnement. Les nano-composites à base de polymères naturels sont d'excellents candidats pour développer la nouvelle génération d'électronique responsable grâce à leur légèreté, durabilité et leur bas coûts. Ainsi, dans ce travail, nous développons un procédé d'impression 3D pour fabriquer des microstructures complexes de polymère naturel, le chitosane, (CS) et de ses nanocomposites.

Ce travail propose des encres à base de CS qui peuvent être fabriquées par impression 3D à température ambiante. La configuration de l'impression 3D est composée d'une étape de translation contrôlée par ordinateur et d'une plate-forme de positionnement à trois axes. L'encre est chargée dans une seringue, qui peut être extrudée à travers une microbuse. Les filaments d'encre sont

déposés sur la plaque pour former une structure couche par couche, où elle subit la solidification du filament par évaporation du solvant aqueux.

Nous démontrons une caractérisation complète des propriétés des encres CS pour l'impression 3D à température ambiante. Les propriétés rhéologiques des encres CS sont analysées par rhéométrie rotationnelle à taux de cisaillement faible et modéré et la viscosité apparente et le comportement en écoulement sont caractérisés par une analyse en rhéométrie capillaire, afin de concevoir une encre aux propriétés rhéofluidifiante pour une impression 3D réussie. Des tests d'évaporation de solvant de différentes compositions d'encre sont menés en observant la réduction de poids des filaments CS extrudés au cours du temps. Puisque différentes structures fabriquées par impression 3D nécessitent des paramètres de traitement particuliers, une cartographie de procédé est créée en prenant en compte des paramètres tels que le diamètre de la microbuse et la concentration d'encre, pour la fabrication réussie de structures CS unidimensionnelles (1D), bidimensionnelles (2D) et tridimensionnelles (3D). Les résultats de la diffraction aux rayons X (XRD) et des propriétés en traction des filaments CS sont également étudiés, montrant différentes propriétés du matériau obtenues après différentes étapes de traitement.

Les échafaudages imprimés en 3D montrent des formes de pores contrôlables (tels que des pores en forme de gradient, carrés et en forme de losange) et une haute résolution de 30 µm. Des échafaudages d'hydrogel microstructurés à surface ridée sont obtenus par une étape de gélification par neutralisation dans l'hydroxyde de sodium. Les échafaudages imprimés et neutralisés montrent des comportements très flexibles et extensibles. La déformation à la rupture des filaments d'hydrogel CS atteint jusqu'à ~ 400% et la résistance maximale est de ~ 7.5 MPa. Les hydrogels microstructurés peuvent guider la croissance des cellules fibroblastiques et induire l'alignement des cellules.

De plus, des nanocomposites constitués de CS en tant que matrice polymère, de nanotubes de carbone à parois multiples (CNT) en tant que nano-renfort et d'un mélange de solvants sont préparés en utilisant un procédé de mélange par broyeur à billes. Les encres nanocomposites CS/CNT sont développées pour présenter une auto-réparation à température ambiante. Les propriétés curatives peuvent être traitées par l'exposition à la vapeur d'eau et le nanocomposite peut restaurer la conductivité électrique et les propriétés mécaniques. L'auto-réparation est rapide, se produisant en quelques secondes après l'endommagement du nanocomposite. L'impression 3D

nous permet de fabriquer des nanocomposites CS/CNT très conducteurs (~ 1450 S/m). L'impression 3D assistée par instabilité est aussi développée pour fabriquer des fibres CS/CNT microstructurées hautement acdaptables, en raison de l'instabilité de l'enroulement de la corde liquide. Des fibres CS/CNT microstructurées présentant des liaisons sacrificielles et une longueur cachée permettent aux nanocomposites d'être très extensibles (déformation à la rupture de ~ 180%). L'extensibilité et la conductivité électrique élevées des fibres CS/CNT permettent de concevoir des capteurs portables. Les capteurs de contrainte personnalisés sont fabriqués par impression 3D assistée par instabilité et ont démontré leur capacité à détecter les mouvements du coude humain. Le nanocomposite CS/CNT peut également être utilisé pour détecter l'humidité due au gonflement du polymère sous une humidité différente de l'environnement.

La nouvelle méthode d'impression 3D d'hydrogels CS et de nanocomposites CS/CNT présentée ici ouvre de nouvelles portes pour concevoir et produire des structures tissulaires 3D à compatibilité topographique, biologique et mécanique ainsi que pour des applications de capteurs de déformations ou d'humidité.

ABSTRACT

The ability to produce complex micro- or nano-structures in soft materials is significant for various applications such as tissue engineering, sensors, drug delivery and medical devices. In tissues or organs, surrounding micro-environments can affect cell alignment and organization that lead to the biological and functional complexity of native tissues. Naturally derived hydrogels are an important class of soft materials, which are exceptionally attractive for biomedical applications since they simulate the aqueous environment of extracellular matrices. However, precisely controlled architectures of naturally derived hydrogels are difficult to obtain through most conventional fabrication methods, and even with three-dimensional (3D) printing. Despite recent progress in the field of additive manufacturing, significant challenges persist to fabricate hydrogels with ordered structures and adequate mechanical and biological properties for mimicking native tissues.

Besides, electronic waste and environmental pollution is a serious issue due to constant demand for newer and more powerful electronics. Many non-biodegradable polymers and toxic components are found in traditional electronics (such as capacitors and integrated circuits), and toxic solvents (such as isopropanol, acetone and trichloroethylene) are on occasion used in their fabrication. With the growing importance of sustainable development, it is of the upmost priority for companies in the electronic industry to develop and fabricate eco-friendly electronics. Natural polymer-based nanocomposites are excellent candidates for developing the next-generation of bio-sustainable electronics due to their lightweight, low-cost, and sustainable properties. Thus, in this work, we develop a 3D printing process to fabricate 3D microstructures of a natural polymer - namely chitosan (CS) - and its nanocomposites.

This work proposes CS-based inks that can be fabricated by 3D printing at room temperature. The setup of 3D printing is composed of a computer-controlled translation stage and a three-axis positioning platform. The ink is loaded into a syringe, which can be extruded through a micronozzle. The ink filaments are deposited on the plate to form a structure in a layer-by-layer manner, where it undergoes filament solidification through solvent evaporation.

We demonstrate a comprehensive characterization of the properties of CS inks for 3D printing at room temperature. The rheological properties of CS inks are analyzed by rotational rheometry at low to moderate shear rate and the process-related viscosity and flow behavior are characterized

by capillary flow analysis, in order to formulate inks with shear thinning behavior for successful 3D printing. Solvent evaporation tests of different ink compositions are investigated by observing the weight reduction of extruded CS filaments with time. Since different structures fabricated by 3D printing require different processing parameters, a processing map is generated by considering parameters such as micronozzle diameter and ink concentration for the successful fabrication of one-dimensional (1D), two-dimensional (2D) and 3D CS structures. The results of X-ray diffraction (XRD) and tensile properties of CS filaments are also investigated, showing different material properties obtained after different processing steps.

The 3D-printed scaffolds show controllable pore shapes (such as gradient, square- and diamond-shaped pores) and a high resolution of 30 µm. Microstructured hydrogel scaffolds with wrinkled surface are obtained through a gelation step of neutralization in sodium hydroxide. The as-printed and neutralized scaffolds show highly flexible and stretchable behaviors. The strain at break of CS hydrogel filaments reaches up to ~ 400% and maximum strength is ~ 7.5 MPa. The microstructured hydrogels can guide fibroblast cell growth and induce cell alignment.

Further, CS-based nanocomposites made of CS as a polymer matrix, multi-walled carbon nanotube (CNT) as a nanofiller and a solvent mixture are prepared using a ball mill mixing method. The CS/CNT nanocomposite inks are developed to exhibit self-healing at room temperature. The healing properties can be processed via exposure to water vapor and the nanocomposite can restore electrical conductivity and mechanical properties. The self-healing is rapid, occurring within seconds after the damage of the nanocomposite. 3D printing enables us to fabricate highly conductive (~ 1450 S/m) CS/CNT nanocomposites. Instability-assisted 3D printing is developed to fabricate high tunable microstructured CS/CNT fibers, due to the liquid rope coiling instability. Microstructured CS/CNT fibers featuring sacrificial bonds and hidden length allow the nanocomposites with high stretchability (strain at break of ~ 180%). The high stretchability and conductivity of CS/CNT fibers enable the nanocomposite to be designed as wearable sensors. The customized strain sensors are fabricated by instability-assisted 3D printing and demonstrate their ability to detect human elbow motions. The CS/CNT nanocomposite can be also used to sense the humidity owing to polymer swelling under different environment humidity.

The novel 3D printing method of tailoring CS hydrogels and CS/CNT nanocomposites demonstrated here opens new doors to design and produce 3D tissue constructs with topographical,

biological, and mechanical compatibility as well as wearable sensor exhibiting strain and humidity sensing ability.

TABLE OF CONTENTS

LIST OF TABLES

LIST OF FIGURES

LIST OF SYMBOLS AND ABBREVIATIONS

3D   three-dimensional

CS   chitosan

TE   tissue engineering

CNTs   carbon nanotubes

DDA   degree of N-deacetylation

PVA   poly(vinly alcohol)

HPN   hybrid polymer networks

IPN   interpenetrating networks

MWCNT   multi-walled carbon nanotubes

SWCNT   single-walled carbon nanotubes

PLA   polylactic acid

CA   classifications

HM   healing mechanism

HC   healing conditions

CD   conductivity

RM   recovery of mechanical property

RE   recovery of electrical property

CO_2 carbon dioxide

PCL   polycaprolactone

2D   two-dimensional

SEM   scanning electron microscope

PEO   poly(ethylene oxide)

SLA   stereolithography

SLS	selective laser sintering
FDM	fused deposition modelling
M	polymer matrix
NF	nanofillers
PM	processing methods
F	flexibility
SB	stretchability
SF	self-healing
CPN	conductive polymer-based nanocomposites

CHAPTER 1   INTRODUCTION

Background and problematic

The shortage of transplantable organs has become a national crisis and has the disadvantages of high costs, risks of infections from donor pathogens, and graft rejection by the immune system [1, 2]. To overcome these issues, tissue engineering (TE) is emerging as a revolutionary strategy which seeks to restore degenerated or damaged tissues. A particularly appealing strategy in TE is to combine the host's own cells with polymer based scaffolds [3]. Tissue-engineered scaffolds should be biodegradable, biocompatible, and have temporary mechanical support as well as customized structure [10], to mimic a certain degree of the complexity of native tissues or organs [4]. Natural polymers such as chitosan (CS) are attractive materials to engineer scaffolds, owing to their high cell compatibility [5]. However, CS normally presents weak mechanical properties, especially for its hydrated conditions [5, 6]. Porous CS scaffolds have been fabricated by techniques such as freeze drying and electrospinning, typically based on a random distribution of cells, matrix, and bioactive molecules [7-10]. Controllable cell-organization in scaffold is fascinating for TE to mimic the hierarchical structure of real tissues and organs such as muscles and bones [11-13].

Furthermore, natural polymers are also excellent candidates for developing next-generation of sustainable electronics owing to their lightweight, low-cost, non-toxic, biodegradability and renewable properties [14, 15]. Conductive fillers such as carbon nanotubes (CNTs) can be loaded into natural polymers to form conductive nanocomposites. Self-healing is also a desirable feature for designing electronic materials with the ability to heal damages and extend their lifetime. Self-healing nanocomposites could be used for a wide range of applications such as wearable devices [16, 17], biosensors, electronics [18] and soft robotics [19]. Nanocomposites used in wearable sensors such as strain sensors are mainly used as a thin film [20]. Nanocomposite sensors in a form of film are however not capable of demonstrating very high sensitivity [21].

3D printing, consisting of a computer-controlled translation stage, might address these issues. Recent advances in 3D printing have been developed to fabricate various materials such as ceramics [22], polylactic acid (PLA) fugitive inks [23], concentrated silk fibroin [24], colloidal suspensions, thermoplastic polymers [25] and hydrogels [26]. Natural polymers composed of polysaccharides and proteins are still challenging for 3D printing, since they may deform or

collapse during the printing process. Prior strategies used *in situ* gelling or low temperature to solidify the ink filament during the printing process [27-29]. However, they always involve a complicated fabrication process (using a bath or reservoir) and some crosslinkers used during fabrication may be cytotoxic. Several conductive nanocomposite inks have been developed so far [30-33]. However, these inks usually contain toxic organic solvents (e.g., dichloromethane) and/or toxic components. Thus, novel ink design and processing technologies with the dominance of simplicity and "green" processes should be developed for fabricating natural polymers such as CS and based nanocomposites for TE and electronic applications.

Organization of the thesis

This thesis is based on three articles submitted to scientific journals and consists of the following sections:

Chapter 2 provides a literature review on chitosan, its physiochemical properties and applications, on electrically conductive nanocomposites, various fabrication techniques used for CS, 3D printing methods used for natural polymers and nanocomposites and the applications of natural polymers and nanocomposites including TE and wearable devices. Chapter 3 states the research objectives and the coherence between the objectives and articles. The core results of this thesis, in the form of three peer reviewed scientific articles, are presented in the following three chapters. Chapter 4 includes a comprehensive study on the effect of fabrication parameters (applied pressure, robot velocity and nozzle diameter) and CS-related parameters (ink composition, solvent evaporation rate and rheological properties) on the printability and CS filament properties. Chapter 5 focuses on the development of CS inks used to fabricate CS scaffold by 3D printing. Microstructrured CS hydrogels are obtained and can guide cell growth and cell alignment. Chapter 6 shows the development of CS/CNT nanocomposites and investigates their electrical conductivy, along with self-healing and mechanical properties. The nanocomposite inks were used to fabricate microstructured fibers by instability-assisted 3D printing. Microstructured fibers were further developed as humidity and strain sensors. In Chapter 7, a general discussion of the entire thesis is presented. Finally Chapter 8 summarizes the conclusions and the recommendations for future work.

CHAPTER 2   LITERATURE REVIEW

2.1 Chitosan

Chitosan, a natural polymer, can be obtained from crustacean shells (chitin) and fungi [34]. As shown in Figure 2.1(a), it is semi-crystalline polysaccharide and composed of β(1→4) linked D-glucosamine residues with (1→4)-2-acetamido-2-deoxy-β-D-glucan (N-acetyl D-glucosamine) and (1→4) -2-amino-2-deoxy-β-D-glucan (D-glucosamine) units [35]. CS is more generally derived from chitin, which is the second most abundant natural amino polysaccharide, through N-deacetylation [14]. Chitin consists of β-(1→4)-N-acetyl-D-glucosamine units (Figure 2.1(b)). The degree of N-deacetylation (DDA) gives the number of amino groups on the skeleton of the CS chain, and the DDA should reach at least 60% for CS [36]. The physical characteristics of CS rely on some main factors: i.e. DDA, molecular weight (average and distribution), the purity, sequence of the acetamido and amino groups and so forth [37].
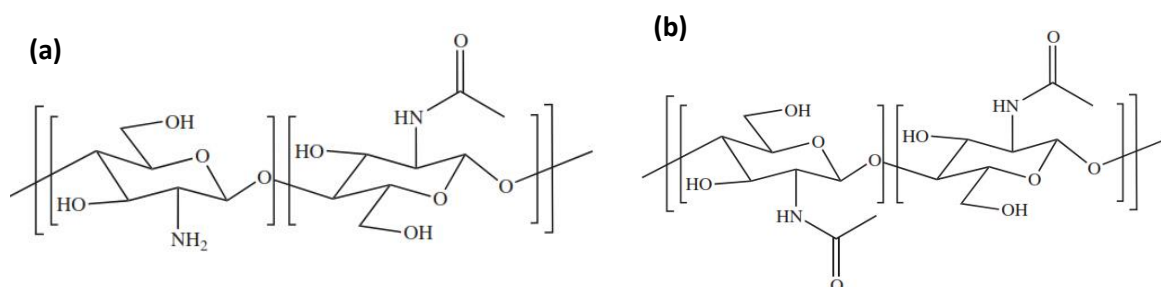
Figure 2.1: Structures of CS and chitin. a) CS, b) chitin [36].

Much of the potential of CS as a natural compound derives from its physiochemical characteristics. Firstly, the solubility of CS in aqueous solutions is poor due to its stable and crystalline structure, while it is soluble in acidic aqueous solutions below a pH of ~6 (pKa) as the free amino groups of CS can be protonated [38]. The pH-dependent solubility of CS allows the manufacturing process to fabricate products such as fibers and scaffolds [39].

Secondly, CS is the only positively-charged natural polymer with high charge density because of protonation, allowing it to form insoluble ionic complexes with a wide variety of water-soluble natural or synthetic anionic materials [40]. CS can combine with negatively charged drugs for drug delivery [41]. Additionally, the amino groups of CS can make it covalently cross-linked with other

materials [36], and functional groups on CS can be chemically or enzymatically modified to change its physical properties.

Finally, CS exhibits a wide variety of intrinsic properties. Briefly, CS is biodegradable: it can be degraded into non-toxic compounds and be metabolized by enzymes in human body like lysozyme [42], which makes it highly suitable to be implanted or injected in the body. CS is biocompatible providing affinity with cells and biomolecules. CS is also mucoadhesive and acts as an antibacterial agent [43], which makes it possible to use in wound healing [44]. All the interesting intrinsic properties mentioned above allow CS to be an outstanding candidate for biomedical applications.

2.1.1 Chitosan hydrogels

Hydrogels are three-dimensional hydrophilic polymeric networks swollen in water or biological fluids and contain chemical or physical cross-links [45]. Hydrogels can be formed from synthetic and natural polymers including hydrophilic homopolymers and copolymers [46]. CS, as a natural polymer, can form biological hydrogels with high water content that are bendable and soft, and they are capable of reducing the damage to the surrounding living organs or tissues for implantation [5].

2.1.2 Physical chitosan networks

Physically associated CS hydrogels present reversible gelation based on electrostatic interactions, hydrophobic interactions or hydrogen bonding instead of covalent interactions [6]. Protonated CS as a polycation can form physical networks with anionic components by ionic interactions and the formation can be affected by DDA, charge density, concentration and the size of negatively charged molecules [47]. Water-soluble non-ionic polymers are also capable of blending with CS to form hydrogels such as poly(vinly alcohol) (PVA) [48]. CS is capable of being gelled by itself without using any additives by neutralizing the amino groups [49]. Physical gelation of CS solutions was performed and explained by hydrophobic interactions and reduced solubility by adding β-glycerophosphate while heating at neutral pH [50]. CS can also be gelled by dissolving in certain types of acid solutions such as sulfuric acid, oxalic acid and phosphoric acid [51]. Physical CS hydrogels are more compatible without using toxic additives, but the mechanical properties are quite limited and it is difficult to precisely control the hydrogel pore sizes, dissolution and chemical functionalization [5].

2.1.3 Chemically cross-linked chitosan hydrogels

Chemically cross-linked CS networks can be classified into three categories: CS cross-linked alone, hybrid polymer networks (HPN) as well as full- or semi-interpenetrating networks (IPN) [42]. CS can be cross-linked by itself with cross-linkers, such as glutaraldehyde and genipin. The gelation reaction of chemical CS hydrogels is mainly dominated by cross-linkers [52]. Materials involved in HPN are mostly biomaterials that need to be biodegradable, biocompatible and bioadhesive. Semi-IPN contains a non-reacting polymer before cross-linking and is entrapped in CS networks, while full-IPN hydrogels are formed by a sequential strategy including the formation of semi-IPN [53]. Irreversible chemical hydrogels are more stable than physical hydrogels. However, toxic agents or catalyst involved may result in contamination.

2.2 Electrically conductive nanocomposites

2.2.1 Fundamentals of electrically conductive nanocomposites

Nanocomposites (at least one dimension in nanoscale from 1 to 100 nm) featuring electrical conductivity are attractive materials for wide applications such as energy storage [54], sensors and biomedical applications [55]. Electrically conductive nanofillers such as single-walled carbon nanotube (SWCNT), multi-walled carbon nanotube (MWCNT), graphene, metallic nanorods, have been used to fabricate nanocomposites with large surface area, electrical conductivity and nanostructures. As described by percolation theory [56], the nanofiller loading plays a significant role in the conductivity of nanocomposites. The conductivity of nanocomposites is very low (close to the insulative state) at a low nanofiller loading, since the distance of nanofillers in the nanocomposite is larger than the size of nanofillers [57]. A "percolation" pathway is formed by connected nanofillers to suddenly increase the conductivity by several orders of magnitude, when the nanofiller concentration reaches to a critical concentration (called percolation threshold).

Table 2.1 shows a collection of conductive nanocomposites prepared by different processing methods. The properties of nanocomposites can be affected by polymer matrix (M), the type of nanofillers (NF) and the processing methods (PM).

Table 2.1: Electrically conductive nanocomposites prepared by different processing methods

M^A	NF	Solvent	PM	CD (S/m)@C (wt %)	Structures	Applications	Ref.
SI	AgNP	DCM	Planetary centrifugal mixing	0.01@68	Hybrid scaffold	Tactile sensors	[58]
EP	MWCNT	No solvent	centrifugal vacuum mixing	148@0.66	Sponge	EMI shielding	[59]
EP	GNP	Acetone	CO2-assisted mixing	10^{-5}@12	-	-	[60]
PLA	MWCNT	DCM	Mechanical mixing and sonication	23@5	Freeform 3D helix	Liquid sensor	[31]
PLA	MWCNT	DCM	Ball mill mixing	3800@40	3D scaffold	Liquid sensor	[32]
PN	AgNW	Hydrogen chloride	Solution mixing	1.03×10^6	Film	-	[61]
CE	rGO	Methanol, acid hydrolysis	Solution mixing	1800@49.4, 5000@56.8	Membrane	-	[62]
EC	GR	Cyclohexanone/terpineol	Solution mixing sonication	25600@50	Film	Flexible electronics	[63]

AF	rGO	water	Mechanical stirring	510@66.7	Film	Enzyme sensing	[64]
GEL	rGO	Deionized water	Solution mixing	3.78@10	-	-	[65]
CS	MWCNT	Acetic acid, glycerol, ionic liquid	Solution mixing sonication	239@40, 3425@80,	Membrane	Actuator	[66]
CS	SWCNT	Acetic acid	Solution mixing	500@40	Membrane	Actuator	[67]
CS	rGO	Acetic acid	Ultrasonication	6.7	Lamellar structure	-	[68]
Our work	MWCNT	Acetic acid, lactic acid, citric acid	Ball mill mixing	1450@40	Microstructured fiber, scaffold	Sensors	

A: SI: silicone, EP: epoxy, PLA: polylactic acid, PN: polyaniline, CE: cellulose, EC: ethyl cellulose, GEL: gelatin, AF: amyloid fibril, GEL: gelatin, CS: chitosan, AgNP: silver nanoparticle, MWCNT: multi-wall carbon nanotube, AgNW: silver nanowire, GNP: graphene nanoplatelet, rGO: reduced graphene oxide, GR: graphene, SWCNT: single-wall carbon nanotube, DCM: dichloromethane

2.2.1 Effect of polymers

The type of polymers plays an important role on the electrical properties of nanocomposites. Some polymers show intrinsic conductivity such as polyaniline (PN) [61]. Therefore, nanocomposites prepared by conducting polymer can achieve excellent conductivity. As shown in Table 2-1, maximum conductivity of 1.03×10^6 S/m has been demonstrated in PN/AgNW nanocomposite film (thickness of ~ 2.5 μm for the AgNW layer and thickness of ~ 10 μm for the PN layer) at a AgNW areal density of 0.84 mg/cm^2. The PN/AgNW nanocomposite was prepared by solution mixing [61]. The polymer may also affect the percolation threshold, since polymer physical properties such as polarity, surface tension and crystallinity have an obvious effect on the

percolation threshold. For example, Nassira *et al.* demonstrated gelatin/graphene nanocomposite that present an ultralow percolation threshold 3.3×10^{-2} vol% [65], due to polymer properties and the processing method.

2.2.2 Effect of processing methods

The processing methods have an important effect on the dispersion, orientation, distribution and aspect ratio of nanofillers. Well-dispersed nanofillers in a polymer matrix is important for achieving excellent mechanical properties [63]. Optimized processing method is also necessary for obtaining low percolation threshold [65]. However, for the electrical conductivity, high concentrations of nanofiller play a significant role in obtaining high conductivity [69]. As shown in Table 2.1, solution mixing is the most popular method to prepare nanocomposites based on natural polymers.

Solution mixing allows preparing nanocomposites in three steps: dispersing nanofillers in a solvent, mixing the polymer and casting the nanocomposite as a film. This method always need sonication [67], ultrasonication [68] or mechanical stirring [64] to mix the solution. The selection of solvent is important to obtain well-dispersed nanocomposites. Lu *et al.* reported that well-dispersed CS/MWCNT nanocomposite was achieved by adding ionic liquid [66]. Toxic solvents such as methanol [62], cyclohexanone and terpineol [63] may be involved in the formation of nanocomposites, which is not compatible for industries since large amount of solvent needs to be evaporated during the process. Also, this processing method usually results in the structures of nanocomposites including a thin film or a fiber that is limited for potential applications. This method is great to mix polymer and nanofillers at low concentration, but it is not very suitable for processing the solution with high content of nanofillers.

Ball mill mixing is a class of grinding method, which use ceramic balls to mix the materials. The high shear stress generated between the rigid balls helps to disperse the nanofiller in the polymer matrix. It has been developed to produce nanocomposite with high content of nanofillers. For example, Chizari *et al.* reported PLA/MWCNT nanocomposites with high contents of MWCNTs (up to 40 wt %) formed by ball mill mixing for the application of liquid sensor [32].

2.2.3 Properties of CNT

Carbon nanotubes (CNTs), discovered by Sumio Iijima in 1991, are promising materials due to their superior electrical and mechanical properties [70]. They can be classified into two types: single-walled nanotube (SWCNT) that is made of a single graphite sheet enfolded into a tube (Figure 2.2 a-d); Multi-walled nanotube (MWCNT) that consists of concentrically arranged nanotubes (Figure 2.2 e-f) [71].
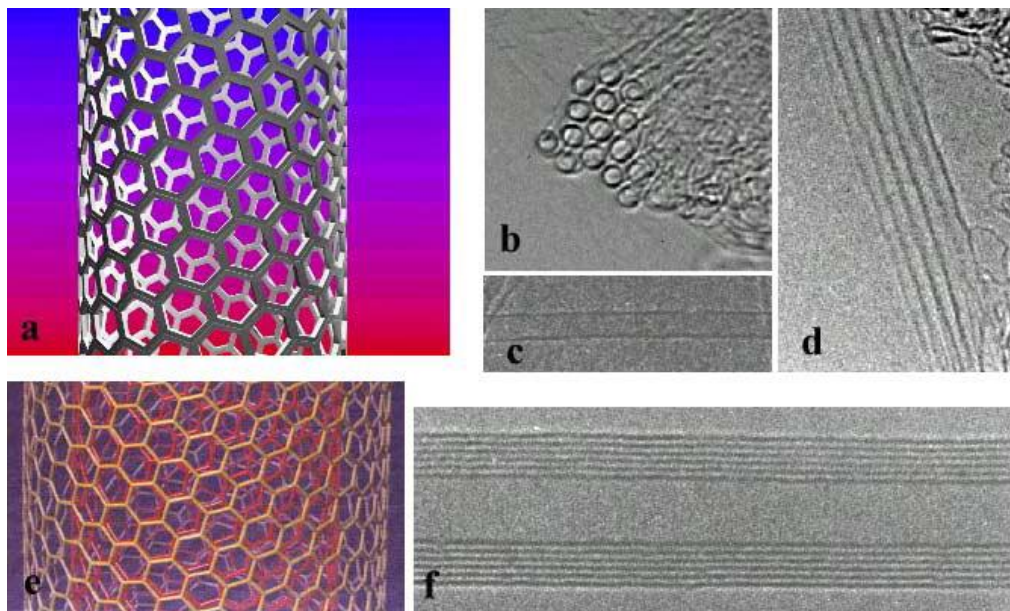
Figure 2.2: Structures of SWCNT (a-d) and MWCNT (e-f). (a) Schematic of an individual helical SWCNT. (b) TEM image showing the cross-section of a bundle of SWCNTs. (c) TEM image of a 1.5 nm diameter SWCNT. (d) A top view of a bundle of SWCNTs. (e) Schematic of an individual MWCNT, showing layers of the tube. (f) TEM image showing the distance between each layer of the tube (0.34 nm) [71].

CNTs have chemical bonding of sp^2 carbon-carbon bonds that provide CNTs with exceptional mechanical properties (i.e., tensile strength of 55-150 GPa [72], Young's modulus of 1.7-3.6 TPa [73]). Table 2.2 shows the physical properties of several carbon materials. CNT (density of 0.8-1.8 g/cm^3) are lighter than other carbon materials such as graphite (density of 1.9-2.3 g/cm^3). CNTs also possess remarkable thermal and electrical properties as compared with other carbon materials, as shown in Table 2.2. These properties allow CNTs a wide range of applications such as electronics, sensors, energy storage and aerospace applications.

Table 2.2: Physical properties of different carbon materials [74]

Property	Graphite	Diamond	Fullerene	SWCNT	MWCNT
Specific gravity (g/cm^3)	1.9–2.3	3.5	1.7	0.8	1.8
Electrical conductivity (S/cm)	4000^p, 3.3^c	10^{-2}–10^{-15}	10^{-5}	10^2–10^6	10^3–10^5
Electron mobility (cm^2/ (V s))	2.0×10^4	1800	0.5–6	$\sim 10^5$	10^4–10^5
Thermal conductivity (W/(m K))	298^p, 2.2^c	900–2320	0.4	6000	2000
Coefficient of thermal expansion (K^{-1})	-1×10^{-6p} 2.9×10^{-5c}	$(1\sim3)\times10^{-6}$	6.2×10^{-5}	Negligible	Negligible
Thermal stability in air (°C)	450–650	<600	$\sim$600	>600	>600

p: in-plane; c: *c*-axis.

2.3 Self-healing materials

Self-healing materials have attracted great attention due to their ability to heal damage for prolonging the lifetime of materials. The materials involve autonomic or nonautonomic healing, relying on whether an external stimulation (e.g., temperature [75] or light [76, 77]) is needed or not. There are three main methods to produce self-healing materials: capsule-, vascular- and intrinsic-based strategies [78]. The first two methods rely on the release of monomers and a catalyst that are loaded into microcapsules (Figure 2.3(a)) or stored inside vessels (Figure 2.3(b)) to heal the matrix damage. White group in 2001 firstly reported a self-healing system that can spontaneously heal a crack in the material by releasing the microcapsulated healing monomer to polymerize the material [79]. They allow self-healing of large material volume (Figure 2.3(d)). However, these two methods have disadvantages of complicated fabrication processes and a depletion of the local healing agent. Figure 2.3(c) shows intrinsic-based self-healing methods that depend on the molecular interactions in the polymer such as host-guest interactions, hydrogen bonds, electrostatic

interactions and metal-ligand coordination. For example, Miyamae *et al.* reported a supramolecular hydrogel that can be healed via host–guest interactions under wet conditions [80]. Intrinsic self-healing polymers with relatively fast self-healing processes (Figure 2.3(e)) could be achieved by designing the polymer compositions. However, it may be unable to obtain large-volume self-healing (Figure 2.3(d)).
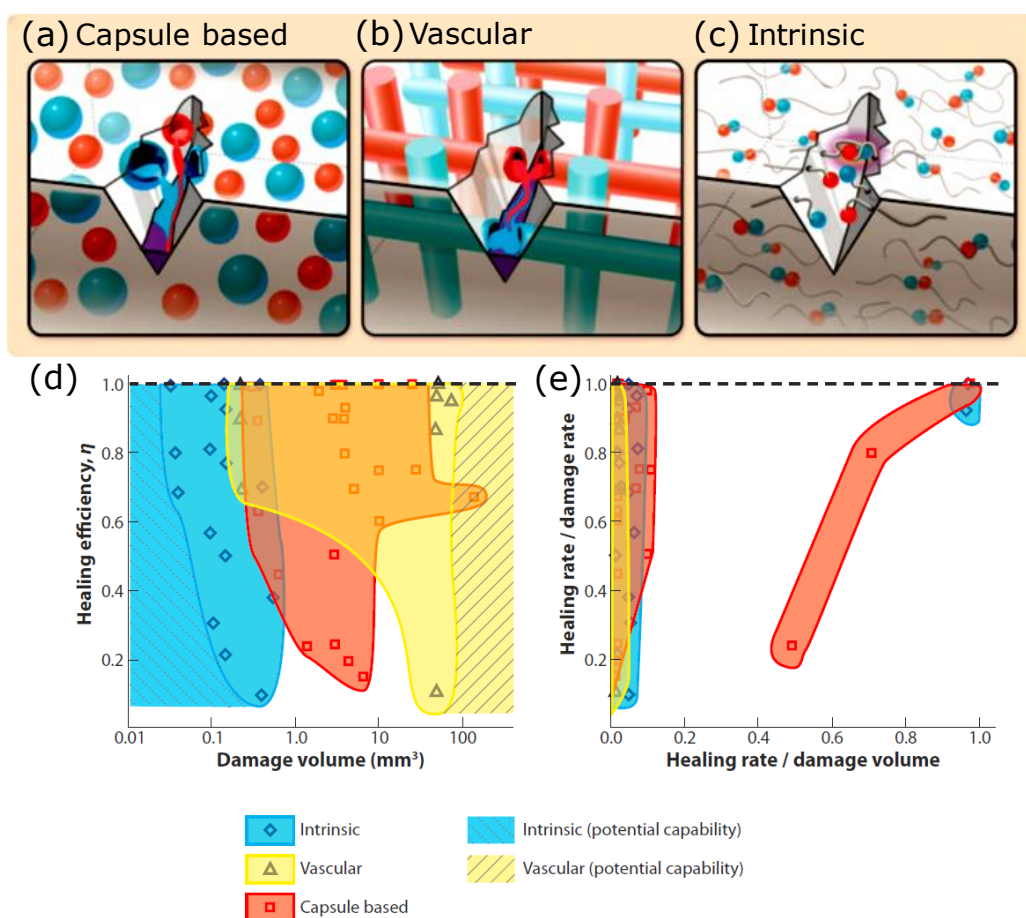
Figure 2.3: Demonstration of self-healing methods including (a) capsule-based, (b) vascular-based and (c) intrinsic-based approaches. (d) performance maps of different self-healing materials on the healing of different volumes and healing rate [78].

Table 2.3 shows a list of studies on self-healing materials with different classification (CA), healing mechanism (HM), healing condition (HC), conductivity (CD) and recovery of mechanical (RM) and electrical (RE) properties. Intensive research has currently been taken into self-healing materials that are capable of recovering mechanical properties. For example, Diba *et al.* demonstrated self-healing composite colloidal gels by carefully controlling the assembly of gelatin

and silica nanoparticles [81]. Zhao et al. demonstrated CS-based hydrogels that can spontaneously heal the damage within 6 h at 25 °C [82]. Despite their great self-healing designs, a lack of electrical conductivity limits their electronic applications. Odom *et al.* also provided an example of using solvent-filled microcapsules from a conductive silver ink to heal damage, allowing excellent restoration of conductivity [83]. Cao *et al.* investigated a polar polymer network combined with a ionic salt to obtain a ionic conductor with autonomous self-healing capability by harnessing ion-dipole interactions [84], but a low conductivity of 0.01 S/m was presented. A rGO-based nanocomposite (conductivity of 90 S/m) was developed with autonomic self-healing to restore mechanical and electrical properties. However, the fabrication method (freeze-casting) is difficult to fabricate precisely controlled 3D structures.

Table 2.3: Various examples of self-healing materials

Material[A]	CA[B]	HM	HC[C]	CD (S/m)	RM	RE	Ref.
EP	Non	Temperature	120 ºC, 24 h	-	57% in fracture load,	-	[75]
TEG	Non	Light	Visible light, 24 h	-	87% in strain	-	[76]
SE	Non	Supramolecular interaction	Laser, 60-80 ºC, 20-60 min	-	Full recovery	-	[77]
EP	Auto	Microcapsule	RT, several min	-	75% in toughness		[79]
PAm, NIPAm	Non	Host-guest interaction	3 h, wet condition	-	68% in strength, 72 h	-	[80]
GN, SN	Auto	Electrostatic interaction	RT, 30 min	-	Similar stress and strain at break	-	[81]

	A	B		C				
CEC, OSA	Auto	Imine bond, acylhydrazone bond	25 ºC, 12 h			90% in strain at break, 12 h	-	[82]
AgP, PUE	Auto	Microcapsule	RT, 10 min	Resistance of 0.95 Ω			80% in voltage	[83]
PVDF-co-HFP	Auto	Ion–dipole interaction	5 min	0.01	100%		-	[84]
PBS/rGO	Auto	Dynamic dative bond	Several min	90	Complete, 24 h		90% in CD	[85]
Our work	Non	Electrostatic interaction	Water vapor, 5-60 s	1450	90% in toughness		95% in CD	

A: EP: epoxy, TEG: tetra(ethylene glycol), SE: supramolecular elastomers, AgP: silver particle, PUE: polyurethane elastomer, PAm: poly(acrylamide), NIPAm: poly(N-isopropylacrylamide), GN: gelatin nanoparticle, SN: silica nanoparticle, CEC: N-carboxyethyl CS (CEC), OSA: oxidized sodium alginate, PVDF-co-HFP: poly(vinylidene fluoride-co-hexafluoropropylene, PBS: polyborosiloxane, rGO: reduced graphene oxide, B: Auto: autonomic, Non: nonautonomic; C: RT: room temperature.

2.4 Fabrication techniques used for 3D chitosan structures

Conventional fabrication techniques, including solvent casting, phase separation, freeze drying, and electrospinning, have been extensively used to produce 3D CS scaffolds.
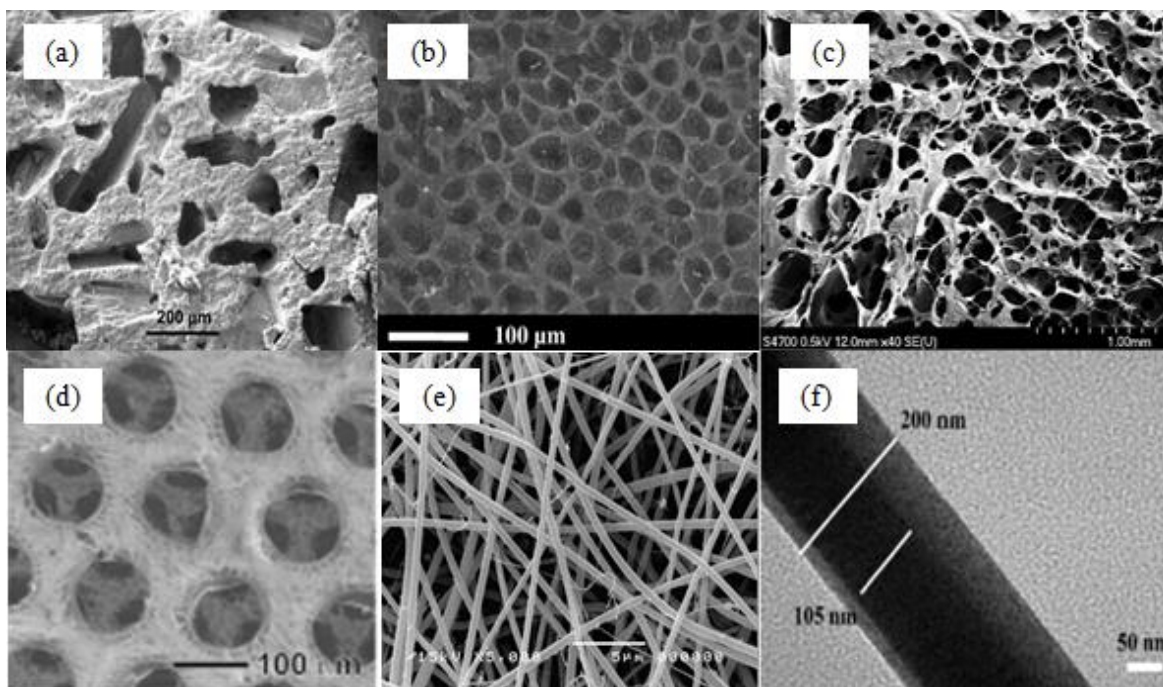
Figure 2.4: Typical CS constructs fabricated using various scaffolding techniques (a) scanning electron microscope (SEM) image of CS scaffold by solvent-casting. (b) SEM image of CS scaffold produced by gas forming [86]. (c) SEM image of CS scaffold by freeze drying [9]. (d) CS scaffold fabricated by freeze drying [87]. (e) electrospun CS nanofibrous membrane [10]. (f) core-shell structured PEO-CS nanofibers by coaxial electrospinning [88].

Solvent casting

Solvent casting technique offers an easy and inexpensive way to fabricate scaffolds. Specifically, the polymer/salt composite is cast into a mold and water-soluble porogens, e.g. wax, salts or sugars, are used to create pores or channels [7, 89]. Sponge-like scaffolds are obtained by evaporating the solvent and removing the porogen [7, 8]. Figure 2.4(a) shows the CS-calcium phosphate scaffolds prepared by solvent casting with different macroporosity (i.e., 17.6 %-65.5 %) and pore size of 165 µm to 271µm. The scaffolds strength range from 0.3 to 8 MPa as the macroporosity is decreased [90]. The limitations of CS scaffolds fabricated by this approach are that they may retain some of the toxicity from the solvent and it is difficult to obtain high porosity of scaffolds.

Gas foaming

Gas foaming has the advantages of requiring neither toxic solvents nor high temperature [89]. Compression-molded polymer disks are exposed to carbon dioxide (CO_2) gas under high pressure to generate highly porous scaffolds. The solubility of carbon dioxide in the polymer declines as pressure is released, as phase separation occurs between the polymer and carbon dioxide gas, which allows the formation of a porous structure [2]. Figure 2.4(b) shows the CS scaffolds fabricated by using dense gas CO_2 and cross-linkers. Highly porous, wet, and rigid structures were obtained and the average pore diameter of the scaffolds was around 40 µm [86]. The CS scaffolds produced by this technique however lead to low pore interconnectivity, especially on the surface of the structure.

Freeze drying

After dissolving in a solvent (acetic acid, water, or benzene), the polymer solution is poured into a mold, frozen and freeze-dried to acquire highly porous scaffolds under high vacuum [8, 89]. Cross-linked CS scaffolds (Figure 2.4(c)) produced for skin regeneration had pore size of roughly 150 µm and porosities from 79% to 85% [9]. The scaffolds achieved maximum tensile strength of 81 kPa; much lower than the ultimate tensile strength (7.7 MPa) of human skin [91]. Despite the advantages of the low temperature maintaining the original properties of scaffolds and not necessarily using toxic solvents, freeze drying has the limitation of obtaining scaffolds with small and inhomogeneous pore size [89]. Choi et al. developed CS scaffolds (Figure 2.4(d)) by using polycaprolactone (PCL) microspheres with freeze drying before removing the PCL with DCM to form uniform pore structures. The final CS scaffolds were formed without using cross-linkers based on pH dependence of CS solubility [87]. However, the process is still time-consuming and complicated.

Electrospinning

Electrospinning can produce fibers with diameters ranging from nanoscale to microscale [92]. This

procedure involves creating a high intensity electric field between a nozzle and a collector with electric opposite charges [92, 93]. The polymer solution in the nozzle overcomes the liquid surface tension and then is ejected to form fibers which are deposited in the collector [92]. Figure 2.4(e) illustrates two-dimensional (2D) nanofibrous CS membranes produced by electrospinning combined with solvent-cast, with fiber diameters of 126 ± 20 nm and membrane thickness of $72 \pm 5\mu$m [10]. CS was mixed with poly(ethylene oxide) for achieving electrospinability in electrospinning [94]. Core-shell constructed CS nanofibers (Figure 2.4(f)) have been fabricated by coaxial electrospinning [88]. The CS scaffolds produced by electrospinning exhibit properties of high porosity, a wide range of pore distribution, and high surface area. However, it is difficult to obtain 3D structures and the obtained 3D scaffolds have the drawbacks of inhomogeneous pore distribution, tortuous pores, and small pore size [95, 96].

2.5 3D printing

3D printing consists of a computer-controlled translation stage, allowing the fabrication of materials via transforming the digital design into 3D objects. Unlike traditional manufacturing techniques that need molds or lithographic masks to fabricate 3D structures, 3D printing can fabricate complex 3D structures via rapid prototyping. 3D printing has numerous advantages such as low-cost, reliability, mass customization and design flexibility. It can be divided into light-based printing such as stereolithography (SLA), and ink-based printing such as robotic dispensing, as shown in Figure 2.5 [97].
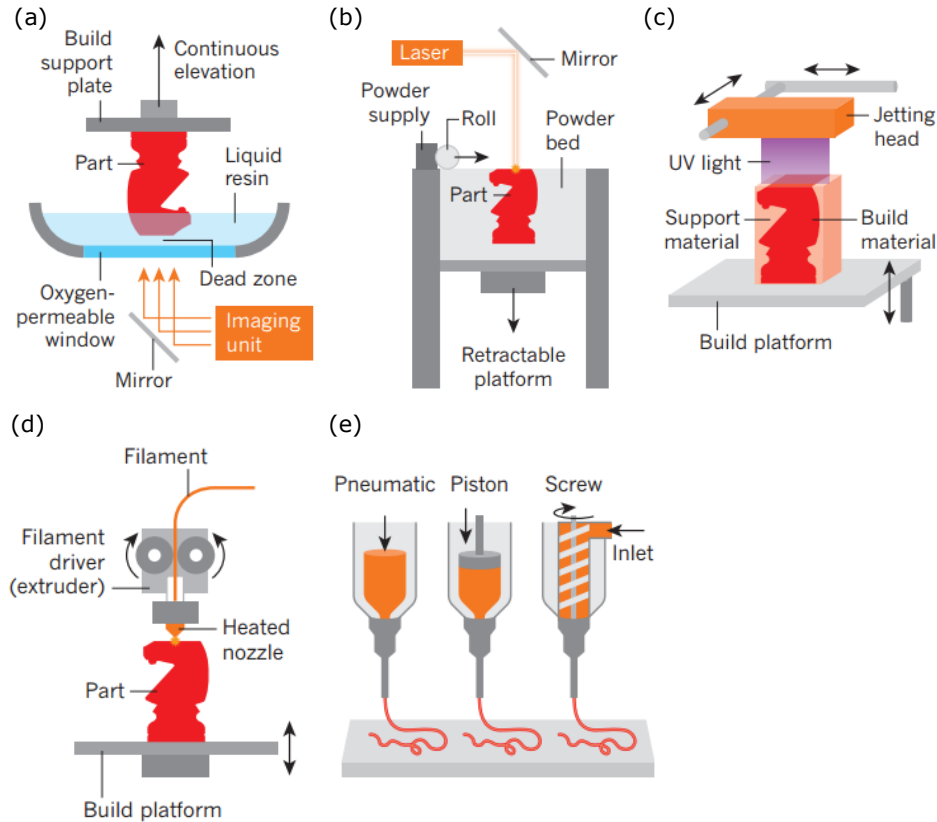
Figure 2.5: 3D printing methods classified into light- and ink-based printing methods. (a) Light-based printing: SLA of liquid resin. (b) Light-based printing: selective laser sintering of polymeric or metallic powders. (c) Light-and ink-based inkjet printing. (d) Ink-based fused deposition modelling. (d) Robot dispensing using viscoelastic inks [97].

Light-based 3D printing methods use light sources such as laser and photon to form structures, such as SLA and selective laser sintering (SLS). In the fabrication process of SLA, a liquid resin is continuously photopolymerized by a laser, and the structure is built by the solidification of a new layer resin via the photopolymerization (Figure 2.5(a)). SLA requires the inks with low to moderate viscosity. In SLS, the polymeric powders such as ceramic are locally fused by a laser to form 3D structures in a powder bed (Figure 2.5(b)). Other light-based methods such as two-photo polymerization (2PP), digital projection lithography (DLP) are also used to fabricate various structures.

Ink-based 3D printing methods can pattern materials by using 3D-printable inks through either droplet- or filament-based 3D printing. Droplet-based printing methods such as inkjet printing, hot-melt printing use low-viscosity soft materials to fabricate structures. Inkjet printing can incorporate light-based printing. For example, some inkjet printers involve an ultraviolet (UV) light source that can photopolymerize a liquid resin during the printing process (Figure 2.5(c)). Filament-based 3D printing employs an applied pressure, mechanical force or heating to extrude materials as a continuous filament. For example, fused deposition modelling (FDM) can fabricate thermoplastic polymers into different structures in a layer-by-layer manner. A heating extrusion head is used to melt the thermoplastic filaments and the filaments solidify as they cool in air (Figure 2.5(d)). An alternative technique to FDM is robotic dispensing (Figure 2.5(e)). For this method, a 3D-printable ink is loaded into a syringe and extruded either by pneumatic, piston- or screw-driven force on a platform. It offers a wide range of ink designs such as fugitive inks [23], collagen [29], poly(dimethyl siloxane) (PDMS) [98], nanocomposites [99, 100], and polylactic acid (PLA) [25]. Solidification of these materials to yield desired structures is either through concentrated inks, supported bath or reservoir, tailoring desired rheological properties (e.g., shear thinning behavior, viscoelastic properties), or solvent evaporation. In some cases, additional processing steps are also performed to solidify the ink during the fabrication process, such as UV-assisted polymerization used to form self-supporting and freeform structures [101] and low-temperature (−20 °C) applied to solidify the ink filament on a cryogenic plate [102].

2.6 3D printing of natural polymers

Biomaterials commonly used for 3D printing are ceramics, metals (e.g., using SLS based on polymeric or metallic powders) and synthetic polymers such as PLA (e.g., using FDM based on thermoplastic polymers) and photosensitive polymers (e.g., SLA based on photopolymerizable resins), and metals. However, these 3D printing have limitations to fabricate very soft materials

such as naturally derived hydrogels. Natural polymers including polysaccharides and proteins still remains challenging to 3D print, since they are too soft to support themselves and thus may collapse or deform during the printing process [29]. Current approaches for 3D printing of natural polymers have obtained significant advances. Table 2.4 shows a collection of natural polymers that can be fabricated by 3D printing. Inkjet printing and robotic dispensing are normally used to generate various structures using natural polymers.

Table 2.4: Summary of natural polymers fabricated by 3D printing

Natural polymer	3D printing technique	Concentration (%)	Structure	Resolution (μm)	Printing strategy	Ref.
Inkjet printing						
SF	Piezoelectric	6	Fiber, web-like structure	10	-	[103]
CS	Piezoelectric	0.2	Micropatterned- thin-film	50	-	[104]
AG	Thermal	2	Fiber	30	-	[105]
Robotic dispensing						
CS/HP	Pneumatic	3	Scaffold	300	Coagulation in reservoir	[27]
CS	Pneumatic	3	Scaffold	100	Coagulation in reservoir	[28]
CS	Pneumatic	4	Scaffold	290	Temperature assisted (-20 ℃ plate)	[102]
GEL	pneumatic	10	Scaffold	200	Temperature assisted	[106]

(10 ℃ plate)

GEL	Pneumatic	5	Scaffold	350	Adding crosslinker to tailor ink rheology	[107]
CNC	Pneumatic	20	Scaffold	410	Concentrated ink	[108]
SF	Pneumatic	28–30	Scaffold	5	Concentrated ink	[24]
SF	-	10-16	Hierarchical scaffold	> 500	Adding sacrificial organic microparticles	[109]
SF	Piston	10	Complex structures	200	Thermoreversible support bath	[29]
HA	Piston	5-20 wt	Scaffold	100	UV assisted	[110]
AG, CAI	Piston	4, 10, 8.94-9.64	Complex biological structures	200	Thermoreversible support bath	[29]
Our work	Pneumatic	8	Scaffold, complex structures	30	Directly printing in air	[111]

SF: silk fibroin, AG: alginate, HP: hydroxyapatite, CNC: cellulose nanocrystals, Ad–HA and CD–HA: HA modified with either adamantane (Ad) or β-cyclodextrin (β-CD), HA: hyaluronic acid, CAI: collagen type I

2.6.1 Inkjet printing

Inkjet printing allows fabricating structures in a very small volume with a high resolution; it can

be divided into thermal and piezoelectric inkjet printing [112]. Thin structures of silk fibroin (SF), chitosan (CS) and alginate (AG) were produced by inkjet printing (Table 2.4). For example, CS micro-pattern (Figure 2.6(a)) was generated on glass by inkjet printing to enhance cell mobility, spreading, and phagocytosis [104]. However, the process always used an ink with low viscosity [113] and was difficult to obtain a 3D structure with high aspect ratio (i.e., vertical direction).
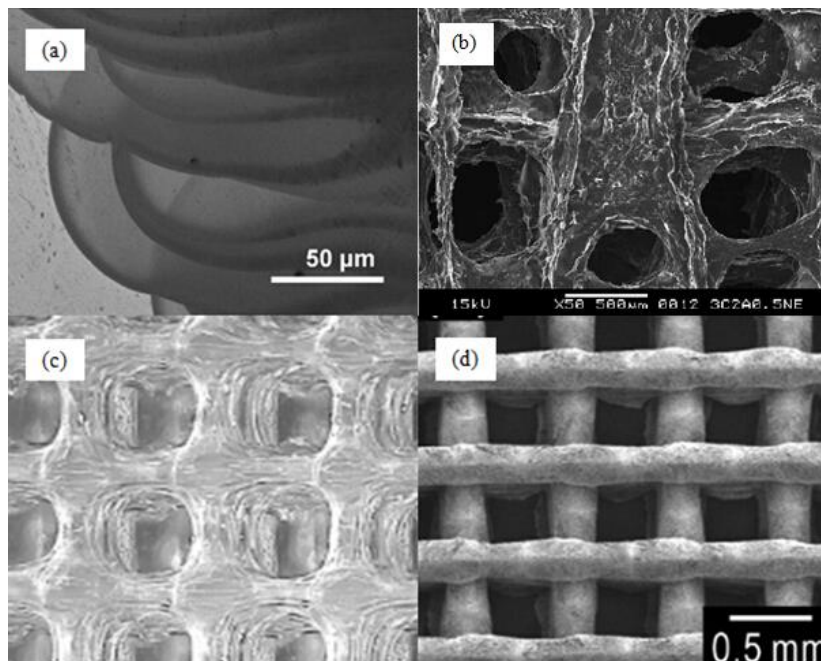
Figure 2.6: CS scaffolds fabricated by 3D printing. (a) CS micropattern generated by inkjet printing [104]. (b) CS scaffold fabricated by robotic dispensing [27]. (c) CS scaffold by robotic dispensing [28]. (d) CS scaffold fabricated by cryogenic 3D plotting system [102].

2.6.2 Robotic dispensing

Rather than single droplet, robotic dispensing can continuously extrude fibers and offers more direct control of the flow of the ink [114]. The fabrication process of natural polymers usually involved *in situ* gelling during the printing process to support the structure by using a bath or reservoir (Table 2.4) [27-29]. Out of this strategy, temperature- or UV-assisted step was applied to solidify the structures during the printing process [102, 106, 110]. Also, concentrated inks were

normally used to avoid the shape deformation due to drying-induced shrinkage [24, 108]. There are a few cases of 3D printing CS, either using a reservoir to conjugate the ink or using a temperature-assisted step during the printing process. Figure 2.6(b) shows 3D CS scaffolds fabricated by a CS solution (3% w/v) deposited into a bath with a mixture of NaOH-ethanol solution [27]. The scaffold had a fully interconnected channel structure with a maximum of 21 layers and the surface of scaffolds was rough. Macrospore diameters were observed from 400 to 1000 µm [27]. Figure 2.6(c) illustrates CS scaffolds produced by dispensing CS and NaOH at the same time. Four-layered scaffolds with pore diameters of 200-500 µm were produced by using nozzles with diameters of 100 and 200 µm. Both of the methods use the pH dependence of CS solubility. Lee *et al.* fabricated CS scaffolds by robotic deposition with a cryogenic refrigeration system. CS solution was solidified to form a structure on a temperature controlled plate (-20 °C) and the final porous scaffolds were generated by post-treatment of freeze-drying and cross-linking [102]. Figure 2.6(d) shows a CS scaffold exhibiting homogeneous pore size and high interconnectivity as well as rough surface. The filament diameters of CS scaffolds ranged from 290 to 310 µm and the pore sizes was around 400 µm. The CS scaffolds with dimensions of $10 \times 18 \times 1.8$ mm^3 had a maximum tensile strength of 0.16 MPa and maximum Young's modulus of 1.2 MPa [102].

2.6.2.1 Solvent-cast 3D printing

Solvent-cast 3D printing is typically based on a robotic dispensing system. Solvent-cast 3D printing can produce 3D structures at room temperature including a syringe inserted the ink and the ink is extruded on a plate to create filament, combined with rapid solvent evaporation (Figure 2.7) [25].
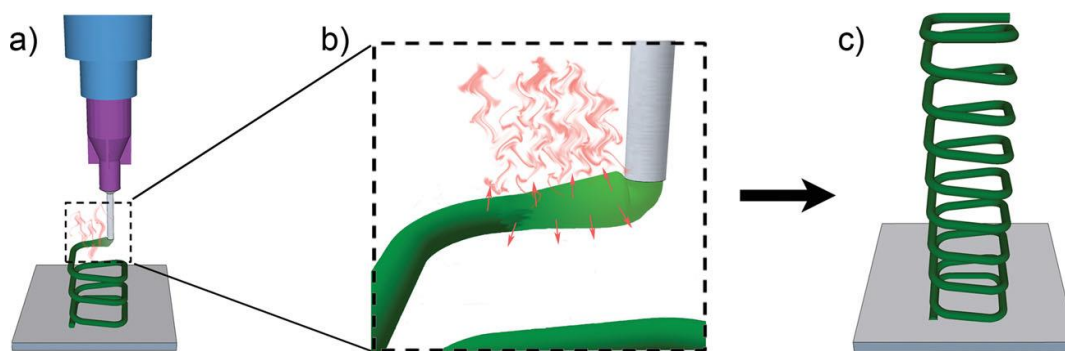
Figure 2.7: Schematic illustration of solvent-cast 3D printing with a thermoplastic solution. (a) Deposition of the polymer solution through a nozzle. (b) Rapid solvent evaporation post extrusion. (c) Example of a 3D square spiral produced by solvent-cast 3D printing [25].

Figure 4 shows the process of fabricating a 3D square spiral with a thermoplastic solution of high concentration. The 3D structure was generated by decreasing the diameter of the filament and increasing its rigidity after rapidly evaporating the solvent [25]. The technique is capable of creating different multifunctional microsystems with complex geometries, which might be a good option to fabricate natural polymers.

2.7 3D printing of nanocomposites

The combination of 3D printing and nanotechnology open new perspectives to engineer functional materials. Nanocomposite inks have been developed to fabricate various structures by different 3D printing methods for a wide range of applications such as sensors, photonics, biomedical applications, micro-antennas, electrodes and electronics, as shown in Figure 2.8. For exmaple, Lebel *et al.* reported UV-assisted 3D printing to fabricate 3D freeform structure of photocurable PU/CNT nanocomposites [101]. Guo *et al.* demonstrated solvent-cast 3D printing to fabricate a helical liquid senor by using PLA/ MWCNT nanocomposites [31]. Chizari *et al.* reported solvent-cast 3D printing of highly conductive PLA/CNT nanocomposites highly conductive nanocomposite materials (up to 5000 S/m) for semi-transparent electromagnetic interference (EMI) shielding application [115]. 3D-printed nanocomposites have also been employed for biomedical applications, such as graphene-based nanocomposite scaffolds used for supporting cell growth [33] and hydrogel nanocomposites used for detoxification devices [116].
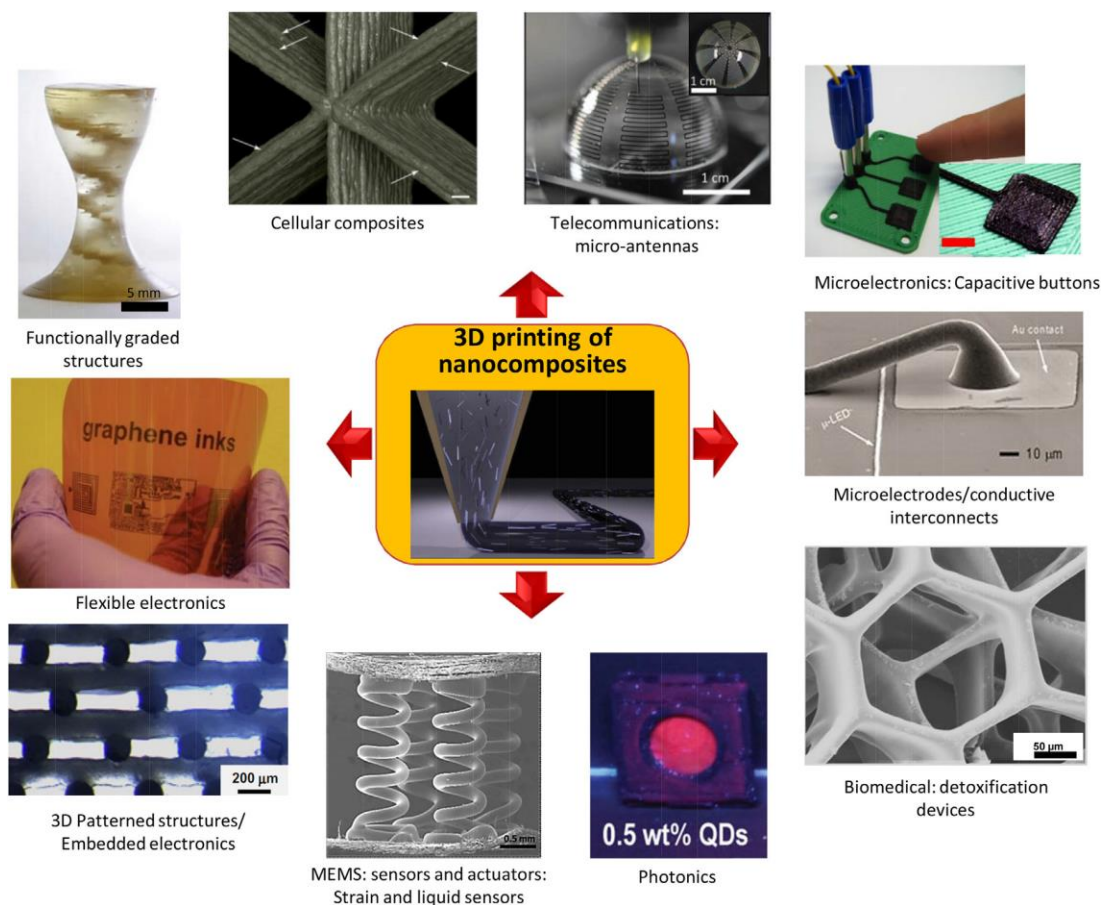
Figure 2.8: 3D nanocomposite macro- and micro-structures fabricated using different 3D printing methods [20].

It is worth noting that 3D printing can also tailor nanocomposite properties (such as mechanical and electrical properties). For example, Compton et al. demonstrated lightweight cellular nanocomposites made of epoxy resin, nanoclay and carbon fibers that were fabricated by 3D printing. The carbon fiber alignment due to the shear stress during the ink extrusion can reinforce the nanocomposites [100]. Chung et al. developed functionally graded nanocomposites fabricated by SLS. Material composition gradient (using non-uniform loading of silica nanoparticles) was exhibited along the build direction of the structure, which helps to obtain varying mechanical properties of the nanocomposites [117]. Secor et al. developed graphene-based nanocomposite film that was fabricated by inkjet printing to achieve an excellent conductivity of 25600 S/m for flexible electronics [63]. Nanocomposite electronics or sensors are usually made in a form of film [20]. Some researchers optimized nanocomposite sensors or electronics with 3D structures for achieving more efficient sensing ability [99, 118].

2.8 Applications of natural polymers and their nanocomposites

Natural polymers have gained great attention for various potential applications such as tissue engineering, drug delivery, and biomedical devices, due to their intrinsic properties such as biocompatibility, biodegradability and bioactivity. Compared with hydrogels based on synthetic polymers (e.g., pluronics, polylactic acid), naturally derived hydrogels show highly hydrated nature and abundant chemical signals that benefit cell growth. Natural polymers are also excellent candidate for developing next-generation of sustainable electronics owing to their lightweight, low-cost, non-toxic, biodegradability and renewable properties [14, 15]. Nanocomposites involving natural polymers and nanofillers have also been considered as a strategy for electronic applications.

2.8.1 Tissue engineering

As tissue engineering (TE) emerged in the late 1980s, it was aimed at fabricating man-made organs for the full regeneration of degenerated tissue or organs [4]. There are three TE strategies for regenerating issues: 1) implantation of cells or cell-extracellular matrix (ECM) grafts [119, 120]; 2) implantation of biomaterials [121]; 3) transplantation of cell-scaffold constructs [122]. Specifically, cells such as bone-marrow-derived stem cells can be directly injected into the infarct region for improving tissue function [123]. The scalability is still a main limitation of cell-based approaches [124], and most of the cells are lost in blood circulation, and successfully injected cells easily die within several days after transplantation [125, 126]. An alternative approach to cell injection is the use of scaffolds engineered by using biomaterials to offer protective and biomimetic environments for cell growth. It is difficult to grow and remodel in tissue repair by using not-cellularized grafts [121]. A combination of cells and polymer scaffolds is an appealing method in TE [3].

2.8.1.1 Scaffold requirements for tissue engineering

Tissue-engineered scaffolds should mimic a certain degree of biological and functional complexity of tissue or organ. Firstly, the scaffolds should be biodegradable and biocompatible. Both synthetic and natural polymers have been studied for the fabrication of 3D scaffolds. Even though synthetic biomaterials (such as PLA and ceramics) have good mechanical and physical properties, these polymers lack bioactive binding sites [127], and provide an environment that may inhibit cell adhesion, proliferation, and differentiation [128]. Natural polymers are capable of simulating

aqueous natural extracellular matrices and having abundant chemical signals, as well as providing high affinity with cells [129]. Among them, CS has been applied in tissue engineering due to its excellent biodegradable, biocompatible, and non-toxic properties [130, 131]. The structural similarity of CS and glycosaminoglycans and the hydrophilicity of CS improve the interaction with growth factors and cellular receptors [132, 133]. For instance, CS can enhance cardiac function through inducing the formation of neo-vasculature [134]. Secondly, the scaffolds for TE have to offer a temporary and suitable mechanical support [89]. For example, the scaffold engineered for cardiac tissue should have similar values of mechanical properties to that of real cardiac tissue. The Young's modulus of myocardium is about 10-20 kPa at initial stage of diastole, and goes up to 200-500 kPa at the end of diastole [135], and the maximum elongation of it is 22-90% [136]. Finally, the geometry of the scaffolds should mimic the structure of extracellular matrix (ECM): high degree of porosity, interconnectivity, well-controlled geometry and high surface-volume ratios [2, 137]. The porosity is not uniform and the pore size differs from the core to the skin in various microstructures of tissue or organs including cardiac muscles and bones [11-13]. Scaffolds with oriented pores for cardiac TE have resulted in high cell density [138], most probably because of favoring cell migration and differentiation and efficient nutrient diffusion [13, 139]. Anisotropic CS nanofibers have been produced by electrospinning with randomly oriented fibers and bulk mechanical properties [11]. Recent advances in TE have demonstrated scaffolds with hierarchical structures to have the control of topographical features for exploring the effect of surrounding environment on cells. For example, Kang et al. reported microfluidic spinning of thin collagen fibers (thickness < 10 μm) with groove patterns (width of 5 μm) that can guide cell alignment [140]. Chen *et al.* reported Pre-stressed polyethylene film with wrinkled surface generated by treating oxygen plasma, which can guide stem cell alignment [141]. However, those structures with micro/nanopatterned surfaces have limited thickness (<100 μm) and thus cannot cultivate cells in real 3D. Their fabrication methods are also difficult to fabricate 3D scaffolds for cell growth.

2.8.1.2 Wearable devices

The recent progresses have been developed a range of self-healing materials for wearable devices such as solar cells, batteries, electronic skin, supercapacitor and batteries (Figure 2.9).
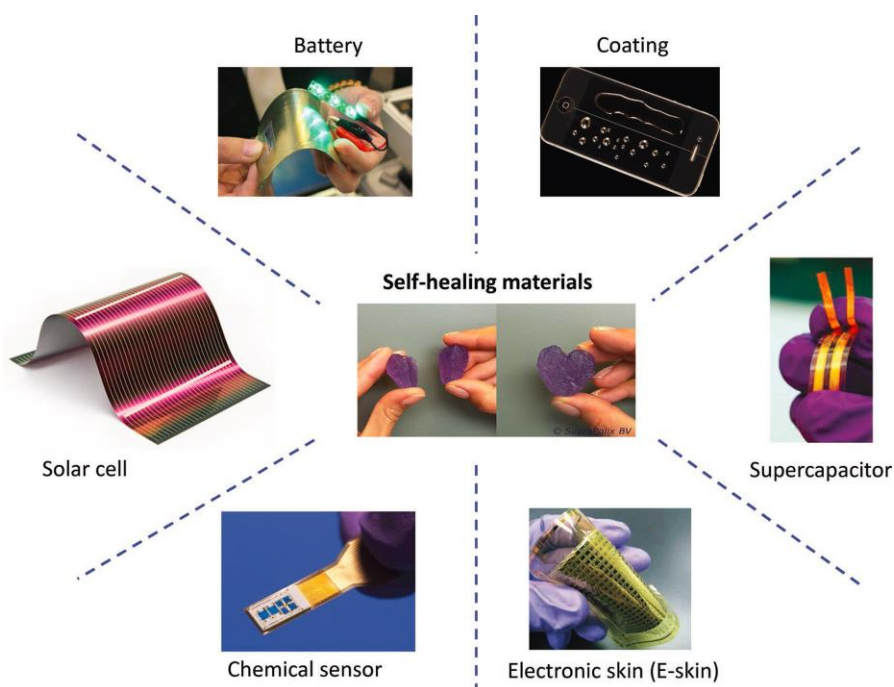
Figure 2.9: Applications of self-healing materials for different wearable devices [17].

Self-healing materials are designed to restore material properties and shapes, which are particularly appealing for wearable devices.For example, supramolecular multiple hydrogen bonding elastomer was capable of restoring its mechanical and electrical properties and it was used to design a human-machine interaction system [142]. Self-healing material can also be used as a coating layer on electrical wires or circuits (building sandwich structure) for wearable devices. For example, He *et al.* demonstrated that a self-healing supramolecular polymer (fatty polybasic acid reacted with diethylenediamine) can load a thermal-sensitive ionic liquid to heal the damage of liquid channel and avoid the leakage of the liquid for electronic sensor application [143].

Wearable devices are favorably equipped with lightweight, flexible, stretchable, easy-to-make and versatile sensing systems. Nanocomposites are excellent candidates to develop various structures for wearable devices. Table 2.5 shows some examples of nanocomposites used as wearable sensors including detect human motions, humidity or gas in the environment. The properties of nanocomposites such as flexibility (F), stretchability (SB) and self-healing (Sf) directly decide the sensing ability of wearable sensors. For example, Amjadi *et al.* reported PDMS/AgNW nanocomposites show repeatable sensing ability at a strain (SR) of 70 % [144]. Zhou *et al.* demonstrated PI/rGO nanocomposite that can detect the humidity. Their strain sensors can detect the bending of different fingers. The electrical resistance of the nanocomposite fiber responded in

a short time of 40 s. Yang *et al.* demonstrated MT/CCTO nanocomposite that heal itself by Diels–Alder and retro-Diels-Alder reactions. Sandwich structure was built by spraying SWCNT on both surface of MT/CCTO nanocomposite. It can be used as a strain sensor to detect the finger bending. The sensor was capable of recovering its resistance by self-healing after 30 min and continued to detect the bending motion. As shown in Table 2.5, most nanocomposites have no self-healing properties and they show a limited elastic strain range. There is a need to develop self-healing nanocomposites to combine self-healing, conductivity, lightweight, easy-to-make, flexible and stretchable properties for a wide range of applications including wearable sensors.

Table 2.5: Examples of wearable sensors based on nanocomposites

Nanocomposite[A]	F	SB; SR (%)	Sf	Structures	Sensing applications	Ref.
PDMS/AgNW	F	70	-	Film	Strain sensor on finger bending	[144]
PI/rGO	F	5	-	Fiber	Pressure, bending, stretching	[145]
PVA/SWCNT	-	150; -	-	Film	Humidity sensors	[146]
SF/SWCNT	F	23; -	-	Coatings on SF fibers	Humidity sensor, temperature senor, finger touching	[147]
PANI/MWCNT	-	-	-	Film	Gas sensor	[148]
GelMA/MWCNT /SWCNT	F	115; 20	-	Fiber on a cellulose paper	Substrate bending	[118]
MT/CCTO, SWMNT	F	-	Sf by DA and r-DA reaction	Sandwich	Finger bending	[149]
PLG/GR	F	375; -	-	Fiber on a substrate	Substrate bending	[33]

Our work	F	230	Sf by water vapor	Microstructu red fiber	Strain and humidity sensor

A: PDMS: Polydimethylsiloxane, AgNW: silver nanowire, PI: polyimide, PVA: Poly(vinyl alcohol), SF: silk fibroin, PANI: polyaniline, GelMA: gelatin methacryloyl MT: Diels–Alder cycloaddition polymer, CCTO: $CaCu_3Ti_4O_{12}$,

B: DA: Diels–Alder, r-DvA: retro-Diels-Alder PLG: polylactide-co-glycolide, GR: graphene

2.9 Summary of literature review

Chitosan, a natural polysaccharide, has interesting and unique intrinsic properties such as biodegradability, biocompatibility, renewability and bioactivity, which make it an excellent candidate for tissue engineering and electronic applications. However, CS generally exhibits weak mechanical properties, especially in hydrated state, and there is consequently a need for improving its properties.

Simple 3D structures such as freeze-dried sponges, solvent-cast scaffold and electrospun matrices have been produced from natural polymers. However, they usually have disordered structures, without a precise control of their architectures (such as the control of pore shape, porosity, interconnectivity and surface pattern). When these structures are used for tissue engineering, they always lead to randomly distributed cells. Cell alignments have been widely shown in tissues and organs at different scales. Therefore, the formation of 3D scaffolds that can guide spatial and oriented organization of cells is extremely important for mimicking the structural complexity of real tissue or organs. 3D printing might address these issues due to its ability to produce complex 3D geometries. However, it is still challenging to fabricate from natural polymers such as CS because the natural polymer inks are too soft to support themselves.

Currently, there is few research works on nanocomposites made of natural polymers as a matrix. It is a great interest to develop "green" nanocomposites for electronic applications. In addition, self-healing behavior is very desirable since it can prolong the material lifetime. However, most self-healing materials are insulating. Conductive nanocomposites may solve this problem with the addition of conductive nanofillers in self-healing materials. The nanocomposites used in electronic applications such as wearable sensors are usually in a form of thin films. This form of

nanocomposites does not present high sensing ability. There is a need to translate 2D structures to more complex 3D structures for application efficiency. 3D printing has been developed to fabricate conductive nanocomposites with 3D structures. Novel nanocomposites combined with functional properties (such as self-healing, stretchability and conductivity) and a high level of printability (the fabrication of tunable 3D structures along with ink flow without nozzle clogging) are needed to overcome those limitations and achieve a further progress in electronic applications.

This thesis aims at addressing these various issues, and the objectives are presented in the next chapter.

CHAPTER 3 RESEARCH OBJECTIVES AND COHERENCE OF ARTICLES

3.1 Research objectives

The principal objective of this research is to develop novel CS and CS/CNT inks for the fabrication of complex 3D structures. This fabrication process should allow the materials to feature multifunctional properties for tissue engineering and electronic applications.

3.1.1 Specific objectives of the research

1) Develop CS inks for water-based solvent cast 3D printing. Establish a comprehensive characterization of the effect of fabrication parameters and CS-related parameters on the printability and material properties.

2) Fabricate CS-based complex 3D scaffolds that can be used for guide cell growth.

3) Develop CS/CNT conductive nanocomposites featuring self-healing properties.

4) Adapt instability-assisted 3D printing to CS/CNT nanocomposites for fabricating microstructured fibers and demonstrate the feasibility of CS/CNT nanocomposites as humidity and strain sensors.

3.1.2 Presentation of articles and coherence with research objectives

Chapter 4, 5 and 6 present the core results of the thesis with three articles in the form of accepted (Chapter 4), published (Chapter 5) and submitted (Chapter 6) states. These articles cover all the research objectives and are described in the following section:

Chapter 4 presents the first article "*Processing and Properties of Chitosan Inks for 3D Printing of Hydrogel Microstructures*", accepted in ACS Biomaterials Science & Engineering (Manuscript ID: ab-2018-00415w.R1). This journal was chosen because it focuses on new biomaterials, bioinspired and biomimetic approaches to biomaterials. This paper was submitted on Jan 1, 2018 and accepted on May 24, 2018. In this work, a comprehensive study of the properties of CS inks for 3D printing is carried out (Specific Objective 1). The rheological properties of CS inks with different concentration are analyzed by rotational rheometry and capillary flow. Solvent evaporation rate of

the various inks is also investigated. A processing map is generated by considering fabrication and materials parameters such as micronozzle diameter and ink concentration for successful 3D printing. The material properties of CS filament after different processing steps are also studied.

Chapter 5 shows the content of the second article, "*3D Printing of Microstructured and Stretchable Chitosan Hydrogel for Guided Cell Growth*", published in Advanced Biosystems (DOI: 10.1002/adbi.201700058). This journal was chosen because it is in the field of life sciences and focuses on innovative biological systems and advanced biotechnology. This paper was submitted on April 11, 2017 and published on May 15, 2017. In this work, CS inks are printed at room temperature in the form of complex 3D scaffolds (Specific Objective 2). The ink filament is extruded to form a 3D structure in a layer–by-layer manner and the filament solidification occurs through solvent evaporation. The resultant 3D structures show a high resolution of 30 µm. A physical gelation of the printed scaffold is processed by neutralization in sodium hydroxide. The mechanical properties of as-printed and neutralized filaments are measured, showing high stretchability and tensile strength. Guided fibroblast cell growth is also demonstrated.

Chapter 6 shows the third article "*3D Printing of Self-healing and Stretchable Nanocomposite Sensors*", submitted on May 31, 2018 to Materials Horizons. This journal was chosen because it focused on materials science with chemistry, physics, biology and engineering. In this work, we develop CS/CNT nanocomposite inks that are prepared using a ball mill mixing method (Specific Objectives 3 and 4). The CS/CNT nanocomposite present healing properties under exposure to water vapor and electrical conductivity and mechanical properties can be restored. The self-healing is rapid, occurring within seconds after the damage of the nanocomposite. Instability-assisted 3D printing is also adapted to fabricate CS/CNT microstructured fibers featuring sacrificial bonds and hidden length that can achieve a high stretchability (strain at break of ~ 180%). The multifunctional nature of this CS-based nanocomposite enables it to be designed as wearable sensors.

CHAPTER 4   ARTICLE 1: PROCESSING AND PROPERTIES OF CHITOSAN INKS FOR 3D PRINTING OF HYDROGEL MICROSTRUCTURES

Qinghua Wu[†], Daniel Therriault [‡] and Marie-Claude Heuzey[†]*

Published: ACS Biomaterials Science & Engineering, 4 (7), 2018, 2643–2652

[†]Department of Chemical Engineering, Research Center for High Performance Polymer and Composite Systems (CREPEC), Polytechnique de Montréal, 2900 Boulevard Edouard-Montpetit, Montréal, Quebec, Canada

[‡]Laboratory for Multiscale Mechanics (LM2), Department of Mechanical Engineering, Research Center for High Performance Polymer and Composite Systems (CREPEC), Polytechnique de Montréal, 2900 Boulevard Edouard-Montpetit, Montréal, Quebec, Canada

*Corresponding Author E-mail: marie-claude.heuzey@polymtl.ca

KEYWORDS: Additive manufacturing, chitosan, hydrogel, microstructures, high strength

4.1 Abstract

The ability to precisely control the properties of natural polymers and fabricate three-dimensional (3D) structures is critical for biomedical applications. In this work, we report the printing of complex 3D structures made of soft polysaccharide (chitosan) inks directly in air and at room temperature. We perform a comprehensive characterization of the 3D printing process by analyzing the effect of ink properties (i.e., rheological properties and solvent evaporation) and process-related printing parameters (i.e., nozzle diameter, robot velocity, and applied pressure). The effects of the neutralization step on the hydrogel formation and their mechanical properties are also investigated. Solvent evaporation tests show that the chitosan ink prepared using an acidic mixture contains residual acids after printing, helping reducing shrink-induced shape deformation. A processing map presents the appropriate ranges of process-related parameters for different structures including filaments, 30-layer scaffolds, starfish, leaf, and spider shapes, showing the versatility of the fabrication approaches. After neutralization, 3D scaffolds still maintain their shape while neutralized filaments show high tensile properties such as a maximum tensile strength of ~ 97 MPa in the dry state and high strain at break ~ 360 % in the wet state. Our fabrication approach provides guidelines to optimize the design and fabrication of aqueous-based inks and opens a new door for

fabricating complex structures from natural polymers and achieving tunable material properties for biomedical applications such as tissue engineering and drug delivery.

4.2 Introduction

Natural polymers are attractive biomaterials for biomedical applications due to their intrinsic properties such as biocompatibility, biodegradability and bioactivity.[1-2] The ability to precisely control their material properties and shapes is important for applications such as tissue engineering.[3] 3D printing methods are promising avenues to fabricate complex biomedical devices such as cardiac microphysiological devices[4], vascular networks[5] and 3D cancer tissue model.[6] However, the 3D printing of natural polymers is still in its early stages, but a few recent studies have achieved significant advances.[7] Usually, 3D printing approaches used for natural polymers require *in situ* crosslinking during the printing process because these water-soluble polymers are generally too soft to self-support their structures.[8-9] For example, structures made of various natural polymers (e.g., gelatin,[10] alginate,[8] chitosan-based polymer[11-13] and hyaluronic acid[14-15]) have been fabricated via partial crosslinking, reservoir-induced cross-linking, or chemical modification. However, these fabrication methods show limited control of the structure resolution (>200 µm). Low temperature manufacturing is developed to solidify the structures during printing.[16] For example, Lee et al reported the fabrication of highly porous chitosan scaffolds through solidification of the structure on a cryogenic plate held at −20 ˚C during the printing process, followed by a freeze-drying process to maintain the 3D structures. A porous structure within the filaments was obtained due to the low temperature and freeze-drying process, which resulted in weak mechanical properties (i.e., Young's modulus of 1.2 MPa and maximum tensile strength of 0.16 MPa for a dried scaffold). So far, the printability of natural polymer inks is still challenging. For example, dilute inks (e.g., 4 wt%)[17] experience significant drying-induced shrinkage during the printing, resulting in the loss of shape fidelity in printed structures.[18] It was demonstrated that the increase of ink concentrations (e.g., 28 wt %)[19-20] or the crosslink density[21] can improve the printability via higher viscosity and minimization drying-induced shape deformation. These viscous inks are not ideal for biomedical applications due to their lower biocompatibility.[22-23] Therefore, developing novel printable natural materials and fabrication approaches for 3D printing is highly attractive and promising for both academic and industrial fields.

Chitosan, a naturally-derived polysaccharide, is non-toxic, biodegradable, biocompatible, bio-adhesive and renewable.[24] For pH below its pKa (pH < 6.2), the amino group (NH_2) on the chitosan chains are protonated into positively charged group (NH_3^+) giving it solubility. Soluble chitosan allows a vast range of applications such as tissue engineering,[25] water treatment,[26] biosensors and drug delivery.[27] Physical chitosan hydrogels can be obtained by the neutralization of chitosan amino groups.[28] However, the mechanical strength of chitosan is weak, especially under hydrated conditions.[29] We first reported the 3D printing of a chitosan physical hydrogel that involve directly depositing the ink in air to form the structure on a three-axis positioning platform[30] as shown in Scheme 4.1. A 3D-printable chitosan ink with low concentration (8 wt %) was formulated by dissolving chitosan in an acidic mixture. This ink was extruded through micronozzles and directly formed into 3D scaffolds in a layer-by-layer manner via solvent evaporation. Rheological properties of the inks play an important role in the extrusion-based 3D printing methods. For instance, Rutz *et al*. studied the viscous and elastic modulus of gelatin-based inks to acquire the desired degree of crosslinking for 3D printing.[10] Guo *et al*. investigated the process-related apparent viscosity to determine suitable polymer concentration for solvent-assisted 3D printing.[31] The rheological properties of chitosan-based solutions have been widely studied, such as chitosan blends,[32] thermosensitive chitosan-glycerol-phosphate solutions[33] and physical chitosan hydrogel.[34] However, to the best of our knowledge, only a few studies have investigated those in the scope of printability optimization of the inks for 3D printing.
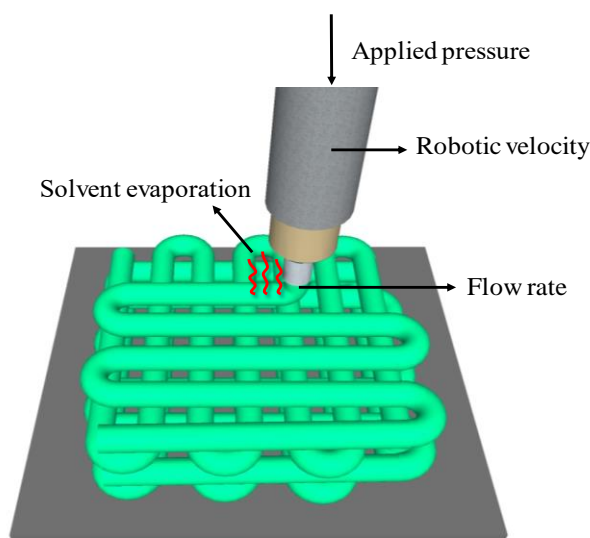
Scheme 4.1: Schematic of the 3D printing process and main process parameters.

In this work, we present a comprehensive study of the properties of chitosan inks for 3D printing at ambient temperature. The rheological properties and flow behavior of the chitosan inks are analyzed to guide the successful 3D printing. The process-related viscosity and flow behavior are characterized by capillary flow analysis. Solvent evaporation kinetics are investigated by observing the weight change of extruded chitosan filaments over time. A processing map is derived by considering parameters for the successful fabrication of one-dimensional (1D), two-dimensional (2D) and 3D chitosan structures. Finally, the tensile properties and XRD patterns of chitosan filaments are investigated.

4.3 Materials and methods

Preparation of Chitosan Inks. Chitosan inks were prepared by dissolving chitosan (90% deacetylated, weight-average molecular weight = 207 kDa, from BioLog Heppe GmbH, Germany) in acidic mixture (40 vol% acetic acid, 20 vol% lactic acid, 40 vol% distilled water). In addition, 3 wt % (based on the total weight of the solution) total citric acid was also added to the mixture. All chemicals were purchased from Sigma-Aldrich, Canada, and used as received. The amount of chitosan and acid solutions were adjusted to obtain different chitosan concentrations (i.e., 6, 8 and 10 wt %). Chitosan solutions were mechanically stirred for 2 h (150 rpm) after resting 12 h. After centrifuging (3000 rpm, 1 h) to eliminate air bubbles, the solutions were stored in sealed bottles in a refrigerator until processing. All solutions were freshly prepared immediately before the 3D printing experiments. The densities of chitosan solutions (i.e., 6, 8 and 10 wt %) were calculated by measuring the mass of 1 mL cubes filled with the solutions. The three solution densities measured are 1.04, 1.1, and 1.2 g/m^3, respectively.

3D Printing. The chitosan ink was inserted in a syringe (3 mL, Nordson EFD). The syringe was then fixed to a high-pressure adaptor (Nordson EFD). The chitosan solution was deposited using a three-axis positioning platform through a micronozzle at room temperature. The ink was extruded under an applied pressure controlled by an air-powered dispensing system (HP-7X, Nordson EFD) and a velocity controlled by a computer assisted robot head (I&J2200-4, I&JFisnar).

Rheological Measurements. Shear viscosities of chitosan solutions were determined using a rotational rheometer (MCR-502, Anton Paar) fitted with a cone and plate flow geometry at shear

rates between 0.1 and 100 s^{-1} at room temperature. The edge of the cone and plate flow geometry was covered with mineral oil to prevent solvent evaporation and it was shown not to affect the tests. Also, process-related viscosity measurements were conducted by capillary flow analysis[35]. Different concentrations of chitosan solutions (6, 8 and 10 wt %) loaded into a syringe (3 mL, Nordson EFD) were extruded through a micronozzle (inner nozzle diameter $D = 200$ µm, capillary length $l = 12.25$ mm, Nordson EFD) under different applied pressures ranging from 0.4 MPa to 3 MPa at a velocity of 0.5 mm s^{-1}. Other micronozzles ($D = 100$ and 330 µm, $l = 12.75$ and 12.25 mm) were also used to extrude the 8 wt % chitosan ink. Chitosan filaments (60 mm long) were dried in vacuum at 55 °C for 72 h and weighed using a high-precision balance (GH-202, A&D Engineering Inc.). Their weight was used to acquire the volumetric flow rates for calculating the process-related apparent viscosity.

Determination of Solvent Evaporation Rate. Chitosan solutions (8 wt %) were prepared by dissolution in different acid solutions (i.e., 40 vol% acetic acid aqueous solution and the acidic mixture described above) and used to investigate solvent evaporation rates. Chitosan filaments (50 mm long) were extruded through a micronozzle ($D = 250$ µm, Nordson EFD) under an applied pressure of ~ 1.3 MPa for 5 s. The weight reduction of the filament was monitored using a high-precision balance (GH-202, A&D Engineering) for 5 h at room temperature. The samples were weighed again after drying under vacuum at 55 °C for 72 h. The solvent evaporation rates were calculated from real-time weight variations (between as-printed filaments and dried filaments), divided by the initial weight of as-printed filaments.

Fabrication of Chitosan Microstructures. 1D, 2D and 3D chitosan microstructures were 3D printed by depositing chitosan filaments in a layer-by-layer manner, where filament solidification was achieved through solvent evaporation. A 8 wt % chitosan ink was used for the fabrication of chitosan scaffolds using a 150 µm micronozzle under an applied pressure of ~1.3 MPa and a velocity of 0.5 mm s^{-1}. The microstructures shaped like a starfish and a leaf were fabricated using a 9 wt % chitosan ink with applied pressures of 1.5 - 2.1 MPa and the velocities of 1 - 2 mm s^{-1}. The files for digital 3D models of starfish and leaf were obtained from Thingiverse (http://www.thingiverse.com/), and a software (Simplify3D) was used to generate codes for 3D printing. The morphological structures of chitosan filaments and 3D-printed scaffolds were observed by scanning electron microscopy (SEM, JSM-840, JEOL). The optical images of 2D and 3D structures were performed using an optical microscope (BX-61, Olympus) and analyzed with

software (Image Pro Plus 6.0, Media Cybernetics). The chitosan structures are dried under vacuum at 55 °C for 72 h for the subsequent neutralization step.

Gelation by Neutralization. After drying, the chitosan scaffolds and the structures shaped-like spiders were immersed in a 1M sodium hydroxide (NaOH) solution for 2 h. After neutralization, samples were washed with distilled water to remove the excess NaOH solution. For analyzing sample surface, the neutralized chitosan scaffold in the dry state was observed by a scanning electron microscope (SEM, JSM-7600, JEOL) and the neutralized scaffold in the wet state was stained using Rhodamine B for 30 min and imaged with a confocal laser scanning microscopy (CLSM) Nikon C2. Rhodamine B stained neutralized scaffolds were observed under a 561 nm laser (Em 561LP).

X-ray Diffraction (XRD). To investigate the crystallinity of samples based on different processing histories, XRD patterns of chitosan powder, as-printed and neutralized filaments in dry state were obtained using a Philips X'Pert X-ray diffractometer equipped with a Cu−Kα radiation, and operated at 50 kV and 40 mA. The diffraction was measured in a range from 5° to 35° with a step width of 0.02° and a scan speed of 0.02° min^{-1}.

Tensile Tests of Chitosan Filaments. Tensile tests on chitosan filaments in different states (i.e., as-printed filaments, filaments after drying for 72 h and neutralized filaments in dry and wet states) were performed using an electromechanical machine (Insight MTS 50kN) with a 100 N load cell. Tests were repeated seven times using the standard of ASTM D3822 / D3822M.

4.4 Results and discussion

Flow Properties. The chitosan inks must exhibit appropriate rheological properties to enable efficient flow through micronozzles for successful 3D printing. The flow behavior of different chitosan inks prepared using acidic mixture during their extrusion through a 200 µm micronozzle was examined by capillary flow analysis[35-36]. Figure 4.1 presents the volumetric flow rate (converted from mass flow rate) of different chitosan solutions (i.e., 6, 8, and 10 wt %) and different nozzles (i.e., 100, 200 and 330 µm) with respect to the applied pressure. Figure 4.1a shows that the volumetric flow rates for all chitosan solutions increased with applied pressure. For a given flow rate, higher pressures were required to allow flow of higher concentrated inks in the micronozzle. Figure 4.1b shows the variation of the ink flow rate when using micronozzles of different

diameters. We observe that for a given pressure the flow rates also increased with nozzle diameter, as expected.
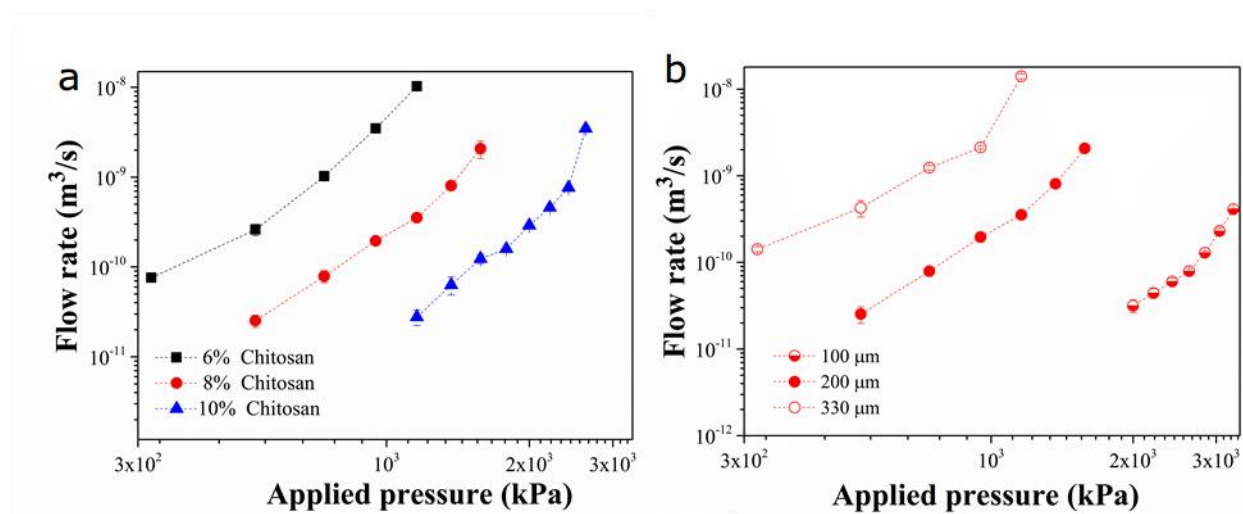
Figure 4.1: Volumetric flow rate as a function of applied pressure for (a) various chitosan inks (6, 8 and 10 wt %) deposited using a 200 µm nozzle, and (b) a 8 wt % chitosan ink extruded using different micronozzle diameters (100, 200 and 330 µm). All inks were prepared using an acidic mixture (40 vol% acetic acid, 20 vol% lactic acid, and 3 wt % citric acid).

Figure 4.2 shows the viscoelastic properties of the chitosan solutions at different concentration (6, 8, and 10 wt %). The process-related apparent viscosities of different chitosan inks (i.e., 6, 8, 10 wt %) were calculated from the capillary flow data with respect to the applied pressure and are presented by solid symbols in Figure 4.2a. All solutions exhibited a pronounced shear thinning response as evidenced by an important decrease in viscosity. For example, the apparent viscosity of the 8 wt % ink at a shear rate of ~800 s^{-1} is ~8 Pa·s and nearly three orders of magnitude smaller than the viscosity of ~1500 Pa·s measured by rotational rheometer in low shear conditions. The shear-thinning behavior can benefit the flow through the deposition micronozzle.[37] After exiting the micronozzle, the shear stress is relieved and the ink viscosity increases again, which helps to keep its filamentary shape. The open symbols in Figure 4.2 present the viscosity of different

chitosan concentrations (i.e., 6, 8, 10 wt %) obtained through rotational rheometry with respect to the shear rate. These viscosity measurements were also obtained at room temperature and under steady simple shear. The 6 and 8 wt % chitosan solutions presented a Newtonian behavior at low shear rate (≤ 0.5 s^{-1}) while the viscosity of the 10 wt % chitosan solution did not show a Newtonian plateau in this investigated range of shear rates. Under the same shear rate, the viscosity of the inks increased with ink concentration, as expected, which will affect 3D printability.

The dashed curves in Figure 4.2 represent the fitted values for shear rates obtained from the
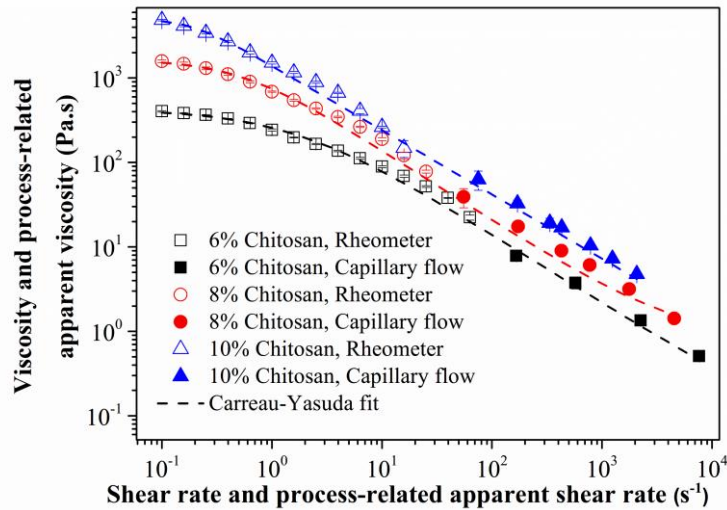
Figure 4.2: Viscosity with respect to shear rate for different chitosan inks prepared using the acidic mixture: 40 vol% acetic acid, 20 vol% lactic acid, and 3 wt % citric acid (open symbols: data obtained using a cone and plate flow geometry in steady shear; solid symbols: data obtained by extruding chitosan filaments and capillary flow analysis). The dashed curves are fits from the Carreau-Yasuda model where the parameters used are listed in Table 4.1.

Carreau-Yasuda model described as

$$\frac{\eta - \eta_\infty}{\eta_0 - \eta_\infty} = [1 + |t_1\dot{\gamma}|^a]^{(n-1)/a}$$

where η_0 is the zero-shear-rate viscosity, η_∞ is the infinite-shear-rate viscosity, t_1 is a characteristic time constant, n is the power law exponent, and a is dimensionless parameter

that controls the width of the transition between the zero-shear-rate and power-law regions. The fitting parameters of the equation are reported in Table 4.1.

Table 4.1 Parameters of the Carreau−Yasuda Model for the various chitosan solutions

Chitosan (wt %)	η_0 (Pa·s)	t_1 (s)	a	n	R^2
6	452	0.52	0.72	0.17	0.97
8	1997	1.88	0.81	0.16	0.95
10	5807	5.33	1.35	0.13	0.96

The curves in Figure 4.2 show an accurate fit of the Carreau-Yasuda model, with reasonable agreement between the viscosities obtained from both the rotational rheometry and the capillary flow analysis. According to the values listed in Table 4.1, η_0 of higher concentrated chitosan solutions is larger. Thus, the shear thinning behavior increases with chitosan concentration and the transition from Newtonian to shear-thinning occurs at lower shear rates. In addition, our data shows that chitosan solutions obey Cox-Merz rule (Figure S4.1, Supporting Information) on a large range of frequencies. Therefore, the linear viscoelastic data can be used to infer the level of elasticity at various apparent processing shear rates. Figure S4.2 (Supporting Information) compares the behavior of viscoelastic properties to extrudate die swell and filament sizes. Figure S4.2a shows the elastic (G') and viscous (G'') moduli of chitosan solutions at different concentrations. G'' is higher than G' in all solutions at low frequencies, followed by $G'' < G'$ after the cross-over point, which is typical of viscoelastic liquids. The 10 wt % chitosan solution exhibits a cross-over point at a relatively lower frequency (1.8 rad/s) as compared to the chitosan solutions of 6 and 8 wt % (24 rad/s and 6.6 rad/s, respectively), which represents a longer relaxation time and hence a more elastic character. The effects of polymer concentration on die swell and filament size were investigated when the solutions were extruded under the same applied pressure (530 kPa) (Figure S4.2 b-d, Supporting Information). It can be seen that higher chitosan concentration leads to an increase in die swell ratio due to higher level of molecular entanglement, which in turn results in larger filament size. Figure S4.2 e-f (Supporting Information) shows the effect of the extrusion pressure on die swell and filament size when an 8 wt % chitosan solution is extruded under different applied pressures (390, 530 and 670 kPa). The

die swell ratios and filament sizes increase with extrusion pressure, since the chitosan molecules are more aligned under higher pressure, and once extruded out of the nozzle to a low stress environment, tend to relax to a greater extent. Figure S4.2d shows that a filament fabricated from a 10 wt % chitosan solution under 530 kPa exhibits strong elasticity, as manifested by flow instability. To avoid process instability, moderate chitosan concentration and pressure (e.g., 8 wt %, 1.2 MPa) were used to avoid flow- and elasticity-driven instabilities. Proper adjustment of platform movement (filament pulling) can also compensate for swelling and result in reasonable diameter of chitosan filaments.

Accurate printing requires adequate rheological properties, and the precise control of the applied pressure with respect to the robotic velocity for the different ink and micronozzle combinations. Figure 4.3a shows the average velocity of the ink flow as a function of the applied pressure for different chitosan solutions (i.e., 6, 8, 10 wt %) deposited using a 200 µm micronozzle. The velocity was calculated by dividing the volumetric flow rate by the area of the micronozzle cross-section. As the concentration of chitosan solutions increased, higher pressures were necessary to generate the flow due to higher viscosity of the inks. Figure 4.3b shows the average velocity with respect to the applied pressure for the same chitosan solution (i.e., 8 wt %) extruded through different nozzles (i.e., 100, 200, and 330 µm). For the same velocity, the applied pressure for the 100 µm nozzle was approximately 5 times larger than that of the 330 µm. In addition, the inks started flowing through
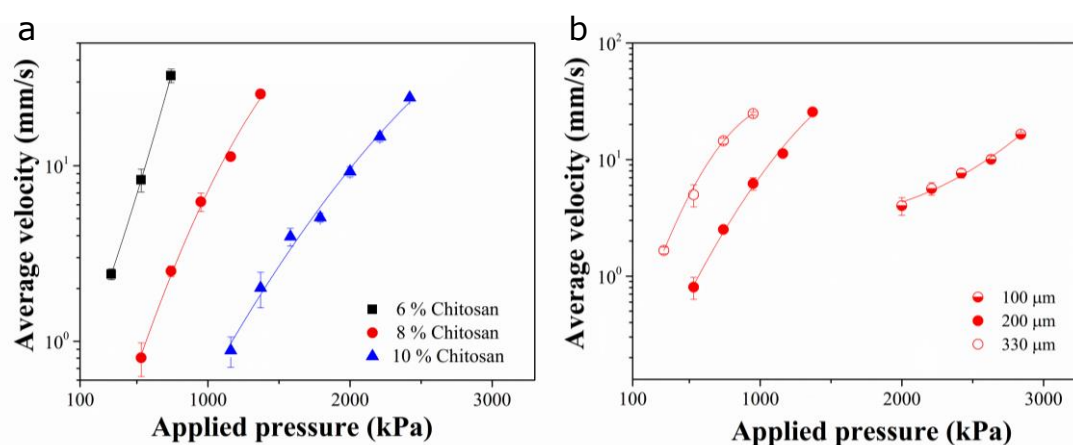
Figure 4.3: Average velocity of ink flow as a function of applied pressure for (a) chitosan solutions (6, 8 and 10 wt %) and (b) a 8 wt % chitosan solution extruded through different micronozzles (diameters: 100, 200, and 330 µm). All the inks were prepared using acidic mixture (40 vol% acetic acid, 20 vol% lactic acid, and 3 wt % citric acid).

the micronozzle only once a minimum pressure was applied, indicating the existence of an apparent yield stress.

Solvent Evaporation. During the 3D printing process used in this work, extruded chitosan filaments gradually solidify after extrusion due to solvent evaporation. To evaluate the effect of solvent evaporation during fabrication, two inks composed of 8 wt % chitosan prepared using the acidic mixture and an acetic acid solution (40 vol% acetic acid) were printed. The solvent evaporation rates were measured by monitoring the weight change of chitosan filaments (50 mm long, extruded using a 250 µm micronozzle) for 5 h using a high-precision balance at room temperature. Figure 4.4 shows the percentage of solvent content as a function of time. The acetic acid solution (slope $|k|$ of 0.018 s^{-1}) evaporated slightly faster than the acidic mixture ($|k|$ of 0.01 s^{-1}) in the first half hour, then both inks slowly evaporated after ~1 h. The filaments retained a lower content (~ 20 wt %) of solvent after 5 h of evaporation when using the acetic acid solution, as opposed to the one prepared with the acidic mixture (~ 45 wt %). Acetic acid is more prone to evaporation into air, because it has a much higher vapor pressure (i.e., 15.7 mm Hg at 25 °C) than lactic acid and citric acid (i.e., 0.0813 mm Hg and 1.7 $\times 10^{-8}$ mm Hg at 25 °C, respectively). The acidic mixture containing low vapor-pressure solvent (i.e., lactic acid) and non-volatile citric acid is unable to completely evaporate over time, which results in more residual solvent (~45 wt % after 5 h) in the filaments. The acidic mixture exhibits appropriate solvent evaporation rate for 3D printing and the residual solvent in the filament can minimize the drying-induced shrinkage. Due

to the drying induced shrinkage of the ink using the acetic acid solution, the ink prepared using the acidic mixture was used preferentially for the fabrication of different structures.

3D Printing of Microstructures. Figure 4.5 shows the process map of chitosan inks based on the acidic mixture for 3D printing. This map illustrates the range of nozzle diameters and chitosan contents appropriate for the fabrication of different types of patterns: 1D filament, 2D network, or 3D microstructures. High shape fidelity of those structures also requires the appropriate adjustment between evaporation rate and printing parameters. Chitosan solutions with different concentrations (from 4 to 12 wt %) and six nozzles (D = 100, 150, 200, 250, 330, and 510 μm) were used in this processing map. The applied pressure (from 0 to 4.1 MPa) and robot velocity (from 0.1 to 500 mm s^{-1}) were investigated for printing. Successful printing was demonstrated through observing 3D-printed structures (e.g., smooth and continuous 1D filament, filament diameter is close to nozzle diameter in 2D arrays, self-support features without sagging in 3D structures). Zone I in Figure 4.5
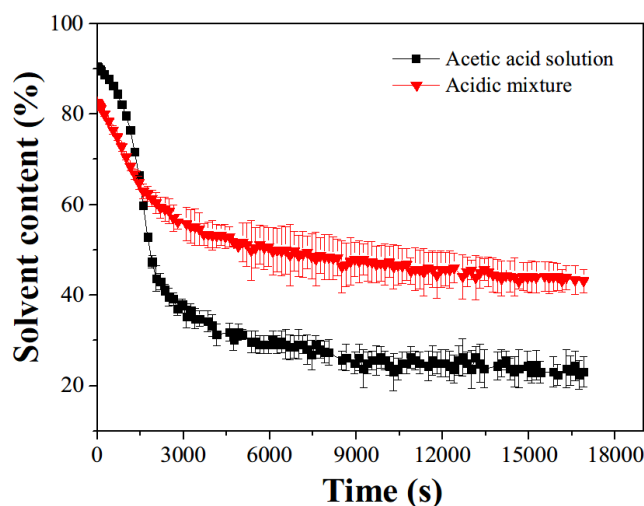
Figure 4.4: Solvent content as a function of time for 8 wt % chitosan solutions dissolved in two different solutions (i.e., acetic acid solution: 40 vol% acetic acid; acidic mixture: 40 vol% acetic acid, 20 vol% lactic acid, and 3 wt % citric acid).

reveals that chitosan inks (approximately from 5 to 11 wt %) can readily flow through micronozzles (D= 30 ~ 500 μm) to form 1D filaments. Zone II represents the ability to fabricate 2D filament arrays and 3D chitosan layer-by-layer structures at high resolution (30 μm). For nozzle sizes that exceed 330 μm, we observed that the structures collapsed. Zone III shows the range of larger nozzle diameters for which the imposed shape was difficult to maintain after fabrication for all the chitosan content investigated. It was also difficult to fabricate structures using both too dilute (Zone VI, the

concentration of chitosan ink < 4 wt %) or too viscous chitosan solutions (Zone V, the concentration of chitosan ink > 11 wt %). The optimal viscosity for the chitosan solution for 3D printing is low enough to be extruded through the micronozzle and also high enough to maintain its shape after printing.

Different chitosan microstructures were fabricated using the parameters corresponding to letters a-e illustrated in Figure 4.6. Figure 4.6a shows a SEM image of a 1D filament with a diameter (*d*) of ~ 90 µm featuring a very smooth surface which was extruded through a 100 µm nozzle with a 6 wt % chitosan solution. The final dimension of the filament is determined by a combination of ink concentration, nozzle diameter, applied pressure (*P*), robotic velocity (*V*) and solvent evaporation. Figure 4.6b presents a fluorescent microscopy image of a 2D filament array in a top view, which was fabricated using a 8 wt % chitosan solution with fluorescent dye (*D* = 30 µm, *V* = 1 mm s^{-1}, *P* = 1.1 MPa). Figure 4.6c shows a top and side view of a 3D chitosan scaffold with a circular morphology of the filaments between interconnected layers, featuring a pore size (*Ps*) of ~220 µm
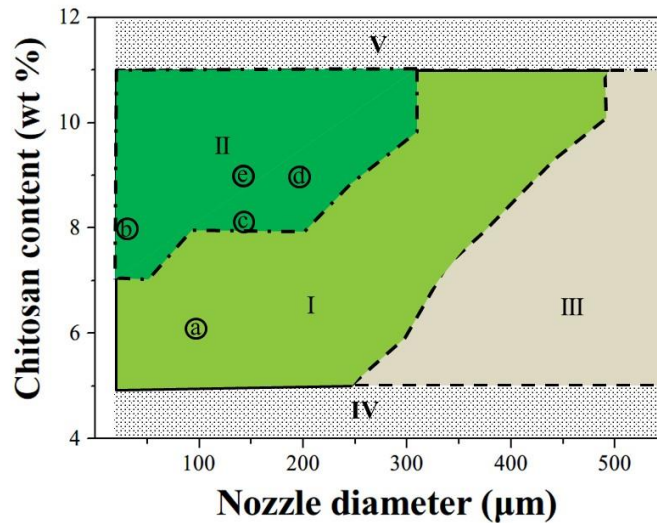
Figure 4.5: Process map illustrating the ranges of chitosan contents and nozzle diameters compatible for the fabrication of various types of microstructures. I: zone for 1D filament, II: zone for 2D filament array or 3D structure, III: zone where chitosan solutions lose shape fidelity, IV: zone where chitosan solutions are too dilute for the process, V: zone where chitosan solutions are too viscous to be printed. The letters a-d represent the fabrication parameters of different structures shown in Figure 4.6. Solvent used is the acidic mixture.

and 30 layers (*L*), fabricated using a 8 wt % chitosan solution (*D* = 150 µm, *V* = 0.5 mm s^{-1}, *P* =

1.3 MPa). After drying under vacuum at 55 °C for 72 h, the filament diameter in the scaffold shrank to ~ 60 % of that of an as-printed scaffold, indicating that solvent occupied ~ 40 % of the filament volume in the as-printed filament. A 9 wt % chitosan ink was used to fabricate a starfish shaped-like structure (D = 200 µm, V = 1 mm s^{-1}, P = 1.5 MPa). As shown in Figure 4.6d, the top and side view of the starfish (L = 17) presented a high shape fidelity with surface patterns. Figure 4.6e shows a 3D printed leaf with detailed main and branch lines and a thickness of ~ 300 µm, which was fabricated using a 9 wt % chitosan ink (D = 150 µm V = 2 mm s^{-1}, P = 2.1 MPa). The insets in Figure 4.6b-e show computer-aided design (CAD) images of each 3D-printed structures. Comparison between the optical or SEM images in Figure 4.6b-e and the CAD images shows the dimensional fidelity of the 3D printing process. Those images demonstrate the versatility and flexibility of the 3D printing method to fabricate different structures from an aqueous-based chitosan solution and map the adequate selection of process and material parameters.
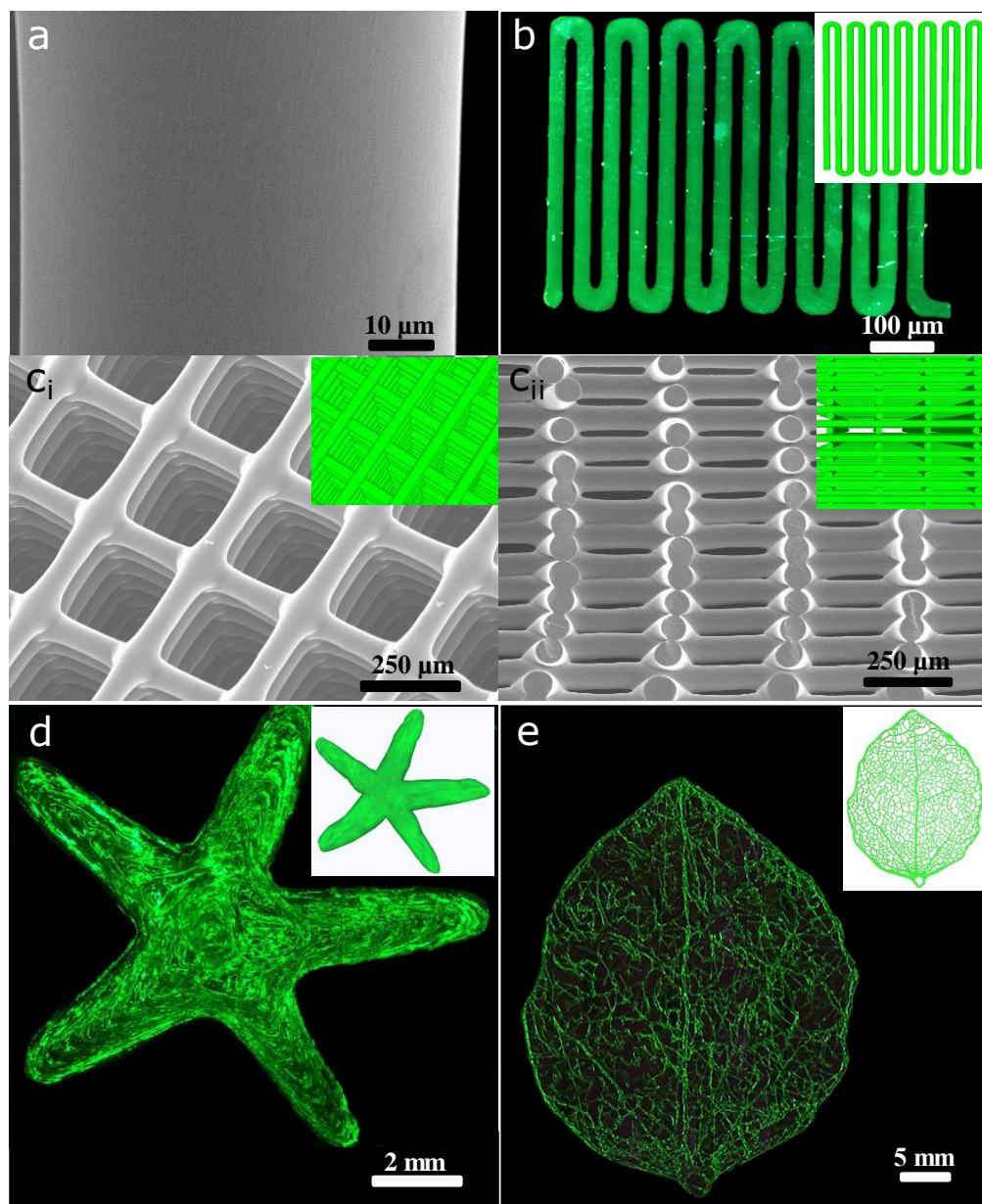
Figure 4.6: (a) close-up SEM image of a chitosan filament, (b) fluorescent microscopy image of a 2D chitosan network, (c) SEM image of a 3D chitosan scaffold with square pore size with top and side views, (d) fluorescent microscopy image of a 3D printed starfish, (e) fluorescent microscopy image of a 3D printed leaf. Inset images in b, c, d and e show CAD models of the 2D network, scaffold, starfish and leaf structures.

Dimensional Stability of 3D-printed Structures. To exhibit the successful printing of the ink prepared using the acidic mixture, the dimensional stability of different 3D structures after printing was investigated. A 10 wt % chitosan ink prepared using the acetic acid solution was used for comparison, considering the difficulty of printing 3D structures from this ink with a chitosan concentration lower than 10 wt %. Figure 4.7 shows the effect of the shrinkage after printing on the dimension of complex 3D chitosan structures at room temperature over time. Figure 4.7a and f shows CAD images of a shape-like spider structure. Figure 4.7 b-e shows fluorescent microscopy images of "spiders" fabricated using a 10 wt % ink with an acetic acid solution after printing for 0, 1, 4, and 28 h. Obvious shrinkage was observed after 1 h printing of the structure. Figure 4.7 g-j shows "spiders" fabricated using a 10 wt % ink with an acidic mixture, exhibiting a high shape retention with a slight shrinkage after printing for 28 h. To quantitatively study the shrinkage behavior post printing, 30-layer scaffolds were fabricated using the two different inks. Comparison between a CAD scaffold model (Figure 4.7k) and a 3D-printed scaffold (width and length: 8 mm × 8 mm, T = 3 mm) fabricated using an ink (10 wt %) based on the acetic acid solution (Figure 4.7l) demonstrate that the 3D-printed scaffold loses its shape. The shrinkage of the scaffolds was quantified using an optical microscope to monitor the relative width and thickness reduction of the scaffolds over 28h. Figure 4.7n shows the normalized dimension change of the scaffolds fabricated using the two inks. The thickness and width of the scaffolds prepared using the acetic acid solution reduced fast, with both values at ~65% after 28 h. In contrast, the scaffolds obtained with the acidic mixture were gradually reduced to 90% and 82% after 28 h. These shrinkage percentages demonstrate that the structures fabricated with the ink prepared from the acidic mixture can maintain higher shape fidelity compared to the ink using acidic acid only. The dimensional stability of 3D-printed structures is especially important for the fabrication of larger structures with longer fabrication time.
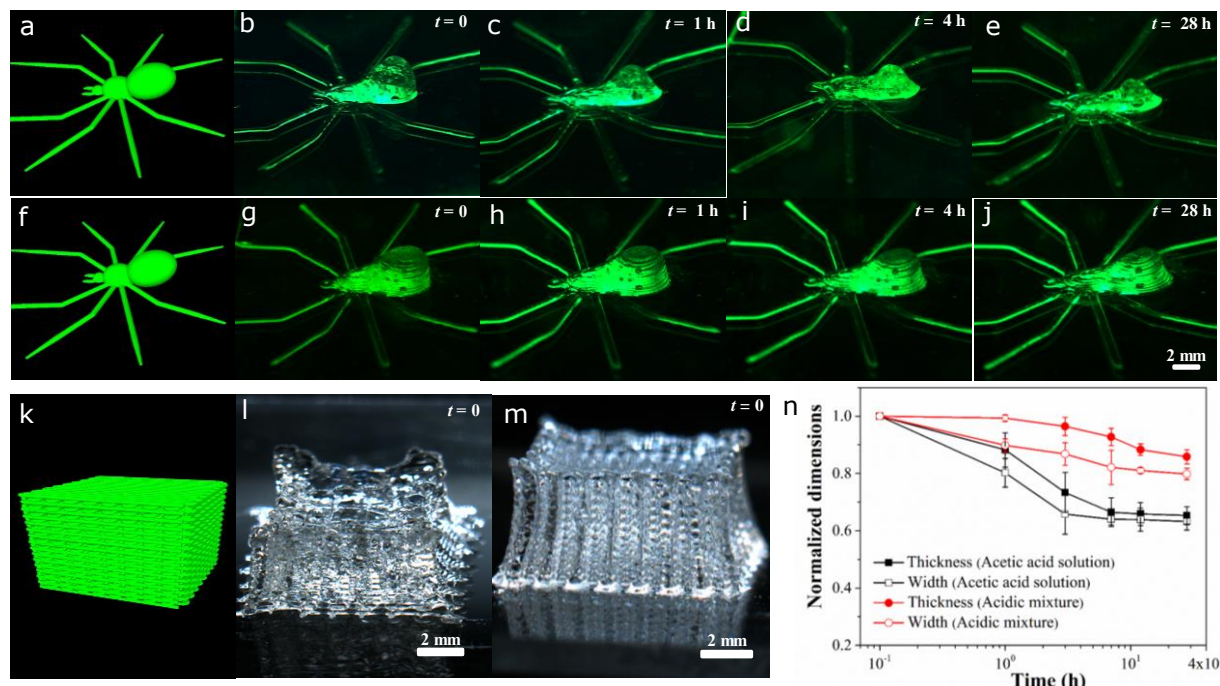
Figure 4.7: (a) and (f) CAD models of a shaped-like spider structure. (b-e) Fluorescent microscopy images of "spiders" fabricated using a 10 wt % ink with an acetic acid solution and (g-j) a 10 wt % ink with the acidic mixture after printing 0, 1, 4, and 28 h. (k) CAD model of the scaffold. (l) An as-printed 30-layer chitosan scaffold fabricated using a 10 wt % ink with the acetic acid solution using 200 µm nozzle and (m) a scaffold fabricated using a 10 wt % ink with the acidic mixture under the same fabrication conditions. (n) The width and thickness reductions of the scaffolds fabricated using chitosan inks (10 wt %) with the acetic acid solution and acidic mixture in Figures l and m over a period of 28 h.

Gelation by Neutralization. After the 3D printing of chitosan microstructures, the chitosan constructs are dried under vacuum at 55 °C for 72 h. A neutralization step was used to remove the residual acid in the structures and obtain a stable hydrogel. The modulus of neutralized chitosan films was measured using DMA, showing that a hydrogel was formed after neutralization (Figure S4.3, Supporting Information). Figure 4.8 shows the variation of the morphology of chitosan scaffolds during the different processing steps. Figure 4.8a shows an as-printed scaffold 24 h after printing made of fine and smooth filaments ($d = 90$ µm, $Ps = 350$ µm). After the neutralization in a NaOH solution (1M) and drying for 4 h in vacuum, an important shrinkage in the neutralized scaffold ($d = 60$ µm, $Ps = 180$ µm) with wrinkled surface is observed in Figure 4.8b. When the neutralized scaffold re-absorbs water, the interconnected structure is still maintained, as shown in

Figure 4.8c with 3D reconstruction of confocal images. A close up view of the filament surface in Figure 4.8c shows oriented wrinkles that were almost perpendicular to the cross section of the filament. The shrinkage of the neutralization step and drying process is the main cause for the wrinkles on the surface. During the neutralization step, NH_3^+ groups are deprotonated to NH_2
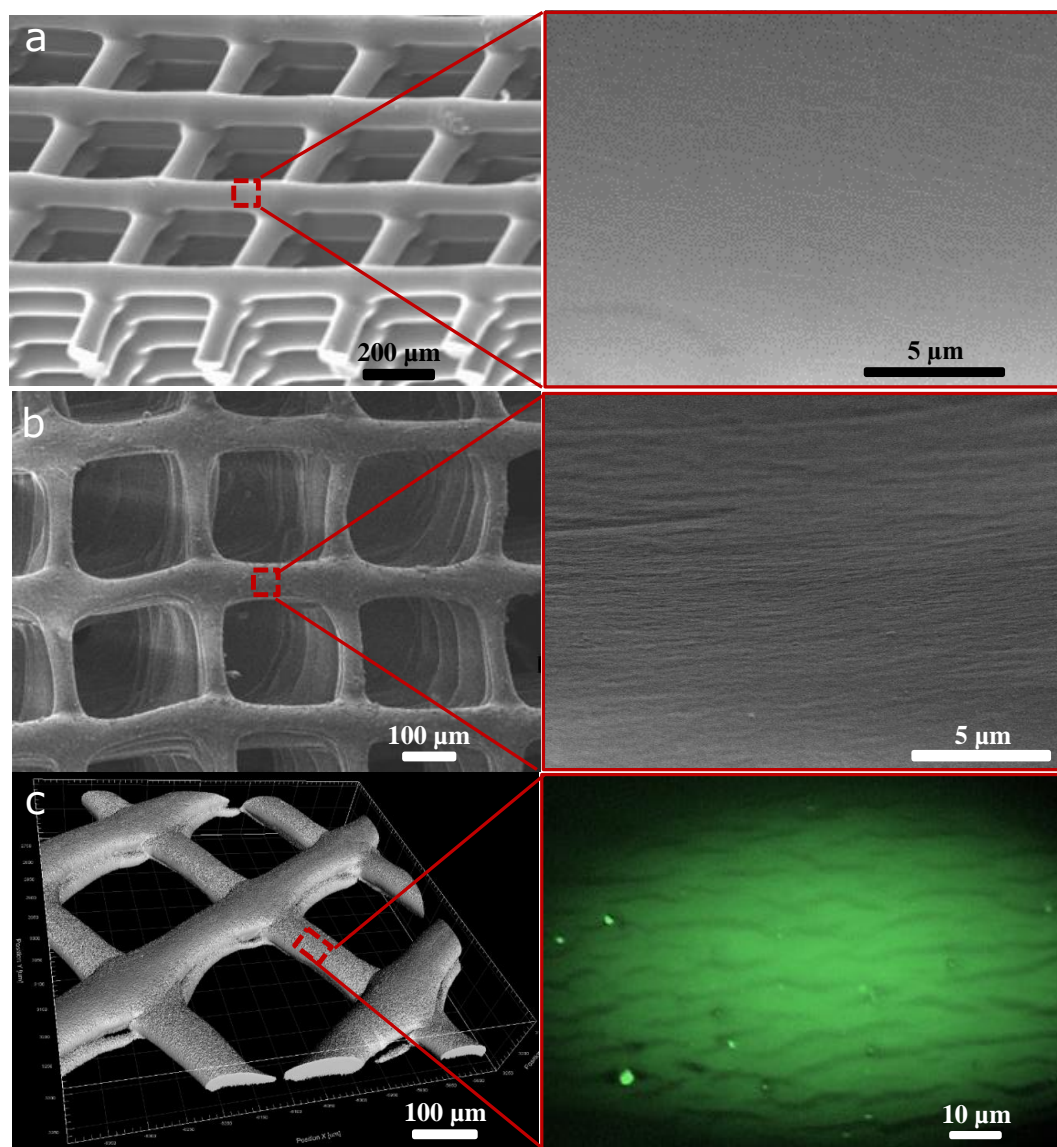
Figure 4.8: (a) SEM images of a 3D printed chitosan scaffold 12 h after printing, and a close-up view of the surface of the filament in the red frame area. (b) SEM images of a neutralized scaffold in the dry state, and a close-up view of the filament featuring longitudinal wrinkles in the red frame area. (c) Confocal images of a neutralized scaffold in the wet state, and fluorescent confocal image of the filament texture in the red frame area.

groups due to the sudden change in pH, yielding the disappearance of ionic repulsion between chitosan chains and favouring chain packing and gel shrinkage.[28]

Physical Characterization of Different Processing. To investigate the effect of different processing on material properties, the microstructure and mechanical properties of chitosan were observed by XRD and tensile testing. Figure 4.9 shows the XRD patterns of chitosan powder and chitosan filaments after different processing steps. Two characteristic diffraction peaks at $2\theta = 10°$ and 19.9° were observed for the chitosan powder, representing the 020 and 100 planes in hydrated chitosan crystals.[38] Compared with native chitosan, chitosan filaments prepared using an acidic mixture are more amorphous because there is no diffraction peak at $2\theta = 10°$ and generated a broader diffraction peak at $2\theta = 21°$. This result implies that the lactic acid and citric acid molecules remained after drying in the filaments, incompletely disrupting the crystalline domains in chitosan, due to possible interactions between the amino groups on chitosan and the carboxyl groups in citric acid and lactic acid.[39] After neutralizing and drying the filament fabricated using the ink with the acidic mixture, two characteristic diffraction peaks at $2\theta = 9.9°$ and 19.7° were exhibited again from the chitosan filaments, which were similar to that of chitosan powder. These peaks reveal that the crystalline degree increased after neutralization. Neutralized filaments with similar configuration as native chitosan has stronger molecular forces than amorphous chitosan[40-41], and stronger molecular forces can help to obtain higher mechanical properties.
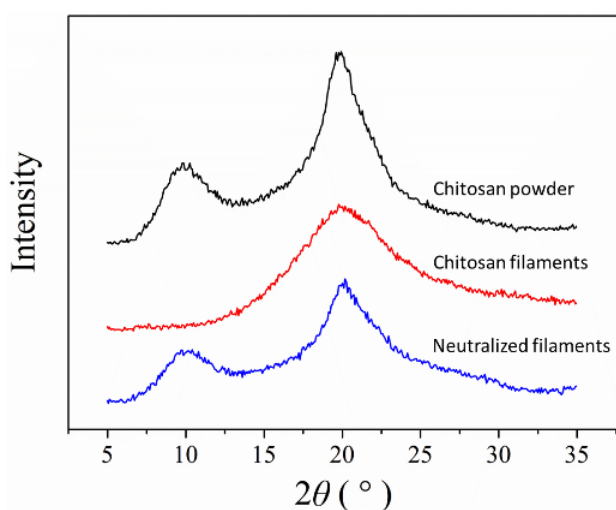
Figure 4.9: X-ray diffraction patterns. Comparison of chitosan powder, dried chitosan filaments printed using the acidic mixture (40 vol% acetic acid, 20 vol% lactic acid, and 3 wt % citric acid), and dried chitosan filaments prepared using the same acidic mixture after neutralization.

The tensile properties of chitosan filaments were investigated with specimens fabricated by 3D printing with a 8 wt % chitosan ink prepared using the acidic mixture. Figure 4.10a shows representative stress-strain curves of chitosan filaments after different processing steps. The as-printed chitosan filaments (*3P*) present a strength at break of ~ 1.6 MPa and the value of the printed filaments after drying (*3P-D*) to allow evaporation of most solvent for 48 h increase to ~ 12 MPa. After neutralization, the neutralized chitosan filaments in the wet state (*N-W*) show a strength at break of ~ 6 MPa and the neutralized chitosan filaments in the dry state (*N-D*) present a strength at break of ~ 95 MPa. The *N-D* filaments show much higher maximum strength than chitosan films fabricated by the reference methods such as solvent casting (*Sc-D,* ~ 33 MPa)[42-44] and cryogenically 3D plotted chitosan (*Cp-D,* ~ 0.2 MPa),[17] as shown in Figure 4.10b. Figure 4.10c shows *3P* filaments have a high strain at break (~ 170%), while the strain at break of *3P-D* filaments decrease to ~ 5%, due to the residual solvent in 3P filament that make it more flexible. After neutralization, the strain at break of *N-D* filaments is higher than *3P-D*. *3P-W* filaments shows a very high stretchability of ~ 360%, which is also much higher than the values in the references.[42, 45] Figure 4.10d shows that Young's modulus of *N-D* filaments (~ 2310 Pa) is higher than that of *3P-D* (~ 102 MPa), while both *3P* and *N-W* are soft with a Young's modulus of ~ 2 MPa. Therefore, *N-D* filaments have higher tensile properties compared to *3P-D* filaments, due to a stable hydrogel and crystallite formation after neutralization, as observed with the XRD results shown in Figure 4.9.

The comparison of the tensile properties of chitosan fabricated using our approach and other techniques including solvent casting,[42-44] cryogenically 3D plotting,[17] and electrospinning[45-46] reveals that 3D-printed chitosan filaments produced in this work exhibit improved tensile properties, due to optimized formulations of chitosan inks and the fabrication method.
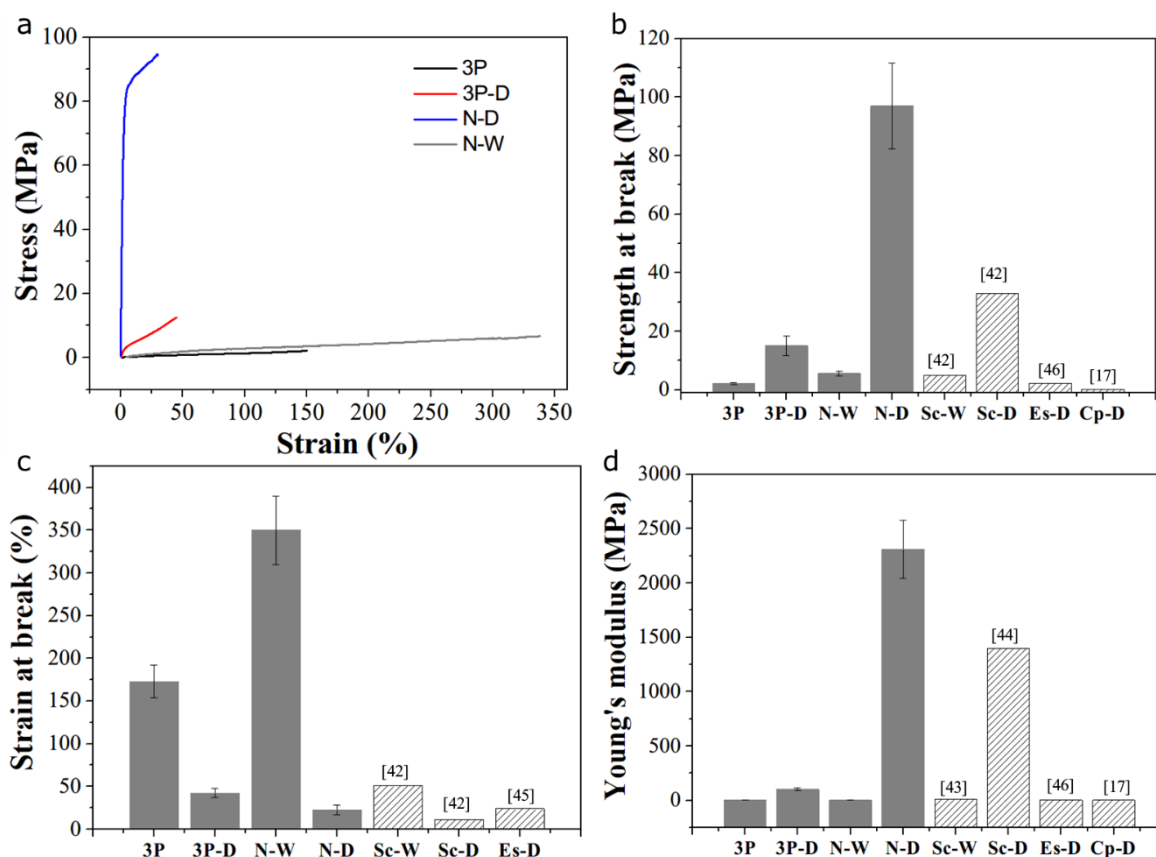
Figure 4.10: (a) Typical stress-strain curves for chitosan filaments after different processing steps (*3P*: as-printed chitosan, *3P-D*: printed chitosan 72 h after drying, *N-W*: neutralized chitosan in the wet state, *N-D*: neutralized chitosan in the dry state). (b) Tensile strength at break, (c) strain at break, and (d) Young's modulus of chitosan filaments, compared with the chitosan fabricated by other methods including solvent-cast chitosan in wet state (*Sc-W*) and in dry state (*Sc-D*), electrospun chitosan in dry state (*Es-D*), and cryogenically 3D plotted chitosan (*Cp-D*). A 8 wt % chitosan ink prepared using the acidic mixture was used to fabricate the chitosan filaments.

4.5 Conclusion

In this work, we investigated the 3D printing process of chitosan inks that were directly printed in air at room temperature. Ink characteristics including rheological properties (e.g. shear-thinning behavior) and solvent evaporation as well as operating conditions (e.g. applied pressure, robot velocity) were examined for successful fabrication. 3D chitosan scaffolds and complex shapes such

as starfish and leaf with high shape fidelity were fabricated using a natural polymer directly in air and at room temperature for the first time. Chitosan hydrogel microstructures with wrinkled surfaces were obtained through a neutralization step. Excellent mechanical properties of physical chitosan hydrogel (e.g., high maximum strength at break ~ 97 MPa of a neutralized filament in dry state and high strain at break ~ 360% of a neutralized filament in wet state) were obtained. Additional experiments would be required to fully investigate the relationship between residence time of the various inks in the micronozzles, their relaxation characteristics and the shape fidelity of the printed structures. The novel approach presented here provides new opportunities to pattern other soft naturally-derived polymer and nanocomposite inks with complex structures, using a clean fabrication process (i.e., without using toxic chemicals), with high resolution (~ 30 µm), high shape fidelity, easy operational mode (i.e., direct printing at room temperature), and high strength for bioengineering, industrial and biomedical applications.

4.6 Acknowledgements

4.7 Supporting information

Rheological measurements. Dynamic rheological properties of the chitosan solutions (6, 8 and 10 wt %) were measured using a rotational rheometer (MCR-502, Anton Paar) fitted with a cone and plate flow geometry at frequencies ranging from 0.1 to 120 rad/s in the linear viscoelastic regime at room temperature, under a strain of 0.2 %. Complex viscosity is compared to shear viscosity in Figure S4.1. Cox-Merz rule applies well for the three solutions in the low to moderate frequency range. Deviations appear in the frequency range that corresponds to the operational process-related apparent shear rate. The dynamic data is nevertheless used to infer the effect of elasticity (G') on the inks printability. It is compared to die swell in Figure S4.2, where die swell of the chitosan

solution extrudates (6, 8 and 10 wt %) was observed using an optical microscope (BX-61, Olympus).
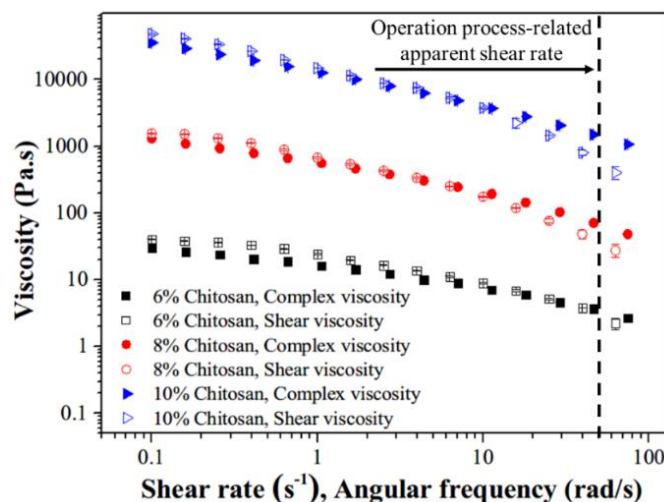
Figure S4.1: Shear viscosity and complex viscosity of chitosan solutions (the viscosity values of the 6 wt % chitosan solution are reduced tenfold and the values of the 10 wt % chitosan solution are increased tenfold for readability). The zone to the right of the vertical dashed line represents the operational process-related apparent shear rates used.
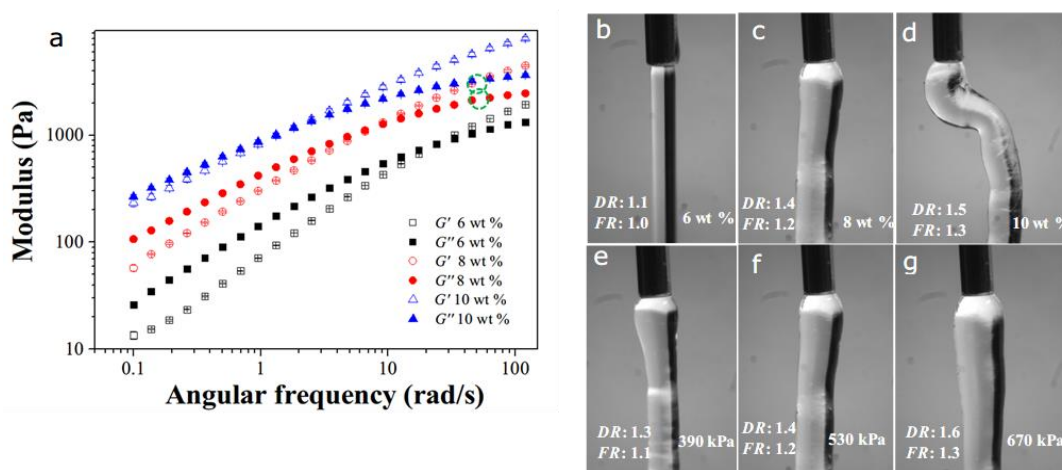
Figure S4.2: (a) Elastic (G') and viscous (G'') shear moduli of chitosan solutions (6, 8 and 10 wt %). The green circles represent G' and G'' of the 8 wt % ink extruded under an applied pressure of 530 kPa (corresponding to a process-related apparent shear rate of 55.2 s^{-1}). The shear rate is calculated by capillary flow analysis.[28] (b-d) Microscope images of extrudates of chitosan solutions (6, 8 and 10 wt %) under an applied pressure of 530 kPa, and (e-g) 8 wt % chitosan ink extruded under different pressures. Die swell ratio (DR) = filament diameter/nozzle diameter, filament size ratio (FR) = filament/nozzle diameter.

Dynamic mechanical analysis. The storage and loss moduli of neutralized chitosan films were measured at room temperature by a dynamic mechanical analyzer (DMA, Q800, TA Instruments) using compression clamps. Samples were fabricated by 3D printing into small circular films using a 8 wt % chitosan ink prepared using the acidic mixture. After neutralization, films (D = 15 mm, T = 1.5 mm) were tested at a strain of 1% and frequency sweep from 1 to 30 Hz. The results show that a chitosan physical hydrogel is obtained after neutralization.
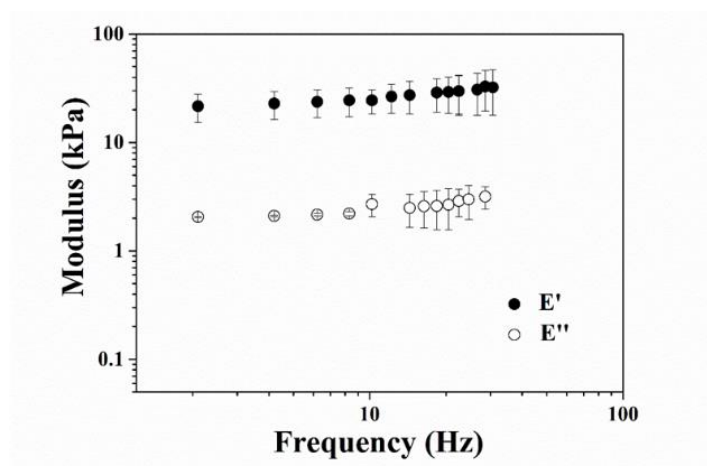
Figure S4.3: Dynamic compression moduli E' and E'' of chitosan films after neutralization post-processing, obtained in DMA using a strain of 1% and compression clamps.

References

[1]   J. M. Dang and K. W. Leong, "Natural polymers for gene delivery and tissue engineering," *Advanced drug delivery reviews,* vol. 58, pp. 487-499, 2006.

[2]   Y. Cai, J. Li, C. K. Poh, H. C. Tan, E. San Thian, J. Y. H. Fuh*, et al.*, "Collagen grafted 3D polycaprolactone scaffolds for enhanced cartilage regeneration," *Journal of Materials Chemistry B,* vol. 1, pp. 5971-5976, 2013.

[3]   M. Guvendiren, J. Molde, R. M. Soares, and J. Kohn, "Designing biomaterials for 3D printing," *ACS biomaterials science & engineering,* vol. 2, pp. 1679-1693, 2016.

[4]   J. U. Lind, T. A. Busbee, A. D. Valentine, F. S. Pasqualini, H. Yuan, M. Yadid*, et al.*, "Instrumented cardiac microphysiological devices via multimaterial three-dimensional printing," *Nature materials,* 2016.

[5]   J. S. Miller, K. R. Stevens, M. T. Yang, B. M. Baker, D.-H. T. Nguyen, D. M. Cohen*, et al.*, "Rapid casting of patterned vascular networks for perfusable engineered three-dimensional tissues," *Nature materials,* vol. 11, pp. 768-774, 2012.

[6]   T. Q. Huang, X. Qu, J. Liu, and S. Chen, "3D printing of biomimetic microstructures for cancer cell migration," *Biomedical microdevices,* vol. 16, pp. 127-132, 2014.

[7]   L. Mogas-Soldevila, J. Duro-Royo, and N. Oxman, "Water-Based Robotic Fabrication: Large-Scale Additive Manufacturing of Functionally Graded Hydrogel Composites via Multichamber Extrusion," *3D Printing and Additive Manufacturing,* vol. 1, pp. 141-151, 2014.

[8]   T. J. Hinton, Q. Jallerat, R. N. Palchesko, J. H. Park, M. S. Grodzicki, H.-J. Shue*, et al.*, "Three-dimensional printing of complex biological structures by freeform reversible embedding of suspended hydrogels," *Science advances,* vol. 1, p. e1500758, 2015.

[9]   T. J. Hinton, A. Hudson, K. Pusch, A. Lee, and A. W. Feinberg, "3D printing PDMS elastomer in a hydrophilic support bath via freeform reversible embedding," *ACS biomaterials science & engineering,* vol. 2, pp. 1781-1786, 2016.

[10]   A. L. Rutz, K. E. Hyland, A. E. Jakus, W. R. Burghardt, and R. N. Shah, "A Multimaterial Bioink Method for 3D Printing Tunable, Cell‐Compatible Hydrogels," *Advanced Materials,* vol. 27, pp. 1607-1614, 2015.

[11]   C. R. Almeida, T. Serra, M. I. Oliveira, J. A. Planell, M. A. Barbosa, and M. Navarro, "Impact of 3-D printed PLA-and chitosan-based scaffolds on human monocyte/macrophage responses: unraveling the effect of 3-D structures on inflammation," *Acta biomaterialia,* vol. 10, pp. 613-622, 2014.

[12]   I.-H. Liu, S.-H. Chang, and H.-Y. Lin, "Chitosan-based hydrogel tissue scaffolds made by 3D plotting promotes osteoblast proliferation and mineralization," *Biomedical Materials,* vol. 10, p. 035004, 2015.

[13]   T. Ang, F. Sultana, D. Hutmacher, Y. S. Wong, J. Fuh, X. Mo*, et al.*, "Fabrication of 3D chitosan–hydroxyapatite scaffolds using a robotic dispensing system," *Materials science and engineering: C,* vol. 20, pp. 35-42, 2002.

[14]   L. Ouyang, C. B. Highley, C. B. Rodell, W. Sun, and J. A. Burdick, "3D printing of shear-thinning hyaluronic acid hydrogels with secondary cross-linking," *ACS Biomaterials Science & Engineering,* vol. 2, pp. 1743-1751, 2016.

[15]   C. B. Highley, C. B. Rodell, and J. A. Burdick, "Direct 3D printing of shear‐thinning hydrogels into self‐healing hydrogels," *Advanced Materials,* vol. 27, pp. 5075-5079, 2015.

[16]   L. Elviri, R. Foresti, C. Bergonzi, F. Zimetti, C. Marchi, A. Bianchera*, et al.*, "Highly defined 3D printed chitosan scaffolds featuring improved cell growth," *Biomedical Materials,* vol. 12, p. 045009, 2017.

[17]   H. Lee and G. Kim, "Cryogenically fabricated three-dimensional chitosan scaffolds with pore size-controlled structures for biomedical applications," *Carbohydrate polymers,* vol. 85, pp. 817-823, 2011.

[18]   J. A. Lewis, J. E. Smay, J. Stuecker, and J. Cesarano, "Direct ink writing of three‐dimensional ceramic structures," *Journal of the American Ceramic Society,* vol. 89, pp. 3599-3609, 2006.

[19]   S. Ghosh, S. T. Parker, X. Wang, D. L. Kaplan, and J. A. Lewis, "Direct‐Write Assembly of Microperiodic Silk Fibroin Scaffolds for Tissue Engineering Applications," *Advanced Functional Materials,* vol. 18, pp. 1883-1889, 2008.

[20]   P. Chavanne, S. Stevanovic, A. Wüthrich, O. Braissant, U. Pieles, P. Gruner*, et al.*, "3D printed chitosan/hydroxyapatite scaffolds for potential use in regenerative medicine," *Biomedical Engineering/Biomedizinische Technik,* 2013.

[21]   A. Tirella, A. Orsini, G. Vozzi, and A. Ahluwalia, "A phase diagram for microfabrication of geometrically controlled hydrogel scaffolds," *Biofabrication,* vol. 1, p. 045002, 2009.

[22]   J. Malda, J. Visser, F. P. Melchels, T. Jüngst, W. E. Hennink, W. J. Dhert*, et al.*, "25th anniversary article: engineering hydrogels for biofabrication," *Advanced Materials,* vol. 25, pp. 5011-5028, 2013.

[23]   C. A. DeForest and K. S. Anseth, "Advances in bioactive hydrogels to probe and direct cell fate," *Annual review of chemical and biomolecular engineering,* vol. 3, pp. 421-444, 2012.

[24]   F. Croisier and C. Jérôme, "Chitosan-based biomaterials for tissue engineering," *European Polymer Journal,* vol. 49, pp. 780-792, 2013.

[25]   R. S. Teotia, D. Kalita, A. K. Singh, S. K. Verma, S. S. Kadam, and J. R. Bellare, "Bifunctional polysulfone-chitosan composite hollow fiber membrane for bioartificial liver," *ACS Biomaterials Science & Engineering,* vol. 1, pp. 372-381, 2015.

[26]   M. Ahmad, S. Ahmed, B. L. Swami, and S. Ikram, "Adsorption of heavy metal ions: role of chitosan and cellulose for water treatment," *Langmuir,* vol. 79, pp. 109-155, 2015.

[27]   M. Y. Kim and J. Kim, "Chitosan Microgels Embedded with Catalase Nanozyme-Loaded Mesocellular Silica Foam for Glucose-Responsive Drug Delivery," *ACS Biomaterials Science & Engineering,* vol. 3, pp. 572-578, 2017.

[28]   S. Ladet, L. David, and A. Domard, "Multi-membrane hydrogels," *Nature,* vol. 452, pp. 76-79, 2008.

[29]   V. Latza, P. A. Guerette, D. Ding, S. Amini, A. Kumar, I. Schmidt*, et al.*, "Multi-scale thermal stability of a hard thermoplastic protein-based material," *Nature communications,* vol. 6, p. 8313, 2015.

[30]   Q. Wu, M. Maire, S. Lerouge, D. Therriault, and M. C. Heuzey, "3D Printing of Microstructured and Stretchable Chitosan Hydrogel for Guided Cell Growth," *Advanced Biosystems,* vol. 1, 2017.

[31]   S. Z. Guo, F. Gosselin, N. Guerin, A. M. Lanouette, M. C. Heuzey, and D. Therriault, "Solvent‐cast three‐dimensional printing of multifunctional microsystems," *Small,* vol. 9, pp. 4118-4122, 2013.

[32]   M. Mucha, "Rheological properties of chitosan blends with poly (ethylene oxide) and poly (vinyl alcohol) in solution," *Reactive and Functional Polymers,* vol. 38, pp. 19-25, 1998.

[33]   A. Chenite, M. Buschmann, D. Wang, C. Chaput, and N. Kandani, "Rheological characterisation of thermogelling chitosan/glycerol-phosphate solutions," *Carbohydrate polymers,* vol. 46, pp. 39-47, 2001.

[34]   J. Cho, M.-C. Heuzey, A. Bégin, and P. J. Carreau, "Physical gelation of chitosan in the presence of β-glycerophosphate: the effect of temperature," *Biomacromolecules,* vol. 6, pp. 3267-3275, 2005.

[35]   J. Bruneaux, D. Therriault, and M.-C. Heuzey, "Micro-extrusion of organic inks for direct-write assembly," *Journal of Micromechanics and Microengineering,* vol. 18, p. 115020, 2008.

[36]   S.-Z. Guo, M.-C. Heuzey, and D. Therriault, "Properties of polylactide inks for solvent-cast printing of three-dimensional freeform microstructures," *Langmuir,* vol. 30, pp. 1142-1150, 2014.

[37]   R. A. Barry, R. F. Shepherd, J. N. Hanson, R. G. Nuzzo, P. Wiltzius, and J. A. Lewis, "Direct‐Write Assembly of 3D Hydrogel Scaffolds for Guided Cell Growth," *Advanced materials,* vol. 21, pp. 2407-2410, 2009.

[38]   K. Ogawa, T. Yui, and K. Okuyama, "Three D structures of chitosan," *International Journal of Biological Macromolecules,* vol. 34, pp. 1-8, 2004.

[39]   Q. Meng, M.-C. Heuzey, and P. J. Carreau, "Hierarchical structure and physicochemical properties of plasticized chitosan," *Biomacromolecules,* vol. 15, pp. 1216-1224, 2014.

[40]   L. Li, B. Yuan, S. Liu, S. Yu, C. Xie, F. Liu*, et al.*, "Preparation of high strength chitosan fibers by using ionic liquid as spinning solution," *Journal of Materials Chemistry,* vol. 22, pp. 8585-8593, 2012.

[41]   R. Minke and J. Blackwell, "The structure of α-chitin," *Journal of molecular biology,* vol. 120, pp. 167-181, 1978.

[42]   L. J. R. Foster, S. Ho, J. Hook, M. Basuki, and H. Marçal, "Chitosan as a biomaterial: influence of degree of deacetylation on its physiochemical, material and biological properties," *PloS one,* vol. 10, p. e0135153, 2015.

[43]   H. Kweon, H. C. Ha, I. C. Um, and Y. H. Park, "Physical properties of silk fibroin/chitosan blend films," *Journal of Applied Polymer Science,* vol. 80, pp. 928-934, 2001.

[44]   X. Yang, Y. Tu, L. Li, S. Shang, and X.-m. Tao, "Well-dispersed chitosan/graphene oxide nanocomposites," *ACS applied materials & interfaces,* vol. 2, pp. 1707-1713, 2010.

[45]   J.-P. Chen, G.-Y. Chang, and J.-K. Chen, "Electrospun collagen/chitosan nanofibrous membrane as wound dressing," *Colloids and Surfaces A: Physicochemical and Engineering Aspects,* vol. 313, pp. 183-188, 2008.

[46]   A. Subramanian, D. Vu, G. F. Larsen, and H.-Y. Lin, "Preparation and evaluation of the electrospun chitosan/PEO fibers for potential applications in cartilage tissue engineering," *Journal of Biomaterials Science, Polymer Edition,* vol. 16, pp. 861-873, 2005.

CHAPTER 5   ARTICLE 2: 3D PRINTING OF MICROSTRUCTURED AND STRETCHABLE CHITOSAN HYDROGEL FOR GUIDED CELL GROWTH

Qinghua Wu, Marion Maire, Sophie Lerouge, Daniel Therriault*, and Marie-Claude Heuzey*

Published: Advanced Biosystems 1 (6), 2017, 1700058
Q. Wu, Prof. M.C. Heuzey,
Department of Chemical Engineering
Prof. D. Therriault,
Laboratory for Multiscale Mechanics (LM$_2$)
Polytechnique de Montréal
C.P. 6079, succ. Centre-Ville, Montréal (Québec),
H3C 3A7, Canada
E-mail: daniel.therriault@polymtl.ca, marie-claude.heuzey@polymtl.ca
Dr. M. Maire, Prof. S. Lerouge,
The University of Montreal Hospital Research Centre (CRCHUM)
École de technologie supérieure (ÉTS)
1100 Rue Notre-Dame O, Montréal (Québec),
H3C 1K3, Canada
KEYWORDS: 3D printing, chitosan, artificial extracellular matrix, scaffolds, cell guidance

5.1 Abstract

The ability to produce complex micro- or nanostructures from naturally derived hydrogels is significant for biomedical applications. However, precisely controlled architectures of soft hydrogels are difficult to be achieved due to their limited mechanical properties. Despite intensive research, significant challenges persist to fabricate hydrogels with ordered structures and adequate mechanical and biological properties for mimicking native tissues. In this work, a 3D printing technique is proposed to fabricate chitosan hydrogel with highly flexible and organized microfiber networks. The microstructured hydrogel scaffolds are obtained through a neutralization step. The strain at failure of hydrogel filaments can reach up to ~ 400% and maximum strength is ~ 7.5 MPa. The hydrogel scaffolds feature surface textures that can guide and align cell growth. This approach of tailoring hydrogels opens doors to design and produce 3D tissue constructs with topographical, biological, and mechanical compatibility.

5.2 Main text

Biomacromolecules, including polysaccharides and proteins, regularly form hierarchical architectures in the natural extracellular matrix (ECM) to regulate cellular behaviors (e.g., orientation, adhesion, and differentiation).[1] The precise control over the fabrication of highly ordered three-dimensional (3D) structures made of biomaterials is extremely desirable for tissue engineering and regenerative medicine.[2] Naturally derived hydrogels (e.g., chitosan, collagen, fibrin, gelatin) are appealing for biomedical application due to their similarities to natural tissues with their high affinity to cells and highly hydrated nature.[3] Simple 3D constructions (e.g., gel beads,[4] freeze-dried scaffolds,[5] and electrospun matrices[6]) have been fabricated from naturally derived hydrogels, yielding disordered structures, since their fabrication methods provided weak control of their architectures. These structures when used for guided cell growth will result in randomly distributed cells. The interactions between cells and the surface topography of biomaterials have a significant impact on cell growth.[7] Accordingly, techniques such as microfluidic spinning[8] and molecular self-assembly[9] have been proposed to fabricate ordered structures of naturally derived hydrogels. However, those structures with micro/nano-patterned surfaces have limited thickness ($< 100\,\mu m$), while cells usually require a real 3D microenvironment. In addition, the requisite mechanical properties of biomedical scaffold include stretchability, flexibility and tensile strength.[10] However, hydrogels exhibit weak mechanical properties[11] such as an alginate hydrogel with a 20% strain at failure, or a chitosan hydrogel with a ~100 kPa tensile strength,[12, 13] respectively. It remains challenging to produce the ideal 3D growth-directing structures with the adequate mechanical and biological properties in order to mimic native tissues.

3D printing methods, consisting of the precise layer-by-layer material deposition, might be able to address this challenge. Naturally derived polymers pose problems when used in 3D printing because they are too soft to support themselves as they significantly deform or collapse under their own weight.[14] Prior methods generally involving *in situ* gelling, including reservoir-induced,[15] photopolymerized[16] or temperature assisted[17] sol-to-gel transition allow hydrogels to retain their shape during the printing process. However, the conditions of *in situ* gelling, such as chemicals reacted with a pre-polymer or cross-linkers, can be cytotoxic. Herein, we report a novel and simple strategy to fabricate chitosan (natural-based polysaccharide) hydrogel featuring precise structural patterns and strong mechanical properties. The chitosan-based ink can be printed directly in air,

where it undergoes partial hardening via solvent evaporation. Subsequent refinement of chitosan scaffolds is obtained through physical gelation in a neutralization step. We demonstrated that such a 3D structural chitosan hydrogel can guide cell growth.

Figure 5.1a shows the 3D printing method. Carefully tailoring the composition and rheology of the ink has resulted in a formulation of 8% (w/v) chitosan dissolved in a mixed solvent (acetic acid/lactic acid/citric acid). The acidic solution can protonate amino groups (NH_2) in chitosan, promoting chain expansion into a semi-rigid rod conformation due to the ionic repulsion between the charged groups (NH_3^+).[18, 19] The chitosan solution was loaded in a syringe and extruded through a micronozzle under a given applied pressure, hence subjected to extensive shear flow. The chitosan ink exhibits a pronounced shear thinning behaviour (Figure S5.1a, Supporting Information), which benefits the ink flow through the deposition micronozzle at room temperature. Once the ink exits the micronozzle, the rigidity of the chitosan filament increases by solvent evaporation (Figure S5.1b, Supporting Information) and thus offers the sufficient structural support for the layer-by-layer of patterning the scaffold.[20] Dilute inks normally go through significant shrinkage upon drying and result in highly flattened filaments.[21] In our case, some residual solvent (i.e., ~45 wt.% after printing 1h, Figure S5.1b, Supporting Information) can reduce drying-induced volume shrinkage to maintain the desired lattice morphology. The chitosan filament was deposited on a three-axis, computer-controlled positioning platform in a layer-by-layer manner to generate the self-supporting 3D scaffold (Figure 5.1bi). The as-printed scaffold (10-layer) can be easily manipulated and deformed using a tweezer without breakage (Figure 5.1bii). Chitosan thick films were also printed for comparison purposes, using the same process of 10-layer stacking but without leaving gaps between filaments. After drying under vacuum for 72h, the chitosan scaffolds (Figure 5.1c) and films were immersed in a sodium hydroxide (NaOH) solution for 2h to neutralize the residual acids. The neutralized scaffolds were subsequently rinsed in water. Upon a sudden change in pH, ionized NH_3^+ groups are deprotonated into NH_2 groups, which leads to the disappearance of ionic repulsion and favours physical crosslinking (i.e., hydrophobic interactions and hydrogen bonds).[19, 22, 23] This soluble-insoluble transition allows the physical gelation of the chitosan hydrogel in the scaffold.[22, 24]
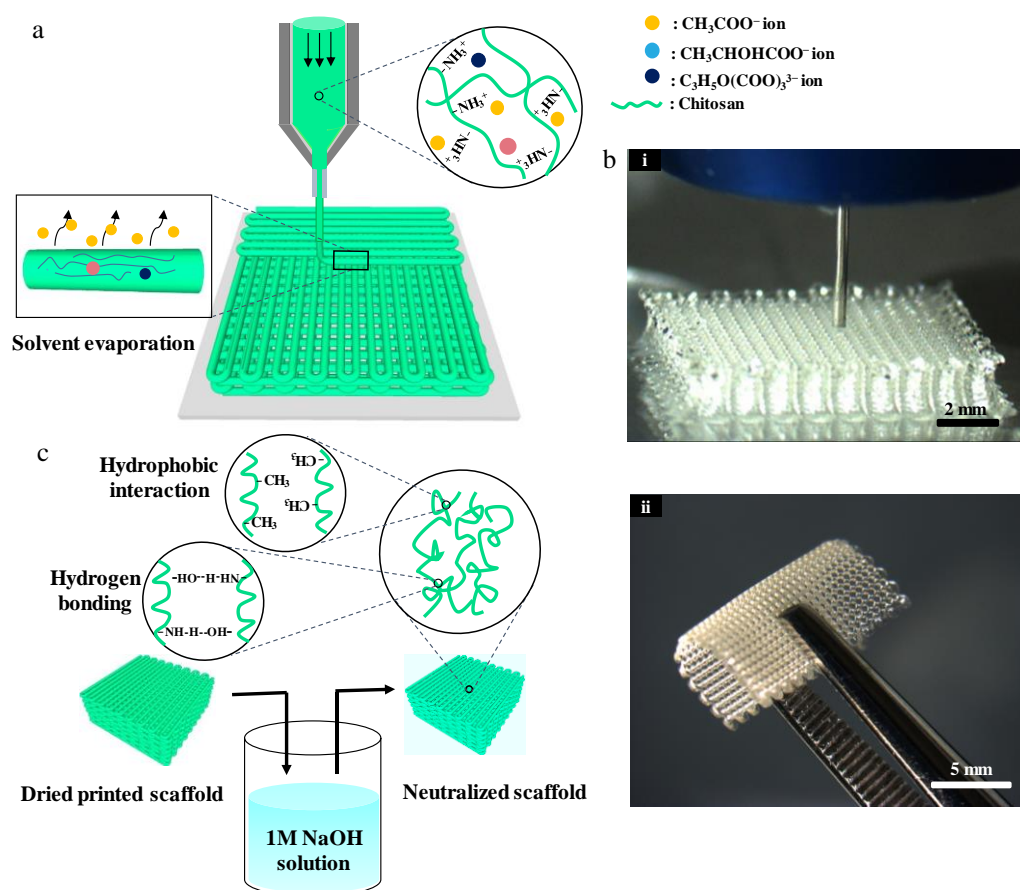
Figure 5.1: a) Schematic representation of 3D printing of a chitosan ink prepared using an acidic mixture and partially hardened via solvent evaporation. b, i) Optical image of the printing of a 30-layer 3D chitosan scaffold through a 100 µm micronozzle, and ii) optical image of a 10-layer chitosan scaffold fabricated with a 100 µm micronozzle and folded using a tweezer. c) Schematic illustration of the neutralization step for yielding physical gelation with hydrophobic interaction and hydrogen bonds to form a chitosan hydrogel scaffold.

To demonstrate the versatility of our 3D printing method, the ink was patterned into different scaffold architectures using a 100 µm micronozzle. After drying under vacuum, the diameter of chitosan filament in those scaffolds shrank to ~70% of its original value, indicating that almost 30% of the filament volume in the as-printed scaffolds was from solvent. These 30-layer (L) representative structures had a thickness (t) of ~2 mm with a total area of ~10 mm^2. Figure 5.2a-c show a dried chitosan scaffold featured with ~70 µm diameter (D) of orthogonally aligned filaments and ~220 µm pore size (Ps). The cross-section of the scaffold demonstrates the high fidelity of the printing process (Figure 5.2b), with homogeneous pores in the in-plane directions

and the circularity of the filaments (Figure 5.2c). A minimum pore size of ~ 150 µm in CS scaffold was obtained. Figure 2d-f show a dried scaffold containing inclined filaments at a minimum angle (α_{min}) of 45° and 300 µm center-to-center spacing (S) between adjacent filaments. This scaffold features layers and diamond-shaped pores. Additional images in Figure S5.2 (Supporting Information) of chitosan scaffolds fabricated with a 30 µm micronozzle show printing at higher resolution. Movie S5.1 (Supporting Information) display the printing of 3D scaffolds with square patterns. Structural features of the hydrated scaffold after neutralization (P_s = 200 µm × 200 µm, D = 100 µm, L = 10) were characterized using confocal laser scanning microscopy (CLSM). 3D reconstruction of the morphology using confocal imaging illustrates the scaffold rough surface (Figure 5.2g). Figure 2h shows a close up view of the wrinkles (microscale peaks and valleys) inherently present on the surface of the scaffold and oriented along the longitudinal direction of the filament. The wrinkling phenomenon could be attributed to the volume change[25, 26] induced by the neutralization. During the neutralization step, the scaffold filaments initially swell due to water absorption, followed by shrinkage due to intermolecular hydrogen-bonds that modify chain conformation.[22] As a comparison, the thick hydrated film (t = 1 mm, L = 10) after neutralization presented a relatively smooth surface (Figure 5.2i). This can be explained by the fact that surface wrinkling is often observed on thin structures,[26, 27] such as wrinkles on thin chitosan films (thickness of ~380 nm) after neutralization.[28]
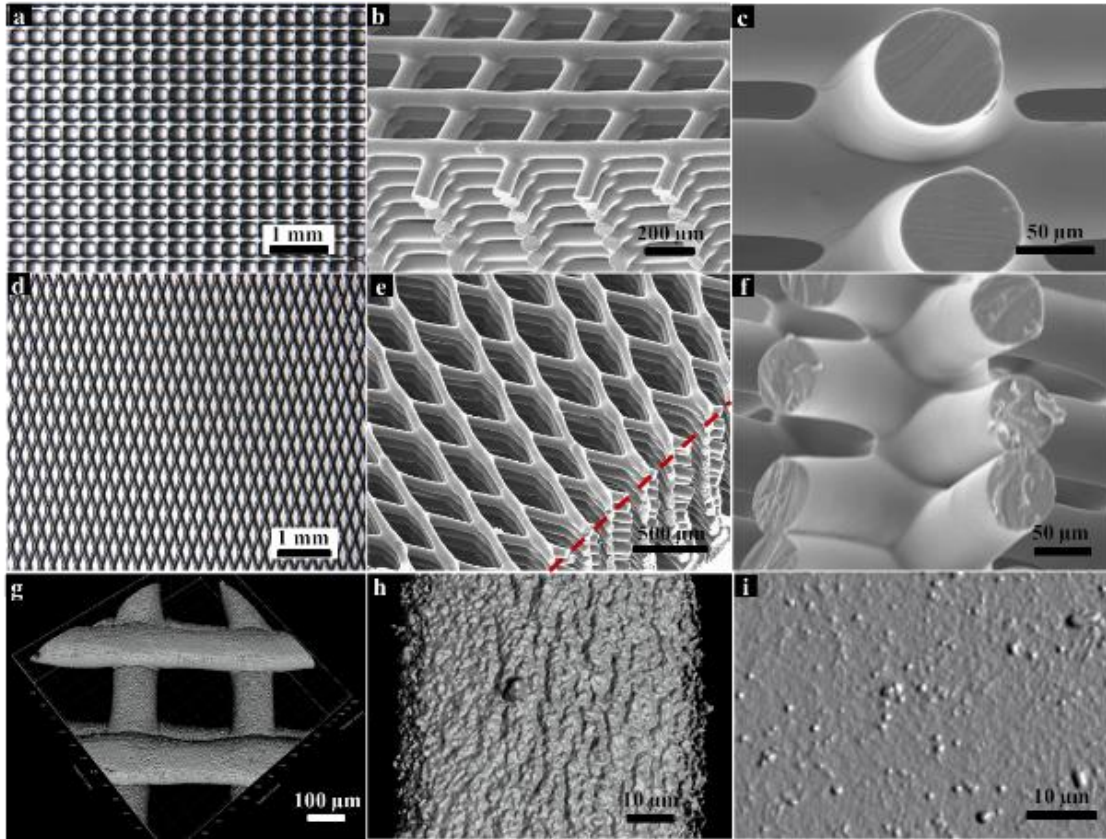
Figure 5.2: (a-f) Optical and SEM images of chitosan dried scaffolds with various architectures fabricated through a 100 µm micronozzle: (a-c) Square pattern (P_s = 220 µm × 220 µm, D = 70 µm, L = 30) and (d-f) diamond pattern (S = 300 µm, D = 70 µm, $α_{min}$ = 45°, L = 30) with top, inclined, and side views. g) 3D reconstruction of a neutralized scaffold (P_s = 200 µm × 200 µm, D = 100 µm, L = 10) in water imaged using laser scanning confocal microscopy. h) Surface rendering of the hydrated filament in a neutralized scaffold, showing a wrinkled surface using confocal fluorescence imaging after staining with Rhodamine B. i) Surface rendering of the hydrated chitosan film after neutralization (t = 1 mm, L = 10), presenting a smooth surface using confocal imaging.

Figure 5.3a shows typical stress-strain curves of as-printed chitosan filaments and neutralized filaments (in wet state). The as-printed filaments show a high strain at failure of ~180% mainly because of the residual acid solution that could maintain the elasticity under deformation.[29] The neutralized filaments present an even higher strain at failure (~400 %) and ultimate strength (~7.5 MPa) than that of the as-printed filament (~3 MPa). The tensile properties of chitosan filaments after neutralization are improved as compared to as-printed due to the formation of a complex inter-

and intra-molecular hydrogen-bond network.[19, 22, 23] To demonstrate the materials robust and flexible behavior, an as-printed chitosan scaffold (P_s = 220 μm × 220 μm, D = 90 μm, L = 10) was stretched using tweezers to almost two times its original width, held for one minute and released, upon which a rapid full recovery was observed (Figure 3b). After neutralization, the neutralized chitosan scaffold (in wet state, P_s = 200 μm × 200 μm, D = 130 μm, L = 10) is also flexible and stretchable but it requires significantly higher forces to be stretched (Figure 5.3a). The Supplementary Movie S6.2 illustrates the stretchable behaviour of both scaffolds. Our ink design and fabrication method lead to superior stretchability, strength and flexibility of the obtained hydrogel as compared to reported behavior of chitosan-based constructions fabricated using more traditional techniques.[30]
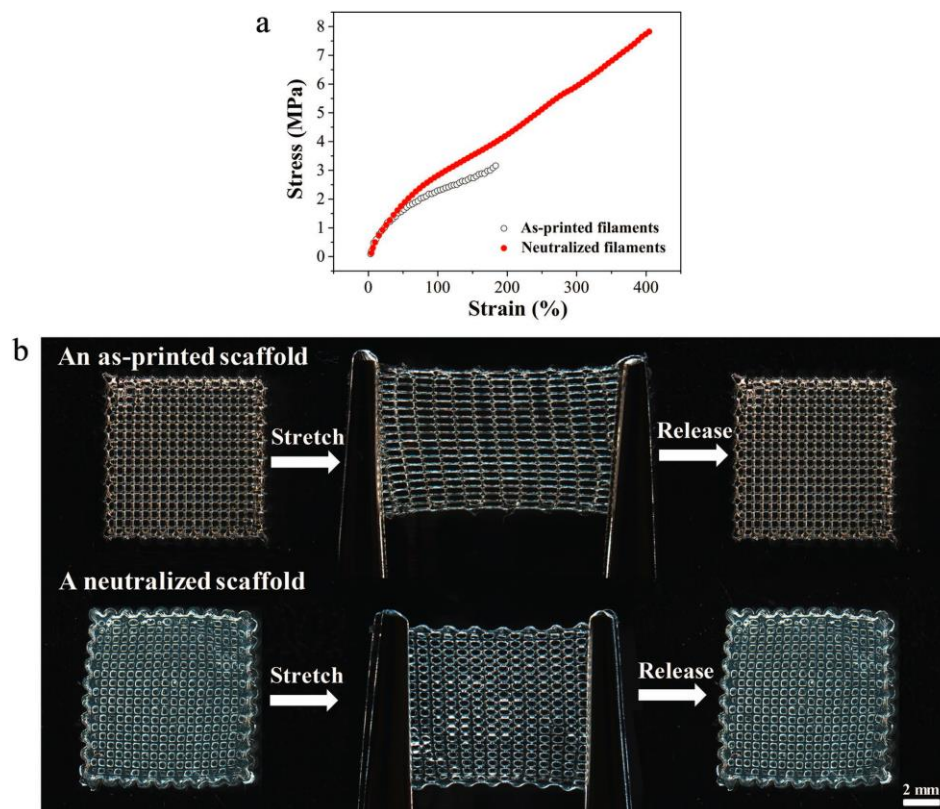
Figure 5.3: a) Typical stress-strain curve for as-printed chitosan (surface area = 0.15 mm^2) and neutralized chitosan filaments (surface area = 0.22 mm^2) in wet state. b) An as-printed chitosan scaffold (P_s = 220 μm × 220 μm, D = 90 μm, L = 10) and a neutralized chitosan scaffold (P_s = 200 μm × 200 μm, D = 130 μm, L = 10) are uniaxially stretched to almost two times its initial width and experiences full recovery after stretching to return to its original shape.

As a first assessment of biocompatibility, L929 fibroblasts were cultivated in extracts of neutralized chitosan films (t = 1 mm, L = 10) and scaffolds (P_s = 200 μm × 200 μm, D = 100 μm, t = 1 mm, L = 10) for indirect cytotoxicity tests. Excellent cell survival (around 100%, Figure S5.3, Supporting Information) was observed in hydrogel scaffold and film extracts. Furthermore, hydrated chitosan films and scaffolds after neutralization were evaluated for their ability to support cell adhesion, spreading and proliferation over one week through the culture of fibroblasts. Figure 5.4a shows the Live-Dead staining results after 7 days of cell culture. The image shows that live cells (in green) fully cover the chitosan scaffolds, with only very few or no dead cells (in red). Scanning electron microscopy (SEM) imaging of fibroblasts adhered on the scaffolds shows that they generally display flattened elongated morphology (Figure 5.4b). Alamar Blue measurements after 1, 3 and 7 days demonstrated excellent cell growth on both 3D scaffolds and films, as shown by fluorescence values increasing 25- and 36-fold from day 1 to 7, respectively (Figure 5.4c). Figure 5.4d and e illustrate that L929 fibroblasts cultivated on the scaffold mostly orient along the printed direction of chitosan filaments. By contrast, cells plated on chitosan films show a random distribution in response to the relatively smooth surface of the films (Figure 5.4g and h). The alignment of the cultured cells was quantified from SEM images by defining the alignment angle θ between the fibroblasts and the direction of the patterned filaments in scaffolds, or an reference line in films (Figure 5.4f). Approximatively 400 cells were analysed to plot the curves of Figure 5.4i. More than 90% of the cells were oriented almost parallel to each of the orthogonal directions ($\theta = 0 \pm 30°$) in the scaffolds, whereas the alignment angle distribution on the chitosan films was wide, demonstrating mostly random cellular alignment. These images and angle distributions indicate that the wrinkles on the surface and/or the architecture of the scaffold itself act as topographical cues that can induce fibroblasts alignment.
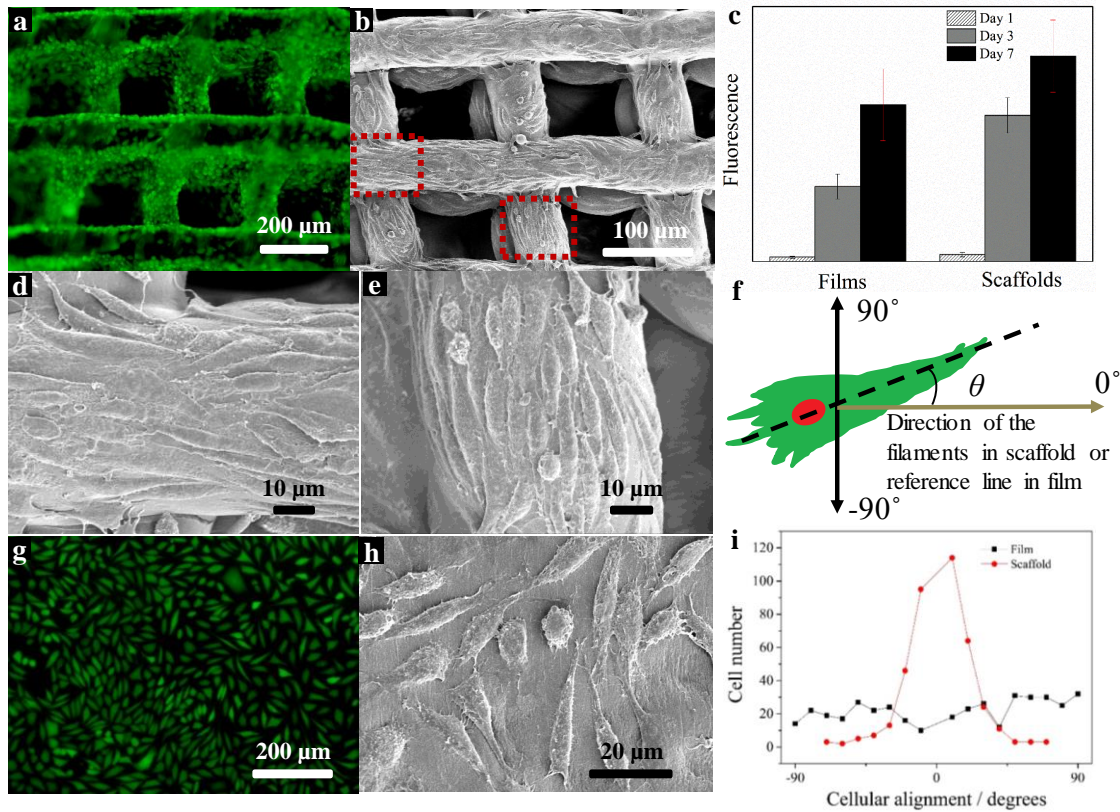
Figure 5.4: a) Fluorescence images of L929 fibroblasts plated on neutralized chitosan scaffolds (P_s = 200 μm × 200 μm, D = 100 μm, L = 10) after 7 days. b) SEM image of L929 fibroblasts adhered on neutralized chitosan scaffolds after 7 days. c) Cell viability on surface of scaffolds and films (t = 1 mm, L = 10) by Alamar Blue assay at 1, 3 and 7 days. d) and e) SEM images of L929 fibroblasts plated on chitosan scaffolds under a higher magnification view of figure b) in the red frame areas. f) Schematic diagram illustrating the procedure used to characterize the alignment angle θ between the orientation of fibroblasts and the main direction of filaments in scaffolds or horizontal line in films. g and h) Fluorescence and SEM images of L929 fibroblasts plated on chitosan films after 7 days. i) Quantification of the orientation of fibroblasts on hydrated chitosan scaffolds and films.

Our current work presents topographically, mechanically and biologically tailored 3D scaffolds from a chitosan hydrogel via a novel 3D printing strategy. The high flexibility of the printed materials with precise porous architectures opens doors to impart topographical complexity with high resolution into soft natural materials. To the best of our knowledge, this is the first report of programmable periodical patterns with wrinkled surface in naturally derived hydrogel used to guide

and orient cell growth. Further study of the mechanisms of the wrinkle formation and its impact on cells growth is underway, along with monitoring mechanical properties of chitosan scaffolds as functions of time during biodegradation. Looking forward, this approach may be leveraged to generate complex topologies for different soft materials, with tunable mechanical and biological properties for tissue or organ repair.

5.3 Experimental Section

Ink Preparation: The chitosan inks were prepared by dissolving 8% (w/v) chitosan (90% deacetylated, weight average molecular weight = 207 kDa, from Biolog in Germany) in solutions (acidic mixture: 40 vol% acetic acid, 10 vol% lactic acid and 3 wt.% citric acid). The acids were all purchased from Sigma-Aldrich and used as received. After resting for 12 h, the solutions were mechanically stirred for 2 h (150 rpm) and centrifuged at 3000 rpm for 1 h to remove air bubbles.

3D Printing of Chitosan Hydrogel Scaffolds and Films: 3D printing was performed using a deposition system consisting of a computer controlled robot (I&J2200-4, I&J Fisnar) with a 3-axis positioning stage and a dispensing apparatus (HP-7X, Nordson EFD). The inks were loaded into a syringe (3 mL, Nordson EFD) mounted in the dispensing adaptor and extruded through a nozzle of 100 µm (5132-0.25-B, Nordson EFD) under applied pressures of ~2 MPa with a velocity of 0.5 mm s^{-1}. Chitosan thick films (~1 mm) were fabricated from orthogonally aligned filaments without pore space. After printing, the scaffolds and films were dried under vacuum at 50 °C for 24 h, neutralized in a 1M NaOH solution for 2 h and rinsed in distilled water to remove residual acids.

Morphological characterization: Chitosan scaffolds were observed with an optical microscope (BX-61, Olympus) and a SEM (JSM-840A, JEOL). For the 3D surface analysis, neutralized chitosan films and scaffolds were stained using Rhodamine B for 30 min, and then imaged with a CLSM Nikon C2. Rhodamine B stained samples were observed under a 561 nm laser (Em 561LP). Surface rendering was applied on a 1 µm to 15 µm spacing z-stacks by using Imaris 8.2 analysis software (BitPlane, Switzerland).

Tensile properties of Chitosan Filaments: Chitosan filaments were produced by 3D printing. They were treated with different processes (neutralization and subsequent washing, or non-neutralization). Filaments were tested using an electromechanical machine (Insight MTS 50KN)

with a 100 N load cell. The tests were repeated seven times using the standard of ASTM D3822 / D3822M.

Cell Culture and Imaging: L929 fibroblasts (15000 per circular sample, placed in 48-well culture plates) were seeded on scaffolds and films. After 4h of adhesion, samples were rinsed with PBS and cells were left to grow in 500 µl of CM for an additional 20h, 3 days and 7 days. Cellular activity was evaluated with Alamar Blue, after transferring the samples to a new well plate to avoid signal from cells that had possibly adhered to the bottom of the wells during culture. The same samples were used for Live/Dead assay (2 µM calcein and 5.5 µM ethidium homodimer diluted in serum free DMEM F12, 45 min incubation at 37 °C). After 7 days of culture other samples were fixed, dehydrated and gold coated for observation by SEM (JSM-840A, JEOL).

5.4 Acknowledgements

5.5 Supporting information

Ink characterization

Ink Rheology: A rotational rheometer (MCR-502, Anton Paar) fitted with a cone and plate flow geometry was used to characterize the chitosan inks (prepared using the acidic mixture). Shear viscosity measurements were conducted at shear rates of 0.1 to 100 s^{-1} at room temperature and under ambient pressure. Mineral oil covered the edge of the sample in the cone and plate flow geometry to prevent solvent evaporation and was shown not to affect the measurements. Process-related viscosity of the inks was also measured by capillary flow analysis[1, 2]. Chitosan solutions (8w/v%) housed in a syringe barrel (3mL, Nordson EFD) were extruded through a micronozzle (inner diameter $D = 200$ µm, capillary length $l = 12.25$ mm, Nordson EFD) under different applied pressures ranging from 530 kPa to 2000 kPa (HP-7X, Nordson EFD) at a velocity of 0.5 mm s^{-1}. Patterned microfibers (60 mm) were dried in vacuum at 50 °C for 24 h and weighed by a high-

precision balance (GH-202, A&D Engineering Inc.) to calculate the apparent viscosity using the method by Bruneaux *et.al* [1]

Determination of Solvent Evaporation Rate: The solvent evaporation of chitosan inks (mixture: 40 vol% acetic acid solution, 10 vol% lactic acid, 3wt.% citric acid) was analyzed for process optimization purposes. Once chitosan filaments (50 mm) were deposited on a glass substrate for 5 s through a micronozzle (D =250 µm, Nordson EFD) under an applied pressure of 1.3 MPa, the weight change was monitored with a high-precision balance (GH-202, A&D Engineering) at room temperature. The weight reduction of samples was recorded for 6 h, and subsequently the samples were weighed again after complete drying under vacuum at 55 ℃ for 72h. The solvent percentage was calculated by the weight change between the as-printed filaments and dried filaments.

3D Printing of Chitosan scaffolds

The chitosan inks were loaded into a syringe (3 mL, Nordson EFD) mounted in the dispensing adaptor and extruded through a nozzle of 30 µm (World Precision Instruments) under applied pressures of 0.4-1 MPa with linear velocities of 0.5-2 mm s^{-1}. The scaffolds were defined by geometry, spacing between filaments, and number of layers. They were produced with orthogonally or obliquely aligned filaments, with 160-360 µm homogenous or gradient spacing over 1 cm^2 area with 12-20 layers.

Indirect Cytotoxicity Tests

L929 (mouse fibroblasts, ATCC, USA) were cultured in CM composed of DMEM F12 (Dulbecco's modified Eagle Medium/Nutrient Mixture F-12 Ham'sMedium, Gibco, Invitrogen, USA) containing 10% foetal bovine serum (FBS). Indirect cytotoxicity tests on gel extracts were performed following the ISO 10993-5: 2009 standard. Hydrogel extracts were obtained by immersing samples in CM containing 1% penicillin – streptomycin. Every 24 h, the supernatant was collected and replaced with fresh medium. Cells were grown until 80-90% of confluency and exposed to gel extracts for 24 h before evaluating cell viability by Alamar Blue assay (resazurin, Cedarlane Corp, Canada, 10% v/v in CM). After 4 h incubation at 37 °C, 5% CO2, the supernatant was collected and placed in a 96 well plate in triplicate. The plate was read with a spectrophotometer ($\lambda_{excitation}$ = 560 nm and $\lambda_{emission}$ = 590 nm, BioTek Instruments Inc., Synergy 4, USA). Cells in culture media without extract and with DMSO 10% were used positive and negative controls.
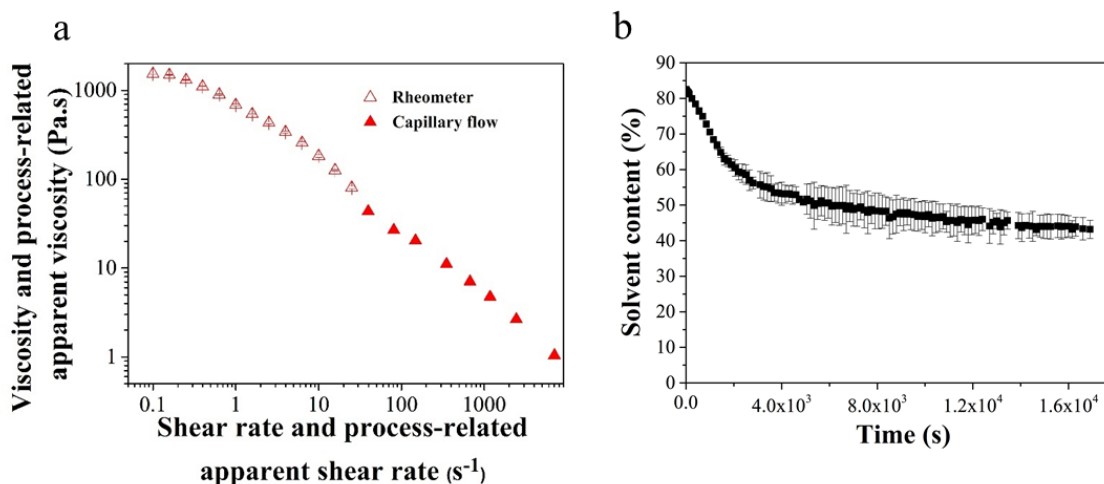
Figure S5.1: Ink characterization. a) Viscosity of the 8% (w/v) chitosan solution prepared using the acidic mixture as a function of shear rate (open symbols: data obtained using a rheometer with a cone and plate flow geometry; solid symbols: data obtained by extrusion of the chitosan solution with a 200 μm nozzle in capillary flow analysis[31]). b) Solvent evaporation rate as a function of time for the chitosan ink using the following printing parameters of an applied pressure = 1.3 MPa, robot velocity = 0.5 mm/s.
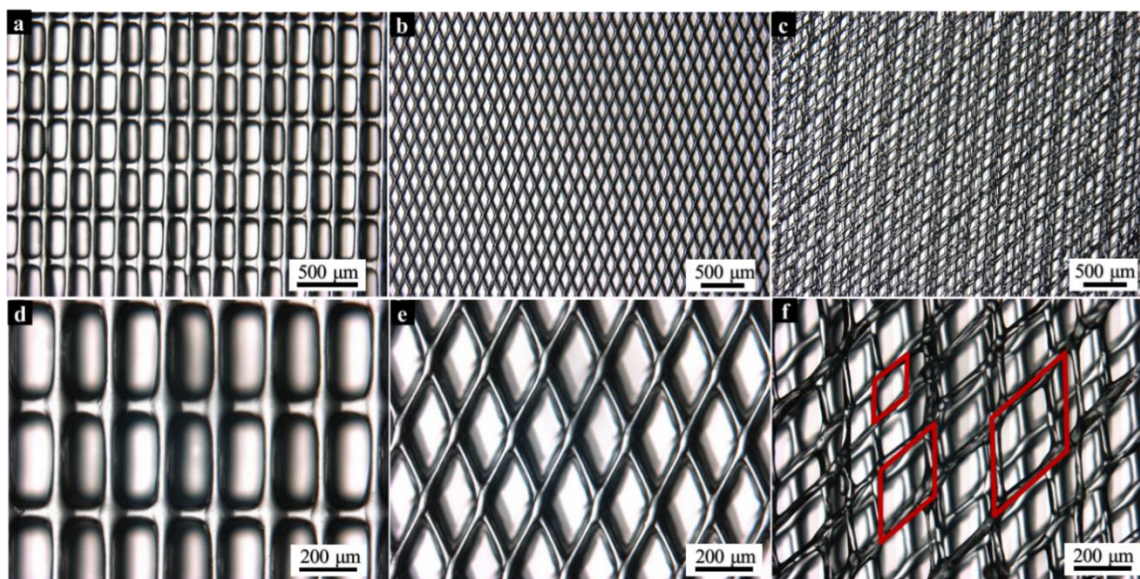
Figure S5.2: Optical images of chitosan hydrogel scaffolds with different patterns produced through a 30 μm micronozzle. a) Rectangular pattern (P_s=160 μm×360 μm, D=45 μm, 20 L), b) Diamond pattern (Ls=270 μm, D=30 μm, 10 L, Ma=45°), c) Diamond pattern with gradient pores (Ls=270 μm, 410 μm, 530 μm, D=30 μm, 12 L, Ma=45°). d-f) Higher-magnification view

of scaffolds corresponding to a, b, c. (P_s=pore size, D=fiber diameter, L=layers, Ma=Minimum angle, Ls=side length).

Movie S5.1: 3D printing of 30-layer chitosan hydrogel scaffolds using a 100 µm nozzle and a 30 µm nozzle at a velocity of 0.5 mm s^{-1}.

Movie S5.2: An as-printed chitosan and a neutralized scaffold stretched by tweezers.
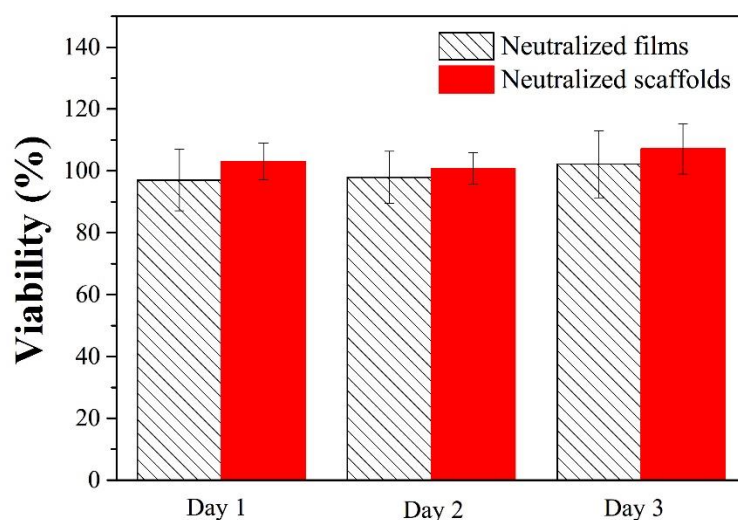
Figure S5.3: Results on the toxicity of extracts from neutralized chitosan films and scaffolds. L929 fibroblasts show around 100% cell viability in the extract medium of chitosan films and scaffolds after immersion 1, 2 and 3 days.

References

[1]   a) C. M. Nelson, M. M. VanDuijn, J. L. Inman, D. A. Fletcher, M. J. Bissell, Science **2006**, 314, 298; b) J. K. Mouw, G. Ou, V. M. Weaver, Nature Reviews Molecular Cell Biology **2014**, 15, 771; c) A. C. Neville, *Biology of fibrous composites: development beyond the cell membrane*, Cambridge University Press, **1993**, p. 117-121.

[2]   a) H. Shin, S. Jo, A. G. Mikos, Biomaterials **2003**, 24, 4353; b) N. Geisel, J. Clasohm, X. Shi, L. Lamboni, J. Yang, K. Mattern, G. Yang, K. H. Schäfer, M. Saumer, Small **2016**, 12, 5407; c) J. A. Inzana, D. Olvera, S. M. Fuller, J. P. Kelly, O. A. Graeve, E. M. Schwarz, S. L. Kates, H. A. Awad, Biomaterials **2014**, 35, 4026.

[3]   a) J. Malda, J. Visser, F. P. Melchels, T. Jüngst, W. E. Hennink, W. J. Dhert, J. Groll, D. W. Hutmacher, Advanced Materials **2013**, 25, 5011; b) J. M. Silva, R. L. Reis, J. F. Mano, Small **2016**.

[4]   C. Fan, D.-A. Wang, RSC Advances **2015**, 5, 80688.

[5]   B. Trappmann, J. E. Gautrot, J. T. Connelly, D. G. Strange, Y. Li, M. L. Oyen, M. A. C. Stuart, H. Boehm, B. Li, V. Vogel, Nature materials **2012**, 11, 642.

[6]   a) J. Visser, F. P. Melchels, J. E. Jeon, E. M. van Bussel, L. S. Kimpton, H. M. Byrne, W. J. Dhert, P. D. Dalton, D. W. Hutmacher, J. Malda, Nature communications **2015**, 6. b) S. N. Jayasinghe, Analyst 2013, 138, 2215.

[7]   D. Hoffman-Kim, J. A. Mitchel, R. V. Bellamkonda, Annual review of biomedical engineering **2010**, 12, 203.

[8]   E. Kang, Y. Y. Choi, S. K. Chae, J. H. Moon, J. Y. Chang, S. H. Lee, Advanced Materials **2012**, 24, 4271.

[9]   S. Zhang, M. A. Greenfield, A. Mata, L. C. Palmer, R. Bitton, J. R. Mantei, C. Aparicio, M. O. de La Cruz, S. I. Stupp, Nature materials **2010**, 9, 594.

[10]   S. Agarwal, J. H. Wendorff, A. Greiner, Advanced Materials **2009**, 21, 3343.

[11]   a) F. Croisier, C. Jérôme, European Polymer Journal **2013**, 49, 780; b) M. G. A. Vieira, M. A. da Silva, L. O. dos Santos, M. M. Beppu, European Polymer Journal **2011**, 47, 254; c) S. J. Hollister, Nature materials **2005**, 4, 518.

[12]   H. Lee, G. Kim, Carbohydrate polymers **2011**, 85, 817.

[13]   J.-Y. Sun, X. Zhao, W. R. Illeperuma, O. Chaudhuri, K. H. Oh, D. J. Mooney, J. J. Vlassak, Z. Suo, Nature **2012**, 489, 133.

[14]   T. J. Hinton, Q. Jallerat, R. N. Palchesko, J. H. Park, M. S. Grodzicki, H.-J. Shue, M. H. Ramadan, A. R. Hudson, A. W. Feinberg, Science advances **2015**, 1, e1500758.

[15]   L. Geng, W. Feng, D. W. Hutmacher, Y. San Wong, H. Tong Loh, J. Y. Fuh, Rapid Prototyping Journal **2005**, 11, 90.

[16]   T. Billiet, E. Gevaert, T. De Schryver, M. Cornelissen, P. Dubruel, Biomaterials **2014**, 35, 49.

[17]   A. L. Rutz, K. E. Hyland, A. E. Jakus, W. R. Burghardt, R. N. Shah, Advanced Materials **2015**, 27, 1607.

[18]   a) M. Rinaudo, G. Pavlov, J. Desbrieres, Polymer **1999**, 40, 7029; b) S. Dumitriu, Polymeric biomaterials **2001**, 1.

[19]   S.-B. Park, J.-O. You, H.-Y. Park, S. J. Haam, W.-S. Kim, Biomaterials **2001**, 22, 323.

[20]   S. Z. Guo, F. Gosselin, N. Guerin, A. M. Lanouette, M. C. Heuzey, D. Therriault, Small **2013**, 9, 4118.

[21]   a) J. A. Lewis, J. E. Smay, J. Stuecker, J. Cesarano, Journal of the American Ceramic Society **2006**, 89, 3599; b) A. Bhatti, M. Mott, J. Evans, M. Edirisinghe, Journal of materials science letters **2001**, 20, 1245.

[22]   S. Ladet, L. David, A. Domard, Nature **2008**, 452, 76.

[23]   J. Berger, M. Reist, J. M. Mayer, O. Felt, R. Gurny, European Journal of Pharmaceutics and Biopharmaceutics **2004**, 57, 35.

[24]   E. Kokufuta, Langmuir **2005**, 21, 10004.

[25]   E. S. Matsuo, T. Tanaka, **1992**.

[26]   B. Li, Y.-P. Cao, X.-Q. Feng, H. Gao, Soft Matter **2012**, 8, 5728.

[27]   L. Ionov, Journal of Materials Chemistry **2012**, 22, 19366.

[28]   K. Gulati, L. Johnson, R. Karunagaran, D. Findlay, D. Losic, Biomacromolecules **2016**, 17, 1261.

[29]   P. S. Garcia, M. V. E. Grossmann, M. A. Shirai, M. M. Lazaretti, F. Yamashita, C. M. O. Muller, S. Mali, Industrial Crops and Products **2014**, 52, 305.

[30]   a) Y. Huang, S. Onyeri, M. Siewe, A. Moshfeghian, S. V. Madihally, Biomaterials **2005**, 26, 7616; b) L. Li, B. Yuan, S. Liu, S. Yu, C. Xie, F. Liu, X. Guo, L. Pei, B. Zhang, Journal of Materials Chemistry **2012**, 22, 8585; c) S. Sayyar, E. Murray, B. Thompson, J. Chung, D. L. Officer, S. Gambhir, G. M. Spinks, G. G. Wallace, Journal of Materials Chemistry B **2015**, 3, 481.

CHAPTER 6   ARTICLE 3: 3D PRINTING OF SELF-HEALING AND STRETCHABLE NANOCOMPOSITES SENSORS

Qinghua Wu[†], Shibo Zou[§], Frédérick Gosselin[§], Daniel Therriault[§], Marie-Claude Heuzey[†]

Submitted: Materials Horizons, 2018

[†]Department of Chemical Engineering, Research Center for High Performance Polymer and Composite Systems (CREPEC), Polytechnique Montréal, Canada

[§]Laboratory for Multiscale Mechanics (LM2), Department of Mechanical Engineering, Research Center for High Performance Polymer and Composite Systems (CREPEC), Polytechnique Montréal, Canada

6.1 Abstract

The design of self-healable and stretchable devices from sustainable materials is increasingly attractive for various applications such as soft robotics, wearable sensors, and biomedical devices. In this work, we report a novel multifunctional material with self-healing ability and electrical conductivity based on chitosan (CS) and multiwall carbon nanotubes (CNT) (30 wt %). The self-healing of the nanocomposites can be achieved with the assistance of water vapor. The self-healing process is rapid, occurring within seconds to heal the damage. Upon drying, the conductivity can be restored. The nanocomposite is processed by instability-assisted 3D printing at room temperature for producing highly tunable microstructured fibers. The microstructured fibers featuring sacrificial bonds and hidden lengths endow the nanocomposite with high stretchability (strain at break of 180%). Exposure the CS/CNT microstructured fibers to water vapor can restore their mechanical properties (e.g., flexibility, strength and toughness) after healing their broken sacrificial bonds. Granted with properties such as self-healing, stretchability and conductivity, CS/CNT nanocomposite strain sensor are developed to detect human elbow motion and local deformation. This work opens new doors for incorporating self-healing ability and high stretchability into sensor design, as well as highlighting the utilization of a biodegradable polymer that leads to a class of electronic materials for excellent performance and functionality of electronic devices.

6.2 Main text

Electronic waste containing toxic or non-biodegradable materials is a serious issue due to growing demand for newer and more powerful electronics.[1, 2] Natural polymers are excellent candidates for developing next-generation of sustainable electronics owing to their lightweight, low-cost, non-toxic, biodegradable and renewable properties.[3, 4] Self-healing is a very desirable feature to engineer electronic materials for various applications such as portable and wearable sensors,[5, 6] electronics,[7] and soft robotics,[8] due to its ability to heal the damaged sites and restore the material shape and properties. Recent researches on the design of self-healing materials based on autonomic healing (e.g., polymeric materials with noncovalent bonds[9, 10]), or nonautonomic systems (e.g., epoxy polymers[11] and supramolecular polymers[12]) via an external stimuli (e.g., temperature,[13] or light[14]) have been successfully employed to restore mechanical properties after material damage. However, lack of electrical conductivity limits their applications in electronics. White *et al.* provided the first example of healing electrodes using solvent-filled microcapsules from a conductive silver ink to heal damage, allowing excellent restoration of conductivity.[15] Guo *et al.* reported a self-healing nanocomposite of poly(2-hydroxyethyl methacrylate) and single-walled carbon nanotubes (10 wt %) through host-guest-interactions with a conductivity of 7.76 S/m.[16] Water-healable conducting polyethylenedioxythiophene films,[17] conductive coatings on a self-healing film,[18] or electrical wire embedded in self-healing sandwich architecture[19] have also been reported. However, most of these materials involved complicate preparation methods or their fabrication methods were difficult to fabricate complex structures for electronic applications. Most stretchable electronic devices are produced by tailoring the material structures such as serpentine stripes and wavy patterns[20, 21], elastomer-based stretchable textiles,[22] or using intrinsic materials stretchability (e.g., stretchable polyelectrolyte).[23] However, they require complex microfabrication technologies or exhibit low conductivity (e.g., up to 0.75 S/m). It remains a challenge to combine eco-friendly material, easy processing, fast and repeatable healing properties, high stretchability and complex structures into material design for electronic applications.

3D printing has drawn important attention for the fabrication of electronic devices due to its low-cost, reliability and ability to accurately fabricate complex 3D structures. [24] Conductive polymer-based nanocomposites (CPN) can be used as strain-sensing materials owning to their conductivity, lightweight, easy processability and corrosion resistance.[25] High loading of carbon nanotubes

(CNT) (e.g., 20 wt %) is necessary to obtain a highly conductive nanocomposite.[26] However, high CNT concentration into the polymer binder enhances the stiffness of the resulting nanocomposite but reduces its stretchability, with limited elastic strain range ($\leq$ 15%).[27-29] Passieux *et al.* reported instability-assisted 3D printing (IA3DP) of poly(lactic acid) (PLA) fibers with sacrificial bond to improve polymer stretchability.[30] Incorporation of structural design into the nanocomposite materials (e.g., featuring sacrificial bond and hidden length to improve the stretchability) might address the challenge of obtaining high conductivity and stretchability in CPN. Although several CPN inks have been developed so far,[31-34] these inks usually contain toxic organic solvents (e.g., dichloromethane) and/or toxic components (e.g., sodium dodecyl sulfate surfactant).

Here, we report a self-healing chitosan (CS)/carbon nanotubes (CNT) nanocomposite that is able to heal damage under exposure to water vapor at room temperature. The nanocomposite can be fabricated with microstructured fibers featuring sacrificial bond and hidden length by instability-assisted 3D printing (IA3DP). The resultant as-printed CS/CNT structure retains its hierarchical architecture and exhibits excellent mechanical properties. A conductivity as high as ~ 1450 S/m was measured, which is higher than previously reported chitosan-based CNT nanocomposites (e.g., ~ 500 S/m).[35-37] The microstructure of completely or partially broken CS/CNT fibers (e.g., cut straight fibers or broken sacrificial bonds in microstructured fibers) can be restored, as well as their electrical and mechanical properties after exposing to water vapor. This water-vapor triggered nanocomposite allows processing multidimensional architectures and develop functional sensors that are capable of sensing humidity and strain.

Figure 6.1 shows the overall development of the novel CS/CNT ink to produce complex 3D structures and microstructured fibers by a solvent-cast 3D printing (SC3DP) and instability-assisted 3D printing (IA3DP).[30, 38] The inks consisted of a blend of CS as polymer binder, CNTs, and dispersing solution (i.e., a mixture of acetic acid, lactic acid, citric acid and distilled water) (Figure 6.1a). In addition to all being protonating agents of NH_2 groups in chitosan, these acids also play specific roles. For example, lactic acid is a plasticizer[39] while citric acid (CA, 5 wt %, non-volatile) facilitates electrostatic interaction between negatively charged citrate ions (CA^-) with positively charged amino groups (NH_3^+) on chitosan chains (CS^+).[38] An ink with well-dispersed nanoparticles in the polymer matrix is critical for ensuring smooth flow through fine nozzles and avoiding clogging during the printing process. CS/CNT nanocomposites with high CNT concentration (i.e., up to 40 wt % based on the total weight of CS + CNT) were prepared using a ball mixing method.[33]

The conductivity of CS/CNT fibers with different CNT contents (i.e., 5, 10, 20, 30 and 40 wt %) inks is shown in Figure 6.1b. The conductivity of the fibers increased significantly with CNT concentration up to 30 wt %, and then increased slightly from ~1240 S/m (30 wt % CNT) to ~1450 S/m (40 wt % CNT). This high conductive performance was attributed to percolation pathways that were formed from CNTs interconnected in the matrix of CS but increasing the filler concentration (CNT > 30 wt %) had limited effect on the increase in conductivity of the nanocomposite since many percolation pathways were already formed. Figure S6.1 (Supporting Information) shows well dispersed CNTs in the CS/CNT nanocomposite (30 wt % CNT). CS/CNT inks (CNT ≤ 30 wt %) were 3D printable and allowed the generation of 3D complex structures. A 20-layer scaffold (30 wt % CNT), starfish- and spider-shape-like (10 wt % CNT) 3D structures as shown in Figure 6.1c were fabricated by SC3DP in a layer-by-layer manner, with solvent evaporation to solidify the CS/CNT structures. Microstructred CS/CNT fibers can also be produced by instability-assisted 3D printing (IA3DP) in ambient air. The instability occurs by locating the robot head slightly above a computer-controlled platform and adjusting the speed ratios between the material flow rate and the platform (schematic in Figure 6.1d). A CS/CNT ink loaded in a syringe was extruded at a material speed V_t through a micronozzle located at a distance H above the platform which moves at a robot speed V_p. By simply tailoring the speed ratio V_t/V_p, different periodic patterns can be obtained (i.e., straight, meandering, coiling, alternating and overlapping fibers), as shown in Figure 6.1d. The different speed ratios corresponding to different patterns is shown in Table S6.1 (Supporting Information). Movie S6.1 (Supporting Information) shows the fabrication of microstructured fibers by IA3DP under different speed ratios. These microstructured fibers have different contour lengths L, wavelengths λ and diameters D. The nanocomposite with 30 wt % CNT was mainly investigated due to its high conductivity and facile printability. The versatility of our fabrication method and ink design exhibited high flexibility in producing various CS/CNT structures (e.g., 3D scaffold and spider-like 3D structure in Figure 1c and microstructured fibers in Figure 6.1d).
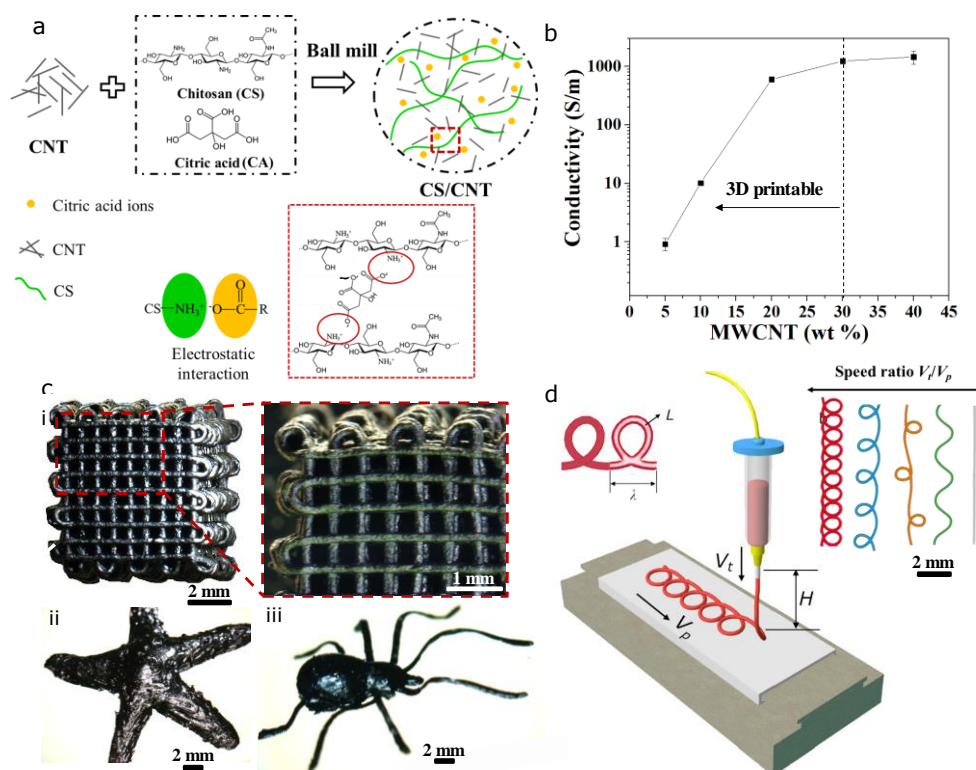
Figure 6.1: (a) CS/CNT ink preparation: CS polymer dilute solution (solvent: acetic acid, citric acid and lactic acid) and CNT were mixed via a ball mixing method. (b) Electrical conductivity of CS/CNT nanocomposites with different CNT contents. The zone at the left of the vertical dashed line represents 3D printable CS/CNT inks with CNT content lower than 30 wt %. (c) A 20-layer scaffold, spider and starfish shaped structures fabricated by the 3D printing method, which undergo solvent evaporation to solidify the structures. (d) Schematic of instability-assisted 3D printing (IA3DP): a CS/CNT fiber with fiber diameter D and contour length L was fabricated with a depositing height H, robot speed V_p and material speed V_t. Photographs of different patterned CS/CNT fibers fabricated from IA3DP under the same condition of $H/D = 10$, from right to left: straight, meandering, alternating, coiling and overlapping patterns.

The healing behavior and corresponding electrical conductivity of CS/CNT nanocomposites are shown in Figure 6.2. A 30 wt % CS/CNT fiber was cut into two halves and then was healed under exposure to water vapor for only ~10 s (Figure 6.2a). Optical microscopy images of the damaged fiber before (with a ~50 µm gap) and after the healing demonstrate the ability of water vapor to enable the healing of the conductive nanocomposite. The schematic of self-healing mechanism is shown in Figure 6.2b. Under water vapor, the CS/CNT fiber swells due to the polymer water-

uptake. The CS swelling enhanced the polymer chains movement and the electrostatic interactions between citrate ions CA^- in the dispersing fluid and NH_3^+ on CS chains, which most probably contributed to the healing effect and leaded to an increase of fiber softness. Figure 6.2c shows the current of the fiber recovered after healing five successive cuts on the fiber. The nanocomposite fiber was healed after exposure to water vapor for ~ 10 s. The electrical current in the fiber was restored to its original value upon drying to evaporate the adsorbed water in the fiber. This result indicates a repeatable restoration of electrical conductivity in the CS/CNT nanocomposite.
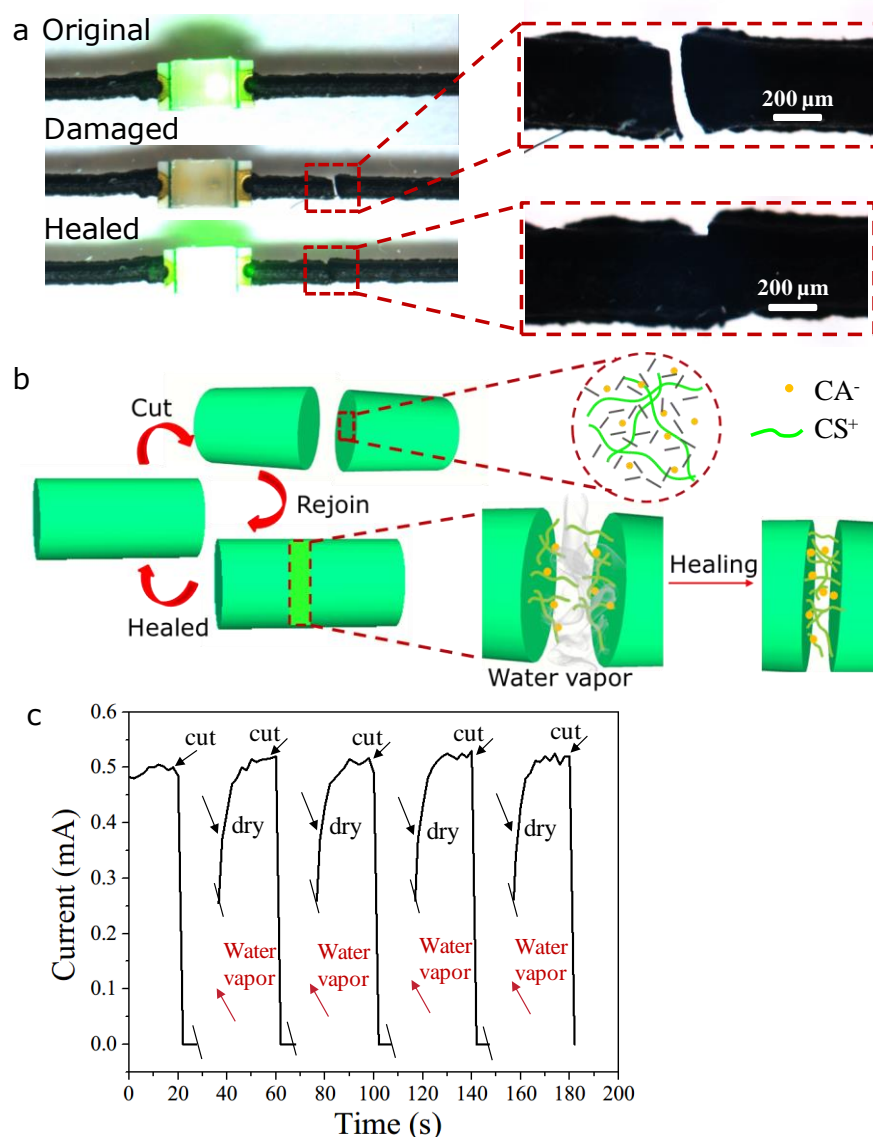
Figure 6.2: (a) Optical microscopy images of a CS/CNT fiber at original, damaged and healed states to turn on or off a LED light bulb, and images at a higher magnification showing the

damaged and healed regions on the fiber. (b) Schematic illustration of the healing process of a CS/CNT fiber exposed to water vapor: water vapor increases the swelling of the CS polymer and thus favors the chain movement and electrostatic interactions between CA^- and CS^+. (c) Repeated healing and recovery of electrical properties for five cuts on the fiber.

Mechanical tensile tests were also performed to measure the tensile properties of the CS/CNT straight and coiled fibers (30 wt % CNT, fiber diameter $D = 250$ µm) with sacrificial bonds. Figure 6.3a shows a typical stress-strain curves of straight and coiling patterned fibers with three loops. Sacrificial bonds (i.e., α, β, γ) on the coiling fibers lead to the saw-tooth shaped curve. The process of stretching bond α is illustrated at the top of Figure 6.3a with a sequence of photographs (showing neighboring α and β bonds). Similar to what Passieux *et al.* found,[30] the bond (taking bond α as an example) can transmit the force to the fiber at apparent strain $\varepsilon = 20$ % and break when reaching the maximum stress of 0.52 MPa at $\varepsilon = 50$ %. The breakage of the bond released the hidden length and a significant drop of the stress was observed due to the unfolding of the bond. After the breakage of the last bond, γ, the apparent stress σ increased and reached a local maximum value of 0.37 MPa at $\varepsilon = 180$ %, due to the tensioning and breakage of the backbone. By contrast, the straight fiber is less stretchable (strain at break of 70 %) but is stiffer (maximum $\sigma = 0.87$ MPa). There are differences between our study and the report of Passieux *et al.*[30] Our nanocomposite fibers are more stretchable than their thermoplastic (PLA) fibers, and the hidden length can be stretched straight after the bond breakage while their fibers still maintained a curved shape after breaking one bond. The full straightness in our nanocomposite fibers was most probably due to softness of our nanocomposite material, with lactic acid being used as a plasticizer. The maximum σ of the first bond α in our samples was higher than that of β (smallest) and γ (intermediate), while Passieux *et al.* observed a gradual decrease from the first to the last bond. This is probably due to the strength of the sacrificial bond, which is influenced by the repeated stretching and relaxation of the bond. The tensile properties of the microstructured fibers can be affected by relative material moisture (RM) (Figure S6.2, Supporting Information). Higher water uptake of the fibers with high RM caused a loss of rigidity and an increase of stretchability.
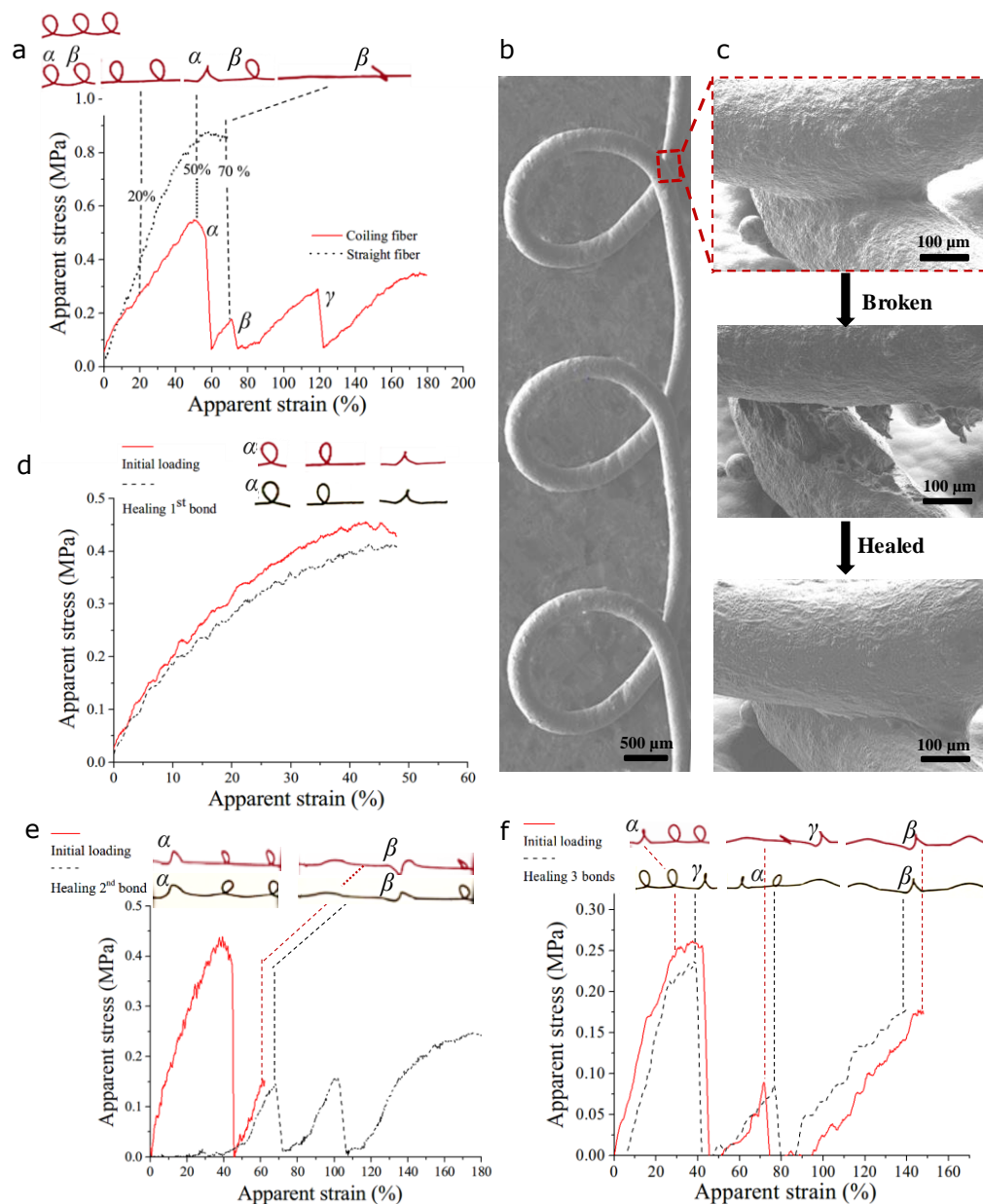
Figure 6.3: (a) Representative tensile curves of straight and coiling pattern fibers with photographs on the top to show sacrificial bond breakage and hidden length extension of bond α. (b) SEM images of a coiling pattern CS/CNT fiber (30 wt % CNT) with three bonds. (c) Top: high magnification of an original sacrificial bond in c, middle: sacrificial bond in broken and healed (bottom) states. (d) Typical tensile curves of a coiling pattern fiber for original loading with breaking of first bond and healing of the bond. (e) Typical tensile curves of a coiling pattern fiber for original loading with breaking of second bond and healing of the bond. (f) Typical tensile curves of a coiling pattern fiber with breaking and healing of all three bonds.

Figure 6.3b shows the SEM image of a coiling patterned CS/CNT fiber (30 wt % CNT, D = 250 µm) with three loops. Close-ups of one sacrificial bond of original, damaged and healed fibers in the magnified views are presented in Figure 6.3c. The sacrificial bond of the original fiber is clearly shown in Figure 6.3c (top). A broken sacrificial bond with a gap of a maximum width of 100 µm caused by stretching of the fiber is shown in Figure 6.3c (middle). After applying water vapor, the gap on the site of the broken sacrificial bond was re-closed (Figure 6.3c, bottom), resulting in the healing of its microstructure. To demonstrate the healing of the sacrificial bonds, mechanical tensile tests were conducted to compare the tensile properties of original and healed fibers with different RM level. Figure 6.3d shows representative tensile curves of an original fiber (medium RM = 18 %) with the first bonds broken, and the healed fiber with the bond restored. After breaking the second bond, the tensile properties of the second bond can also be recovered after healing the second bond (Figure 6.3e). Due to enhanced chain mobility in fibers at higher RM, healing of three consecutive bonds is achievable, as shown in typical tensile curves of these coiling patterned in Figure 6.3f. After healing all three bonds, the curve of the healed fiber was almost perfectly overlapped with that of the original fiber. The healed fiber achieved ~ 90% toughness recovery after healing all three bonds. Movie S6.2 (Supporting Information) shows the tensile tests and healing processing of original and healed coiling fibers. The comparison between healed fiber and original fiber demonstrates nearly perfect healing effect and the restoration of mechanical properties (i.e., strength, stretchability and toughness).

For further potential applications, the humidity-sensing capability of the CS/CNT fiber (10 wt % CNT) is examined under different relative humidity (RH) levels using a humidity chamber. Figure 6.4a shows the relationship between RH and electrical resistance. The resistance of the CS/CNT fiber (black curve) increased as the RH increased from 35% to 85%. Similar resistance values under the same RH (within the error bars) was measured when the RH decreased to 35%, indicating the reversibility of the sensing process. When the CS/CNT fiber was placed in a humidified environment, it can gradually swell and thus the distance between CNTs widened. Once the RH went back to the original value, the fiber dimension and CNT distance returned to its initial states, resulting in a reversible sensing process.

Due to the lightweight and flexibility of microstructured CS/CNT fibers, the fibers can be noninvasively adapted on the surface of various materials with any shape and rigidity for a wide range of applications such as strain sensors, position sensors and wearable devices. A strain sensor

was developed by depositing a CS/CNT coiling fiber on a CS film, which can be used to detect human motion. A 3D hybrid structure consisted of a coiling pattern fiber (30 wt % CNT) deposited on a flexible CS film (10 wt % CS)[38]. The sensor was attached on the outside of an elbow and was used to detect the bending motion of an arm. Figure 6.4b shows the response of the sensor to the dynamic test of bending an arm. The current signals exhibited repeatable response to the cycling activity of fully stretched arm (relaxed state) and fully bended arm (bended state). Since CS/CNT fibers adhered to the CS film, all sacrificial bonds in the sensor were disconnected once the bending force was applied (Figure 6.4c). Therefore, there was an increase of the electronic pathways (black curve in Figure 6.4c) in the sensor under tension and thus the current of the sensor decreased. The strain sensor was successful to detect the elbow movement by using a flexible supportive substrate (CS film). This strain sensor can recover the bended sensor structure to the original shape once the arm was in relaxed state, instead of using self-healing property of the nanocomposite. After the detection of large-scale motion, a spider-web-like sensor deposited on a polydimethylsiloxane (PDMS) film was investigated for detecting local deformation. Self-healing property of the nanocomposite was used for recovering the sensor structure and electrical signals. Figure 4d shows a spider-web-like sensor which consisted of coiling CS/CNT fiber in spiral thread onto straight CS fibers (10 wt %, dyed by Rhodamin B) in radical thread. The CS straight fibers separated the CS/CNT fiber into pieces with a same angle of θ (45°). Through monitoring the current of the whole CS/CNT fiber (schematic in Figure S6.3a, Supporting Information), a constant current decrease (0.002 mA) of the whole CS/CNT fiber was observed for breaking each bond by a tweezer (Figure 6.4e). The current decrease (an increase of the fiber resistance under a voltage of 5V) was due to the longer length of the fiber after bond breakage. The electronic pathway in the loop with a breakage of bond was longer than the pathway in the original loop (black curve to show the electronic pathway in the inset image of Figure 6.4e). By checking the current of each fiber piece (schematic in Figure S6.3b, Supporting Information), it is possible to know the specific position where the bond was broken. Figure 6.4f shows the current of one fiber piece where one sacrificial bond is broken in the sensor. A current decrease was measured due to one bond breakage and the current of the fiber piece can return to its initial value after healing the bond. The current change of fiber piece showed the location where one bond was broken (red curve in the inset image of Figure 6.4f). No current change was observed in the fiber piece where there was no bond breakage. This spider-web-like sensor was capable of sensing the structure change of the CS/CNT web and

showing the deformation location through observing the current signals change, which demonstrated accurate sensing performance. This sensor with a large surface area can be largely expanded at a low strain level. The combination of complex geometries and excellent sensing ability offers a proof-of-concept approach for various applications such as position sensors, wearable devices and soft robotics.
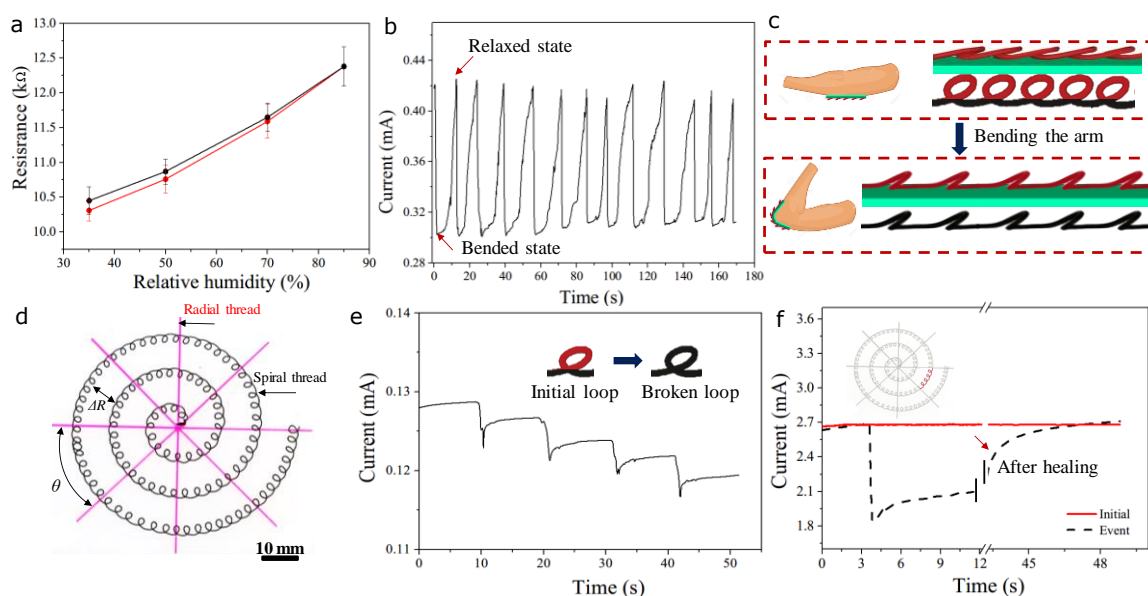
Figure 6.4: (a) Relationship between RH and electrical resistance for a CS/CNT fiber (10 wt % CNT) as a humidity sensor. (b) Current change for a strain sensor attached to the outside of an elbow to monitor the bending motion of an arm with fully stretched arm (relaxed state) and fully bended arm (bended state). (c) Schematic showing the strain sensor attached on an elbow under relaxed and bended states, and the shape change of the coiling fiber on a CS film under the force of bending the arm. The black curves show the different electronic pathways between original fiber and the fiber under tension. (d) A spider-web-like sensor formed by a coiling pattern CS/CNT fiber (30 wt % CNT) in spiral thread that was deposited on a CS network (dyed in pink) with straight fibers in radical thread. The CS fibers divided the CS/CNT fiber into pieces. This sensor was attached to a transparent PDMS film. (e) Current signals of the whole CS/CNT fiber web in response to breaking four bonds. The inset images show top views of an initial loop and the loop after breaking its sacrificial bond and the black curve shows their different electronic pathways. (f) Current signals of the fiber where one sacrificial bond was broken.

In summary, we report novel CS/CNT inks to fabricate complex 3D structures featuring self-healing, stretchable and high electrical conductivity. Various microstructured fibers and 3D structures were fabricated by facile 3D printing approaches at room temperature. By applying structural hierarchy, microstructured fiber with sacrificial bond and hidden length endow a high stretchability (maximum strain of 180 %) of the CS/CNT nanocomposite with a high CNT content (30 wt %). This room-temperature processed, fast and repeatable self-healing electronic nanocomposite material can restore its outstanding mechanical properties (i.e., stretchability, strength and toughness) and high electrical conductivity by simply applying water vapor. These CS/CNT nanocomposite instability-assisted 3D printed structures can be designed as multifunctional devices including humidity and strain sensors. The humidity sensor presents a reversible sensing ability and strain sensors are capable of sensing human motion and local deformation. The restoration of nanocomposite shape and electrical properties can be achieved either through structure design (e.g., using flexible supportive substrate) or the healing properties of nanocomposites. This work not only develops a simple strategy to design CS/CNT nanocomposites with self-healing properties, but also demonstrates the 3D printing of multidimensional structures as well as the development of strain sensor applications. We foresee that our strategy of ink design with carefully selected natural polymer, nano-fillers and non-toxic solvent with fascinating self-healing, electronic and mechanical properties enables a future class of multifunctional electronic devices and electroactive sensors.

6.3 Experimental section

Preparation of Nanocomposite Inks. CS solutions were prepared by dissolving CS (90% deacetylated, weight-average molecular weight = 207 kDa, from BioLog Heppe GmbH, Germany) in an acidic mixture (40 wt % acetic acid, 10 wt % lactic acid, 50 wt % distilled water). Citric acid 5 wt % (based on the total weight of CS + CNT) was added to the inks. Multi-walled carbon nanotubes (CNT, Nanocyl NC7000) were mixed with the CS solution via ball mixing (SPEX SamplePrep 8000M Mixer/Mill). Specifically, a 2.5 wt% (based on the total weight of the solution) chitosan solution was placed inside a ball miller with the required content of CNT (for a given CNT/chitosan ratio) and ball milled for 30 minutes. After mixing, nanocomposites with CNT concentrations of 5, 10, 20, 30, and 40 wt% (based on the total weight of CS + CNT) were obtained. After ball milling, the CS/CNT inks with different CNT concentrations were partially dried at room

temperature with simple mixing every 15 minutes. The different CNT/chitosan inks were adjusted to their total CS + CNT concentration to 25-30 wt% (based on the total weight of the ink) for 3D printing. All chemicals were purchased from Sigma-Aldrich, Canada, and used as received.

3D Printing of Microstructures. The CS/CNT inks were loaded into a syringe (3 mL, Nordson EFD) placed into the printhead which was mounted on a three-axis positioning stage and connected to a dispensing robot (Fisnar I&J2200-4). A 20-layer scaffold was fabricated using a CS/CNT ink with 30 wt% CNT and under an applied pressure of 2.2 MPa and a robot velocity of 5 mm s^{-1}, while the shape-like spider and starfish were produced using a CS/CNT ink with 10 wt% CNT under an applied pressure of 1.9 MPa and a robot velocity of 2 mm s^{-1}. The inks were extruded through a micronozzle (Nordson EFD) under an applied pressure that was controlled by a dispensing apparatus (HP-7X, Nordson EFD). The CS/CNT structures were fabricated by depositing CS/CNT filaments in a layer–by-layer manner, which was followed by the filament solidification through solvent evaporation. The files for digital 3D model of those microstructures were acquired by Thingiverse (http://www.thingiverse.com/). A software (Simplify3D) was used to generate codes from those files for 3D printing. CS/CNT fibers featuring sacrificial bonds were fabricated by instability-assisted 3D printing (IA3DP). A CS/CNT ink (30 wt % of CNT) was extruded at a speed V_t through a 410 µm nozzle (Nordson EFD). CS/CNT fibers with different patterns were fabricated by changing the applied pressure to control the speed ratio (V_t/V_p) (Table S6.1, Supporting Information) at a robot velocity of 2 mm s^{-1} under a distance ratio (*H/D*) of 10. The morphology of those microstructures was observed by an optical microscope (BX-61, Olympus).

Conductivity Measurements. The electrical conductivity tests were performed on fibers of CS/CNT nanocomposites. CS/CNT inks with different CNT concentrations (5, 10, 20, 30 and 40 wt %) were extruded through a 410 µm nozzle to prepare the samples. The resistance of the fiber samples was measured by a Keithley 6517A electrometer connected to a Keithley 8009 test fixture (Keithley Instruments, USA). The diameters of the fibers were observed by an optical microscope (BX-61, Olympus) and the lengths of the fibers were measured by a digital caliper (Lyman electronic digital caliper). The volume conductivity was calculated from the resistance values considering the length and cross-section area of the fiber samples.

Self-Healing Behavior. CS/CNT fibers were cut with a standard razor blade. Water vapor (deionized water) was sprayed for 10 s onto the samples using a humidifier to heal the samples. The healed fibers were dried by a hair dryer until the current back to the initial values. Electrical measurements were performed on original and healed fibers using a Keithley 6517A electrometer connected to data collecting software.

Mechanical Testing. Mechanical tests were performed on straight and coiling patterned fibers using an electromechanical machine (Insight MTS 50kN) with a 5 N load cell. The coiling pattern fibers with different relative moistures (14, 18 and 21 %) were also tested. The fiber moisture was determined through thermogravimetric analysis (TGA, TA Instruments Q500, USA) by performing an isothermal test at a temperature of 100 °C maintained for 30 min, using a heating rate of 50 °C/min to reach the set temperature and under a nitrogen atmosphere. The tensile properties of original and healed fibers with RM of 18 and 21 % were also determined. Water vapor (deionized water) was sprayed for 10 ~ 60 s (depending on different RM of samples) onto the samples using a humidifier to heal the fibers for restoring tensile properties. Tests were repeated seven times using the standard of ASTM D3822 / D3822M for each set of parameters. SEM images were performed with a JEOL JSM-7600TFE Field Emission Scanning Electron Microscope.

Fabrication and Characterization of the Sensors. To record the resistance of CS/CNT fibers at different RH, a conductive CS/CNT fiber (10 wt %) was incubated at different RH levels in a Cole-Parmer humidity-controlled chamber (03323-14). Electrical measurements were performed to measure the resistance change using a Keithley 6517A electrometer connected to a data collecting software. A flexible CS film (8 wt % CS) was fabricated by SC3DP at a robot velocity of 3 mm s^{-1} and a pressure of 1.1 MPa, and a coiling pattern fiber (30 wt %, RM of 18 %) fabricated by IA3DP at a robot velocity of 2 mm s^{-1} was deposited on the CS film. This structure was used as a strain sensor and the sensing ability was observed by bending an arm. A spider-web-like sensor was used to observe local motion through bond breaking and healing. Pink CS (10 wt %, dyed by Rhodamine B) straight fibers were fabricated by 3DP on a PDMS film. A coiling pattern fiber (30 wt % CNT) generated in a spiral path was deposited by IA3DP onto the pink CS network. The bond was broken by a tweezer and the bonds were healed under water vapor (~10 s) and were dried by a hair dryer for restoring electrical conductivity. The electrical conductivity tests were performed on the strain and web sensors under a voltage of 5 V by using Keithley 6517A electrometer.

6.4 Acknowledgements

6.5 Supporting information
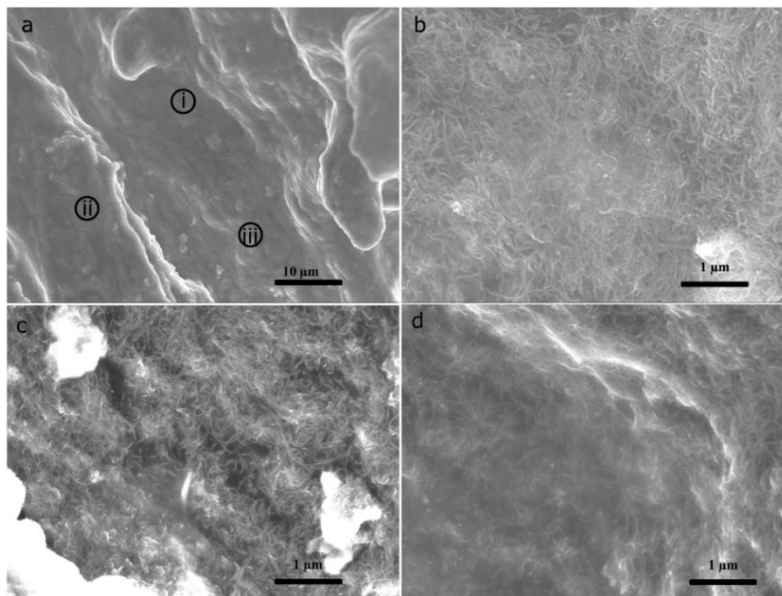
Figure S6.1: (a) SEM images of CS/CNT nanocomposite (30 wt % CNT) morphology in the cross-section of a CS/CNT fiber. (b), (c) and (d) show CNT homogeneous distribution in the nanocomposite at higher magnification SEM images of the nanocomposite morphology at different positions (i, ii, and iii) in (a).

Table S6.1: Different patterned CS/CNT fibers were generated by IA3DP (instability assisted 3D printing) through changing speed ratio (V_t/V_p) under the same distance ratio of distance/nozzle diameter (H/D) = 10

Speed ratio (V_t/V_p)	Fiber patterns	
< 1	Break or thin straight fiber	
= 1	Straight fiber	
Slightly larger than 1	Meandering pattern	
1.6 ~ 2.5	Alternating or coiling pattern	
2.5 ~ 3.5	Coiling pattern	
> 3.5	Overlapping pattern	

Movie S6.1: Instability-assisted 3D printing of microstructured CS/CNT fibers.
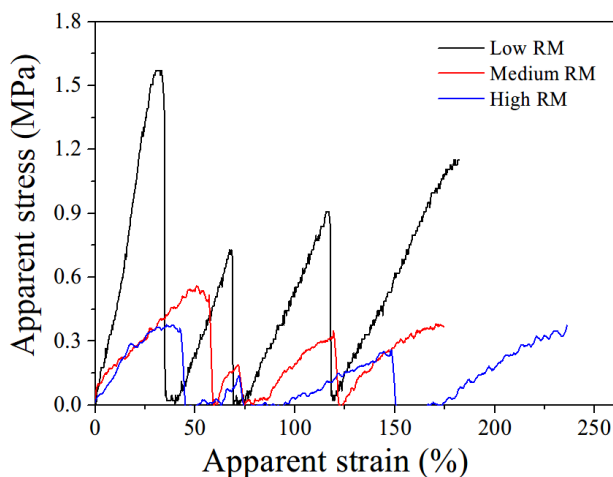
Figure S6.2: Typical tensile curves of coiling pattern fibers with different RM level of (low RM = 14 %, medium RM = 18 %, high RM = 21 %, H/D = 10).
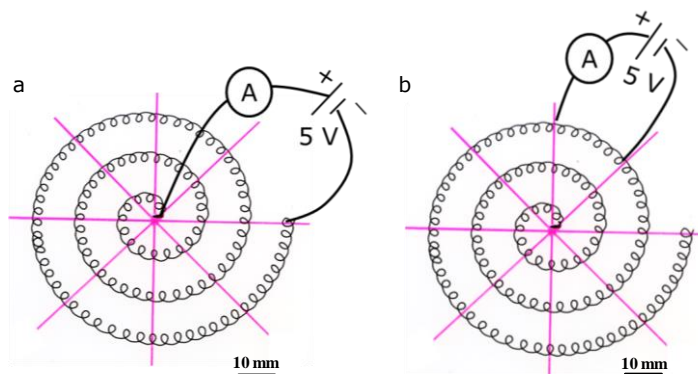
Figure S6.3: (a) Wiring schematic for measuring the current of one fiber piece in the spider-web-like sensor. (b) Wiring schematic for measuring the current of the whole fiber in the sensor.

References

[1]   M. Eriksen, L. C. Lebreton, H. S. Carson, M. Thiel, C. J. Moore, J. C. Borerro, *et al.*, "Plastic pollution in the world's oceans: more than 5 trillion plastic pieces weighing over 250,000 tons afloat at sea," *PloS one,* vol. 9, p. e111913, 2014.

[2]   P. Kiddee, R. Naidu, and M. H. Wong, "Electronic waste management approaches: An overview," *Waste Management,* vol. 33, pp. 1237-1250, 2013.

[3]   M. Rinaudo, "Chitin and chitosan: properties and applications," *Progress in polymer science,* vol. 31, pp. 603-632, 2006.

[4]   B. Zhu, H. Wang, W. R. Leow, Y. Cai, X. J. Loh, M. Y. Han, *et al.*, "Silk fibroin for flexible electronic devices," *Advanced Materials,* vol. 28, pp. 4250-4265, 2016.

[5]   Z. Lei, Q. Wang, S. Sun, W. Zhu, and P. Wu, "A Bioinspired Mineral Hydrogel as a Self‑Healable, Mechanically Adaptable Ionic Skin for Highly Sensitive Pressure Sensing," *Advanced Materials,* vol. 29, 2017.

[6]   T. P. Huynh, P. Sonar, and H. Haick, "Advanced Materials for Use in Soft Self‑Healing Devices," *Advanced Materials,* vol. 29, 2017.

[7]   J. Y. Oh, S. Rondeau-Gagné, Y.-C. Chiu, A. Chortos, F. Lissel, G.-J. N. Wang*, et al.*, "Intrinsically stretchable and healable semiconducting polymer for organic transistors," *Nature,* vol. 539, p. 411, 2016.

[8]   D. Rus and M. T. Tolley, "Design, fabrication and control of soft robots," *Nature,* vol. 521, p. 467, 2015.

[9]   Y. Zhang, B. Yang, X. Zhang, L. Xu, L. Tao, S. Li*, et al.*, "A magnetic self-healing hydrogel," *Chemical Communications,* vol. 48, pp. 9305-9307, 2012.

[10]   J. A. Neal, D. Mozhdehi, and Z. Guan, "Enhancing mechanical performance of a covalent self-healing material by sacrificial noncovalent bonds," *Journal of the American Chemical Society,* vol. 137, pp. 4846-4850, 2015.

[11]   X. Chen, M. A. Dam, K. Ono, A. Mal, H. Shen, S. R. Nutt*, et al.*, "A thermally re-mendable cross-linked polymeric material," *Science,* vol. 295, pp. 1698-1702, 2002.

[12]   M. Burnworth, L. Tang, J. R. Kumpfer, A. J. Duncan, F. L. Beyer, G. L. Fiore*, et al.*, "Optically healable supramolecular polymers," *Nature,* vol. 472, p. 334, 2011.

[13]   P. Cordier, F. Tournilhac, C. Soulié-Ziakovic, and L. Leibler, "Self-healing and thermoreversible rubber from supramolecular assembly," *Nature,* vol. 451, p. 977, 2008.

[14]   Y. Amamoto, H. Otsuka, A. Takahara, and K. Matyjaszewski, "Self‑healing of covalently cross‑linked polymers by reshuffling thiuram disulfide moieties in air under visible light," *Advanced Materials,* vol. 24, pp. 3975-3980, 2012.

[15]   S. A. Odom, S. Chayanupatkul, B. J. Blaiszik, O. Zhao, A. C. Jackson, P. V. Braun*, et al.*, "A Self‑healing Conductive Ink," *Advanced Materials,* vol. 24, pp. 2578-2581, 2012.

[16]   K. Guo, D. L. Zhang, X. M. Zhang, J. Zhang, L. S. Ding, B. J. Li*, et al.*, "Conductive Elastomers with Autonomic Self‑Healing Properties," *Angewandte Chemie,* vol. 127, pp. 12295-12301, 2015.

[17]   S. Zhang and F. Cicoira, "Water‑Enabled Healing of Conducting Polymer Films," *Advanced Materials,* vol. 29, 2017.

[18]   Y. He, S. Liao, H. Jia, Y. Cao, Z. Wang, and Y. Wang, "A Self‑Healing Electronic Sensor Based on Thermal‑Sensitive Fluids," *Advanced Materials,* vol. 27, pp. 4622-4627, 2015.

[19]   E. Palleau, S. Reece, S. C. Desai, M. E. Smith, and M. D. Dickey, "Self‑healing stretchable wires for reconfigurable circuit wiring and 3D microfluidics," *Advanced Materials,* vol. 25, pp. 1589-1592, 2013.

[20]   S.-K. Kang, R. K. Murphy, S.-W. Hwang, S. M. Lee, D. V. Harburg, N. A. Krueger*, et al.*, "Bioresorbable silicon electronic sensors for the brain," *Nature,* vol. 530, pp. 71-76, 2016.

[21] C. W. Park, S. K. Kang, H. L. Hernandez, J. A. Kaitz, D. S. Wie, J. Shin, *et al.*, "Thermally triggered degradation of transient electronic devices," *Advanced Materials,* vol. 27, pp. 3783-3788, 2015.

[22] H. Jinno, K. Kuribara, M. Kaltenbrunner, N. Matsuhisa, T. Someya, T. Yokota, *et al.*, "Printable elastic conductors with a high conductivity for electronic textile applications," *Nature communications,* vol. 6, p. 7461, 2015.

[23] Y. Huang, M. Zhong, Y. Huang, M. Zhu, Z. Pei, Z. Wang, *et al.*, "A self-healable and highly stretchable supercapacitor based on a dual crosslinked polyelectrolyte," *Nature communications,* vol. 6, p. 10310, 2015.

[24] E. B. Secor, S. Lim, H. Zhang, C. D. Frisbie, L. F. Francis, and M. C. Hersam, "Gravure printing of graphene for large‐area flexible electronics," *Advanced materials,* vol. 26, pp. 4533-4538, 2014.

[25] M. Moniruzzaman and K. I. Winey, "Polymer nanocomposites containing carbon nanotubes," *Macromolecules,* vol. 39, pp. 5194-5205, 2006.

[26] M. K. Shin, J. Oh, M. Lima, M. E. Kozlov, S. J. Kim, and R. H. Baughman, "Elastomeric conductive composites based on carbon nanotube forests," *Advanced materials,* vol. 22, pp. 2663-2667, 2010.

[27] H. Liu, J. Gao, W. Huang, K. Dai, G. Zheng, C. Liu, *et al.*, "Electrically conductive strain sensing polyurethane nanocomposites with synergistic carbon nanotubes and graphene bifillers," *Nanoscale,* vol. 8, pp. 12977-12989, 2016.

[28] S. Zhou, S. Zeng, S. Zhang, J. Qiao, J. Di, M. Chen, *et al.*, "Hierarchical carbon nanotube hybrid films for high-performance all-solid-state supercapacitors," *RSC Advances,* vol. 7, pp. 52010-52016, 2017.

[29] V. K. Rangari, M. Yousuf, S. Jeelani, M. X. Pulikkathara, and V. N. Khabashesku, "Alignment of carbon nanotubes and reinforcing effects in nylon-6 polymer composite fibers," *Nanotechnology,* vol. 19, p. 245703, 2008.

[30] R. Passieux, L. Guthrie, S. H. Rad, M. Lévesque, D. Therriault, and F. P. Gosselin, "Instability‐Assisted Direct Writing of Microstructured Fibers Featuring Sacrificial Bonds," *Advanced Materials,* vol. 27, pp. 3676-3680, 2015.

[31] H. Okimoto, T. Takenobu, K. Yanagi, Y. Miyata, H. Shimotani, H. Kataura, *et al.*, "Tunable Carbon Nanotube Thin‐Film Transistors Produced Exclusively via Inkjet Printing," *Advanced materials,* vol. 22, pp. 3981-3986, 2010.

[32] S.-z. Guo, X. Yang, M.-C. Heuzey, and D. Therriault, "3D printing of a multifunctional nanocomposite helical liquid sensor," *Nanoscale,* vol. 7, pp. 6451-6456, 2015.

[33] K. Chizari, M. A. Daoud, A. R. Ravindran, and D. Therriault, "3D Printing of Highly Conductive Nanocomposites for the Functional Optimization of Liquid Sensors," *Small,* vol. 12, pp. 6076-6082, 2016.

[34] A. E. Jakus, E. B. Secor, A. L. Rutz, S. W. Jordan, M. C. Hersam, and R. N. Shah, "Three-dimensional printing of high-content graphene scaffolds for electronic and biomedical applications," *ACS nano,* vol. 9, pp. 4636-4648, 2015.

[35]   Y. Hu, S. J. Noelck, and R. A. Drezek, "Symmetry breaking in gold − silica − gold multilayer nanoshells," *Acs Nano,* vol. 4, pp. 1521-1528, 2010.

[36]   L. Lu and W. Chen, "Biocompatible composite actuator: a supramolecular structure consisting of the biopolymer chitosan, carbon nanotubes, and an ionic liquid," *Advanced Materials,* vol. 22, pp. 3745-3748, 2010.

[37]   C. Chen, C. Yang, S. Li, and D. Li, "A three-dimensionally chitin nanofiber/carbon nanotube hydrogel network for foldable conductive paper," *Carbohydrate polymers,* vol. 134, pp. 309-313, 2015.

[38]   Q. Wu, M. Maire, S. Lerouge, D. Therriault, and M. C. Heuzey, "3D printing of microstructured and stretchable chitosan hydrogel for guided cell growth," *Advanced Biosystems,* vol. 1, 2017.

[39]   Q. Meng, M.-C. Heuzey, and P. J. Carreau, "Hierarchical structure and physicochemical properties of plasticized chitosan," *Biomacromolecules,* vol. 15, pp. 1216-1224, 2014.

CHAPTER 7   GENERAL DISCUSSION

7.1 3D printing of chitosan

3D printing with various light- and ink- based printing methods allows the digital design of a wide range of materials. Despite great progress made in recent decades, 3D printing is still mainly based on the fabrication of rigid architectures by using materials such as thermoplastic polymers in fused deposition modelling (FDM), polymeric or metallic powders in selective laser sintering (SLS), and photopolymerizable resins in stereolithography (SLA). Those materials are adequate for fabricating complex 3D structures, but they are not ideal for tailoring multifunctional materials. Although soft materials such as hydrogels, colloidal suspensions and natural polymers have been developed to fabricate different structures for potential applications, their fabrication processes always need external support for the structure during the printing process, such as using coagulation in reservoir or low-temperature plate to solidify the ink filament. Unlike rigid materials, they are too soft to support themselves. Currently, the level of manufacturing of soft structures is relatively simplistic [97]. For 3D printing used in tissue engineering (TE), the main problem is that the manufacturing of complex and tissue-mimicking structures with high resolution gives restricted conditions for the properties of the ink. As shown in our processing map, the area for the fabrication of 3D scaffold is narrower than that for the fabrication of 1D and 2D structures. In order to fabricate a structure with high shape fidelity, polymers with high concentration or high crosslinking density are used to improve the printability. Since cells show higher affinity in an aqueous environment, concentrated hydrogels are not ideal for TE. Therefore, there is a conflict between obtaining high shape fidelity and cell viability.

In this work, we developed a natural polymer-based ink that can be directly printed in air at room temperature by 3D printing. The successful 3D printing was achieved by tailoring the solvent evaporation and ink rheological properties through ink composition, without the use of external supports such as bath or low-temperature assisted steps. Fabrication parameters like applied pressure, nozzle diameter and robot velocity were shown to affect the printed 3D structures. Various 1D filaments, 2D arrays and 3D self-supporting structures with a high resolution of 30 μm were fabricated, demonstrating a high fidelity of the printing process. However, due to a relatively low solvent evaporation rate used in our fabrication, it may need a longer time to fabricate a relatively large object. Fast solvent evaporation rate can help shape solidification after printing in

a short time, but it may easily cause clogging in the nozzle during printing. After printing, a gelation step was used to obtain a physical CS hydrogel by neutralization of CS scaffolds in a sodium hydroxide solution. There were micro-wrinkles formed on the surface of the scaffolds due to a volume change in the gelation step. For the first time, 3D CS scaffold fabricated by 3D printing with a wrinkled surface that can guide cell growth and induce cell alignment were obtained. There is a need for more detailed work on the control of wrinkle formation (such as using different concentrations of NaOH solutions, etc.). We could also investigate other natural polymers such as collagen and alginate to see whether they have similar performance to chitosan.

7.2 3D printing of chitosan-based conductive nanocomposites

Conductive polymer-based nanocomposites (CPN) are attractive materials for fabrication of multifunctional electronic devices. So far, traditional methods such as solvent casting [66] and wet spinning [150] have been developed to fabricate CPN. However, they allow limited control on the manufacturing of complex and precise structures for the targeted applications. 3D printing has drawn important attention for the fabrication of conductive inks due to its ability to fabricate customized 3D structures. Currently, the conductive materials used in 3D printing are usually metals that can be produced by printing techniques such as selective laser melting (SLM) [151]. Some 3D printing techniques such as fused deposition modeling (FDM) have limitations to fabricate CPN since the inks can easily undergo clogging during extrusion through a micronozzle under high melting temperature. Therefore, there is a need to design novel nanocomposite inks for 3D printing with a high printability and structure fidelity.

We firstly reported CS/CNT inks with a high nanofiller content ($\leq$ 30 wt %) that can be fabricated by 3D printing to obtain various 3D structures at room temperature. The preparation of CNT-based nanocomposites with well-dispersed nanofillers in the polymer matrix is important for 3D printing (avoid clogging). Mixing methods such as extrusion and solution mixing have limitations for mixing CNT/polymer at high CNT concentrations (> 10 wt %). In order to achieve high conductivity, a high content of CNTs (up to 40 wt %) was used in the nanocomposites by a ball mill mixing method. This method can achieve high content of nanofillers with good dispersion. Normally, a high loading of nanofillers results in stiffer and less stretchable nanocomposite materials. But the stretchability is favorable for electronic applications. Thus, we fabricated

microstructured CS/CNT fibers by instability-assisted 3D printing. The fibers featured sacrificial bonds and hidden length that allow achieving high stretchability.

Self-healing materials have been developed for electronic applications, due to their ability to heal damage for restoring the material properties and prolonging the material lifetime. Most self-healing materials are insulating and usually involve complicated preparation steps (e.g., chemical modification and polymer synthesis). Harsh processing conditions (e.g., toxic solvents and high temperature) are also commonly used in the self-healing process. The integration of self-healing polymers with conductive nanofillers such as CNTs and graphene may address these limitations. We developed self-healing CS/CNT nanocomposites that can restore mechanical and electrical properties under exposure to water vapor at room temperature. Non-toxic solvents (acetic acid and lactic acid) were involved in this process. The self-healing of nanocomposite was attributed to electrostatic interactions between negative citrate ions in the healing agent (citric acid) and positively charged amino groups, as well as polymer swelling under the application of water vapor. However, this method used acidic solvents for chitosan, which may limit the extension of this method to other natural polymers. Furthermore, self-healing materials are normally fabricated into films and sometimes they have rigid morphology and definite structures [152], which limit their potential applications in multidimensional spaces. 3D printing was used in this work to fabricate self-healing CS/CNT nanocomposites into various complex structures (e.g., 3D scaffold and microstructured fibers) at room temperature. Water-triggered self-healing nanocomposites were also developed to fabricate humidity and strain sensors with hybrid structures (microstructured fibers attached on a film). Although the strain sensors were capable of sensing humidity change, human elbow motion and local deformation, more versatile smart devices accompanied with self-healing property and complex or hybrid 3D structures should be developed for more advanced applications.

CHAPTER 8   CONCLUSION AND RECOMMENDATIONS

8.1 Conclusion

In this thesis, the 3D printing technique was applied to fabricate various structures using natural polymer (CS) and its nanocomposite inks. The effects of ink properties (concentration, viscosity, nanofiller content and solvent evaporation rate) and printing parameters (nozzle diameter, applied pressure and robot velocity) on printability were characterized. Applications for guiding cell growth and sensors for detecting human motion and humidity were presented. The conclusions drawn from this work are presented below:

CS solutions (4-12 wt %) in an acidic mixture of acetic acid, lactic acid and citric acid were investigated for their printability. These acids were selected, since they are "green" solvents and non-toxic. CS solutions (6, 8, 10 wt %) exhibited shear-thinning behavior, which was observed from the viscosity measured by rotational rheometer and process-related apparent viscosity obtained from capillary flow analysis. The shear-thinning behavior benefited the solution flow from a micronozzle for 3D printing at room temperature. Once the solution was extruded from the micronozzle, the rigidity of CS filament increased due to the solvent evaporation. The solvent evaporation rate could be tailored by solvent content and composition. Acetic acid (volatile solvent) can evaporate during the printing process. Lactic acid and citric acid (non-volatile solvent) can remain in the filament to avoid drying-induced shrinkage of deposited filaments.

The 8 and 10 wt % CS solutions were successfully employed to fabricate 3D scaffold, while the 6 wt % CS solution can be used to fabricate 2D arrays. It was difficult to fabricate continuous filament to form structures using both too dilute (the concentration of CS solution < 4 wt %) or too viscous CS solutions (the concentration of CS solution > 11 wt %). The area of processing map for fabricating 3D scaffold was narrower than that for fabricating 1D filament and 2D arrays, showing more restricted conditions for the fabrication of 3D scaffold. After 3D printing, a neutralization step was used to form CS hydrogel. 3D hydrogel scaffold with wrinkled surface was obtained after neutralization. The wrinkled surface and/or the architecture of the scaffold itself worked as topographical cues that could guide cell growth and induce cell alignment.

CS/CNT nanocomposites were prepared to achieve conductivity and self-healing for different applications. The nanocomposites with different nanofiller loadings (5, 10, 20, 30, 40 wt %) were

prepared to examine their electrical conductivity. The conductivity of the deposited CS/CNT filaments presented a nonlinear increase with an increase of CNT loading. A maximum conductivity of about 1450 S/m was obtained using a 40 wt % CNT loading.

The self-healing of CS/CNT nanocomposites composed of CS as polymer binder, CNTs, and a dispersing solution (a mixture of acetic acid, lactic acid, citric acid and distilled water) was investigated. The nanocomposite could heal itself by exposure to water vapor. A CS/CNT fiber (30 wt % CNT) was used to demonstrate the healing process. Optical microscopy images of the damaged fiber (with a ~50 µm gap) and healed fiber showed the use of water vapor to enable the healing of the nanocomposite. The healing was rapid, with a response time of ~10 s. Under water vapor, the CS/CNT fiber swelled due to higher water-uptake of the polymer in a moisture atmosphere. The swelling of CS improved the polymer chains movement and the electrostatic interactions between citrate ions in the nanocomposite and NH_3^+ on CS chains, which contributed to the healing of the damaged fiber.

High CNT loadings were used to achieve high conductivity, but high loading of CNTs can significantly affect the nanocomposite stiffness and reduce its stretchability. Microstructured CS/CNT fibers featuring sacrificial bond and hidden length were fabricated by instability-assisted 3D printing, which significantly increase their stretchability (strain at break of 230% in microstructured fiber, 70% in straight fiber). The nanocomposite can be used as a sensor to detect humidity due to CS polymer swelling under a moisture environment. The feasibility of forming strain sensors was investigated by fabricating microstructured fiber/CS film hybrid structure to detect large human motion such as elbow motions. A spider-web-like sensor was used to detect local deformation by applying self-healing behavior of nanocomposites.

The novel 3D-printing technique demonstrated here allows fabricating various structures using CS and CS/CNT nanocomposite, showing a versatile, easy-to-use and reliable printing process. We foresee that our strategy of ink design with carefully selected natural polymers, nano-fillers and non-toxic solvents with fascinating self-healing, electronic and mechanical properties will enable a future class of multifunctional electronic devices and electroactive sensors.

8.2 Recommendations

Recommendations for future work are as follows:

1) Other natural polymers such as alginate and silk fibroin may be employed as new inks for our 3D printing method.

2) Mechanical properties of CS scaffolds should be studied as functions of time during biodegradation for further application of cell growth.

3) The effect of fiber patterns, fiber hidden length, CNT loading and bending angle degree on the strain sensor ability should be further investigated.

4) Modeling and simulation should be carried out to compare with the experimental data of the resistance changes of microstructured fibers under stretching.

5) Sensors developed in this work are mainly used to detect strain change. They may be developed to more versatile sensors such as detecting temperature, due to their resistance difference in different water content.

6) Other conductive nanofillers such as graphene and silver nanoparticles should also be investigated to compare the conductivity and mechanical properties of CS-based nanocomposites.

BIBLIOGRAPHY

[1] V. Mouriño and A. R. Boccaccini, "Bone tissue engineering therapeutics: controlled drug delivery in three-dimensional scaffolds," *Journal of the Royal Society Interface,* vol. 7, pp. 209-227, 2010.

[2] M. Boffito, S. Sartori, and G. Ciardelli, "Polymeric scaffolds for cardiac tissue engineering: requirements and fabrication technologies," *Polymer International,* vol. 63, pp. 2-11, 2014.

[3] K. Y. Lee and D. J. Mooney, "Hydrogels for tissue engineering," *Chemical reviews,* vol. 101, pp. 1869-1880, 2001.

[4] J. Malda, J. Visser, F. P. Melchels, T. Jüngst, W. E. Hennink, W. J. Dhert, *et al.*, "25th anniversary article: engineering hydrogels for biofabrication," *Advanced materials,* vol. 25, pp. 5011-5028, 2013.

[5] M. Dash, F. Chiellini, R. Ottenbrite, and E. Chiellini, "Chitosan—A versatile semi-synthetic polymer in biomedical applications," *Progress in Polymer Science,* vol. 36, pp. 981-1014, 2011.

[6] N. Boucard, C. Viton, and A. Domard, "New aspects of the formation of physical hydrogels of chitosan in a hydroalcoholic medium," *Biomacromolecules,* vol. 6, pp. 3227-3237, 2005.

[7] A. G. Mikos and J. S. Temenoff, "Formation of highly porous biodegradable scaffolds for tissue engineering," *Electronic Journal of Biotechnology,* vol. 3, pp. 23-24, 2000.

[8] E. Sachlos and J. Czernuszka, "Making tissue engineering scaffolds work. Review: the application of solid freeform fabrication technology to the production of tissue engineering scaffolds," *Eur Cell Mater,* vol. 5, pp. 39-40, 2003.

[9] I. Adekogbe and A. Ghanem, "Fabrication and characterization of DTBP-crosslinked chitosan scaffolds for skin tissue engineering," *Biomaterials,* vol. 26, pp. 7241-7250, 2005.

[10] P. Sangsanoh, O. Suwantong, A. Neamnark, P. Cheepsunthorn, P. Pavasant, and P. Supaphol, "< i> In vitro</i> biocompatibility of electrospun and solvent-cast chitosan substrata towards Schwann, osteoblast, keratinocyte and fibroblast cells," *European Polymer Journal,* vol. 46, pp. 428-440, 2010.

[11] X. Zong, H. Bien, C.-Y. Chung, L. Yin, D. Fang, B. S. Hsiao, *et al.*, "Electrospun fine-textured scaffolds for heart tissue constructs," *Biomaterials,* vol. 26, pp. 5330-5338, 2005.

[12] Z. Jian-zhong, W. Jiu-Gen, and M. Jia-Ju, "Porous structures of natural materials and bionic design," *Journal of Zhejiang University Science A,* vol. 6, pp. 1095-1099, 2005.

[13] E. L. De Mulder, P. Buma, and G. Hannink, "Anisotropic porous biodegradable scaffolds for musculoskeletal tissue engineering," *Materials,* vol. 2, pp. 1674-1696, 2009.

[14] M. Rinaudo, "Chitin and chitosan: properties and applications," *Progress in polymer science,* vol. 31, pp. 603-632, 2006.

[15] B. Zhu, H. Wang, W. R. Leow, Y. Cai, X. J. Loh, M. Y. Han, *et al.*, "Silk fibroin for flexible electronic devices," *Advanced Materials,* vol. 28, pp. 4250-4265, 2016.

[16] Z. Lei, Q. Wang, S. Sun, W. Zhu, and P. Wu, "A Bioinspired Mineral Hydrogel as a Self‑Healable, Mechanically Adaptable Ionic Skin for Highly Sensitive Pressure Sensing," *Advanced Materials,* vol. 29, 2017.

[17] T. P. Huynh, P. Sonar, and H. Haick, "Advanced Materials for Use in Soft Self‑Healing Devices," *Advanced Materials,* vol. 29, 2017.

[18] J. Y. Oh, S. Rondeau-Gagné, Y.-C. Chiu, A. Chortos, F. Lissel, G.-J. N. Wang, *et al.*, "Intrinsically stretchable and healable semiconducting polymer for organic transistors," *Nature,* vol. 539, p. 411, 2016.

[19] D. Rus and M. T. Tolley, "Design, fabrication and control of soft robots," *Nature,* vol. 521, p. 467, 2015.

[20] R. Dermanaki Farahani and M. Dubé, "Printing polymer nanocomposites and composites in three dimensions," *Advanced Engineering Materials,* vol. 20, p. 1700539, 2018.

[21] R. D. Farahani, H. Dalir, V. Le Borgne, L. A. Gautier, M. A. El Khakani, M. Lévesque, *et al.*, "Direct-write fabrication of freestanding nanocomposite strain sensors," *Nanotechnology,* vol. 23, p. 085502, 2012.

[22] P. H. Warnke, H. Seitz, F. Warnke, S. T. Becker, S. Sivananthan, E. Sherry, *et al.*, "Ceramic scaffolds produced by computer‑assisted 3D printing and sintering: Characterization and biocompatibility investigations," *Journal of Biomedical Materials Research Part B: Applied Biomaterials,* vol. 93, pp. 212-217, 2010.

[23] D. Therriault, R. F. Shepherd, S. R. White, and J. A. Lewis, "Fugitive inks for Direct‑Write assembly of Three‑Dimensional microvascular networks," *Advanced Materials,* vol. 17, pp. 395-399, 2005.

[24] S. Ghosh, S. T. Parker, X. Wang, D. L. Kaplan, and J. A. Lewis, "Direct‑Write Assembly of Microperiodic Silk Fibroin Scaffolds for Tissue Engineering Applications," *Advanced Functional Materials,* vol. 18, pp. 1883-1889, 2008.

[25] S. Z. Guo, F. Gosselin, N. Guerin, A. M. Lanouette, M. C. Heuzey, and D. Therriault, "Solvent‑cast three‑dimensional printing of multifunctional microsystems," *Small,* vol. 9, pp. 4118-4122, 2013.

[26] S. Hong, D. Sycks, H. F. Chan, S. Lin, G. P. Lopez, F. Guilak, *et al.*, "3D printing of highly stretchable and tough hydrogels into complex, cellularized structures," *Advanced materials,* vol. 27, pp. 4035-4040, 2015.

[27] T. Ang, F. Sultana, D. Hutmacher, Y. S. Wong, J. Fuh, X. Mo, *et al.*, "Fabrication of 3D chitosan–hydroxyapatite scaffolds using a robotic dispensing system," *Materials science and engineering: C,* vol. 20, pp. 35-42, 2002.

[28] L. Geng, W. Feng, D. W. Hutmacher, Y. San Wong, H. T. Loh, and J. Y. Fuh, "Direct writing of chitosan scaffolds using a robotic system," *Rapid Prototyping Journal,* vol. 11, pp. 90-97, 2005.

[29] T. J. Hinton, Q. Jallerat, R. N. Palchesko, J. H. Park, M. S. Grodzicki, H.-J. Shue, *et al.*, "Three-dimensional printing of complex biological structures by freeform reversible embedding of suspended hydrogels," *Science advances,* vol. 1, p. e1500758, 2015.

[30] H. Okimoto, T. Takenobu, K. Yanagi, Y. Miyata, H. Shimotani, H. Kataura*, et al.*, "Tunable Carbon Nanotube Thin‐Film Transistors Produced Exclusively via Inkjet Printing," *Advanced materials,* vol. 22, pp. 3981-3986, 2010.

[31] S.-z. Guo, X. Yang, M.-C. Heuzey, and D. Therriault, "3D printing of a multifunctional nanocomposite helical liquid sensor," *Nanoscale,* vol. 7, pp. 6451-6456, 2015.

[32] K. Chizari, M. A. Daoud, A. R. Ravindran, and D. Therriault, "3D Printing of Highly Conductive Nanocomposites for the Functional Optimization of Liquid Sensors," *Small,* vol. 12, pp. 6076-6082, 2016.

[33] A. E. Jakus, E. B. Secor, A. L. Rutz, S. W. Jordan, M. C. Hersam, and R. N. Shah, "Three-dimensional printing of high-content graphene scaffolds for electronic and biomedical applications," *ACS nano,* vol. 9, pp. 4636-4648, 2015.

[34] K. Harish Prashanth and R. Tharanathan, "Chitin/chitosan: modifications and their unlimited application potential—an overview," *Trends in food science & technology,* vol. 18, pp. 117-131, 2007.

[35] K. S. Katti, D. R. Katti, and R. Dash, "Synthesis and characterization of a novel chitosan/montmorillonite/hydroxyapatite nanocomposite for bone tissue engineering," *Biomedical Materials,* vol. 3, p. 034122, 2008.

[36] F. Croisier and C. Jérôme, "Chitosan-based biomaterials for tissue engineering," *European Polymer Journal,* vol. 49, pp. 780-792, 2013.

[37] C. Pillai, W. Paul, and C. P. Sharma, "Chitin and chitosan polymers: Chemistry, solubility and fiber formation," *Progress in Polymer Science,* vol. 34, pp. 641-678, 2009.

[38] M. Rinaudo, G. Pavlov, and J. Desbrieres, "Influence of acetic acid concentration on the solubilization of chitosan," *Polymer,* vol. 40, pp. 7029-7032, 1999.

[39] S. V. Madihally and H. W. Matthew, "Porous chitosan scaffolds for tissue engineering," *Biomaterials,* vol. 20, pp. 1133-1142, 1999.

[40] L. Ilium, "Chitosan and its use as a pharmaceutical excipient," *Pharmaceutical research,* vol. 15, pp. 1326-1331, 1998.

[41] L. Hu, Y. Sun, and Y. Wu, "Advances in chitosan-based drug delivery vehicles," *Nanoscale,* vol. 5, pp. 3103-3111, 2013.

[42] J. Berger, M. Reist, J. Mayer, O. Felt, N. Peppas, and R. Gurny, "Structure and interactions in covalently and ionically crosslinked chitosan hydrogels for biomedical applications," *European Journal of Pharmaceutics and Biopharmaceutics,* vol. 57, pp. 19-34, 2004.

[43] I. Aranaz, M. Mengíbar, R. Harris, I. Paños, B. Miralles, N. Acosta*, et al.*, "Functional characterization of chitin and chitosan," *Current Chemical Biology,* vol. 3, pp. 203-230, 2009.

[44] H. Ueno, T. Mori, and T. Fujinaga, "Topical formulations and wound healing applications of chitosan," *Advanced drug delivery reviews,* vol. 52, pp. 105-115, 2001.

[45] N. Peppas, Y. Huang, M. Torres-Lugo, J. Ward, and J. Zhang, "Physicochemical foundations and structural design of hydrogels in medicine and biology," *Annual review of biomedical engineering,* vol. 2, pp. 9-29, 2000.

[46] B. V. Slaughter, S. S. Khurshid, O. Z. Fisher, A. Khademhosseini, and N. A. Peppas, "Hydrogels in regenerative medicine," *Advanced Materials,* vol. 21, pp. 3307-3329, 2009.

[47] N. Bhattarai, J. Gunn, and M. Zhang, "Chitosan-based hydrogels for controlled, localized drug delivery," *Advanced drug delivery reviews,* vol. 62, pp. 83-99, 2010.

[48] W.-Y. Chuang, T.-H. Young, C.-H. Yao, and W.-Y. Chiu, "Properties of the poly (vinyl alcohol)/chitosan blend and its effect on the culture of fibroblast in vitro," *Biomaterials,* vol. 20, pp. 1479-1487, 1999.

[49] S. Ladet, L. David, and A. Domard, "Multi-membrane hydrogels," *Nature,* vol. 452, pp. 76-79, 2008.

[50] J. Cho, M.-C. Heuzey, A. Bégin, and P. J. Carreau, "Physical gelation of chitosan in the presence of β-glycerophosphate: The effect of temperature," *Biomacromolecules,* vol. 6, pp. 3267-3275, 2005.

[51] M. Hamdine, M.-C. Heuzey, and A. Bégin, "Effect of organic and inorganic acids on concentrated chitosan solutions and gels," *International journal of biological macromolecules,* vol. 37, pp. 134-142, 2005.

[52] F.-L. Mi, C.-Y. Kuan, S.-S. Shyu, S.-T. Lee, and S.-F. Chang, "The study of gelation kinetics and chain-relaxation properties of glutaraldehyde-cross-linked chitosan gel and their effects on microspheres preparation and drug release," *Carbohydrate Polymers,* vol. 41, pp. 389-396, 2000.

[53] E. S. Dragan, M. M. Perju, and M. V. Dinu, "Preparation and characterization of IPN composite hydrogels based on polyacrylamide and chitosan and their interaction with ionic dyes," *Carbohydrate Polymers,* vol. 88, pp. 270-281, 2012.

[54] R. H. Baughman, A. A. Zakhidov, and W. A. De Heer, "Carbon nanotubes--the route toward applications," *science,* vol. 297, pp. 787-792, 2002.

[55] M. C. Serrano, M. C. Gutiérrez, and F. del Monte, "Role of polymers in the design of 3D carbon nanotube-based scaffolds for biomedical applications," *Progress in Polymer Science,* vol. 39, pp. 1448-1471, 2014.

[56] V. K. Shante and S. Kirkpatrick, "An introduction to percolation theory," *Advances in Physics,* vol. 20, pp. 325-357, 1971.

[57] N. Grossiord, J. Loos, L. Van Laake, M. Maugey, C. Zakri, C. E. Koning*, et al.*, "High‐Conductivity Polymer Nanocomposites Obtained by Tailoring the Characteristics of Carbon Nanotube Fillers," *Advanced Functional Materials,* vol. 18, pp. 3226-3234, 2008.

[58] S. Z. Guo, K. Qiu, F. Meng, S. H. Park, and M. C. McAlpine, "3D printed stretchable tactile sensors," *Advanced Materials,* vol. 29, 2017.

[59] Y. Chen, H. B. Zhang, Y. Yang, M. Wang, A. Cao, and Z. Z. Yu, "High‐Performance Epoxy Nanocomposites Reinforced with Three‐Dimensional Carbon Nanotube Sponge for Electromagnetic Interference Shielding," *Advanced Functional Materials,* vol. 26, pp. 447-455, 2016.

[60] H.-P. Chang, H.-C. Liu, and C.-S. Tan, "Using supercritical CO2-assisted mixing to prepare graphene/carbon nanotube/epoxy nanocomposites," *Polymer,* vol. 75, pp. 125-133, 2015.

[61] G.-W. Huang, H.-M. Xiao, and S.-Y. Fu, "Electrical switch for smart pH self-adjusting system based on silver nanowire/polyaniline nanocomposite film," *ACS nano,* vol. 9, pp. 3234-3242, 2015.

[62] R. Xiong, K. Hu, A. M. Grant, R. Ma, W. Xu, C. Lu*, et al.*, "Ultrarobust Transparent Cellulose Nanocrystal‐Graphene Membranes with High Electrical Conductivity," *Advanced Materials,* vol. 28, pp. 1501-1509, 2016.

[63] E. B. Secor, B. Y. Ahn, T. Z. Gao, J. A. Lewis, and M. C. Hersam, "Rapid and versatile photonic annealing of graphene inks for flexible printed electronics," *Advanced Materials,* vol. 27, pp. 6683-6688, 2015.

[64] C. Li, J. Adamcik, and R. Mezzenga, "Biodegradable nanocomposites of amyloid fibrils and graphene with shape-memory and enzyme-sensing properties," *Nature Nanotechnology,* vol. 7, p. 421, 2012.

[65] H. Nassira, A. Sánchez‐Ferrer, J. Adamcik, S. Handschin, H. Mahdavi, N. Taheri Qazvini*, et al.*, "Gelatin–Graphene nanocomposites with ultralow electrical percolation threshold," *Advanced Materials,* vol. 28, pp. 6914-6920, 2016.

[66] L. Lu and W. Chen, "Biocompatible composite actuator: a supramolecular structure consisting of the biopolymer chitosan, carbon nanotubes, and an ionic liquid," *Advanced Materials,* vol. 22, pp. 3745-3748, 2010.

[67] Y. Hu, W. Chen, L. Lu, J. Liu, and C. Chang, "Electromechanical actuation with controllable motion based on a single-walled carbon nanotube and natural biopolymer composite," *ACS nano,* vol. 4, pp. 3498-3502, 2010.

[68] H.-L. Gao, Y.-B. Zhu, L.-B. Mao, F.-C. Wang, X.-S. Luo, Y.-Y. Liu*, et al.*, "Super-elastic and fatigue resistant carbon material with lamellar multi-arch microstructure," *Nature communications,* vol. 7, p. 12920, 2016.

[69] M. K. Shin, J. Oh, M. Lima, M. E. Kozlov, S. J. Kim, and R. H. Baughman, "Elastomeric conductive composites based on carbon nanotube forests," *Advanced materials,* vol. 22, pp. 2663-2667, 2010.

[70] R. Saito, G. Dresselhaus, and M. S. Dresselhaus, *Physical properties of carbon nanotubes*: World Scientific, 1998.

[71] P. M. Ajayan and O. Z. Zhou, "Applications of carbon nanotubes," in *Carbon nanotubes*, ed: Springer, 2001, pp. 391-425.

[72] D. Qian, G. J. Wagner, W. K. Liu, M.-F. Yu, and R. S. Ruoff, "Mechanics of carbon nanotubes," *Applied mechanics reviews,* vol. 55, pp. 495-533, 2002.

[73] O. Lourie and H. Wagner, "Evaluation of Young's modulus of carbon nanotubes by micro-Raman spectroscopy," *Journal of Materials Research,* vol. 13, pp. 2418-2422, 1998.

[74] P.-C. Ma, N. A. Siddiqui, G. Marom, and J.-K. Kim, "Dispersion and functionalization of carbon nanotubes for polymer-based nanocomposites: a review," *Composites Part A: Applied Science and Manufacturing,* vol. 41, pp. 1345-1367, 2010.

[75] X. Chen, M. A. Dam, K. Ono, A. Mal, H. Shen, S. R. Nutt*, et al.*, "A thermally re-mendable cross-linked polymeric material," *Science,* vol. 295, pp. 1698-1702, 2002.

[76]   Y. Amamoto, H. Otsuka, A. Takahara, and K. Matyjaszewski, "Self‑healing of covalently cross‑linked polymers by reshuffling thiuram disulfide moieties in air under visible light," *Advanced Materials,* vol. 24, pp. 3975-3980, 2012.

[77]   M. Noack, R. Merindol, B. Zhu, A. Benitez, S. Hackelbusch, F. Beckert, *et al.*, "Light‑Fueled, Spatiotemporal Modulation of Mechanical Properties and Rapid Self‑Healing of Graphene‑Doped Supramolecular Elastomers," *Advanced Functional Materials,* vol. 27, 2017.

[78]   B. J. Blaiszik, S. L. Kramer, S. C. Olugebefola, J. S. Moore, N. R. Sottos, and S. R. White, "Self-healing polymers and composites," *Annual Review of Materials Research,* vol. 40, pp. 179-211, 2010.

[79]   S. R. White, N. Sottos, P. Geubelle, J. Moore, M. R. Kessler, S. Sriram, *et al.*, "Autonomic healing of polymer composites," *Nature,* vol. 409, pp. 794-797, 2001.

[80]   K. Miyamae, M. Nakahata, Y. Takashima, and A. Harada, "Self‑Healing, Expansion–Contraction, and Shape‑Memory Properties of a Preorganized Supramolecular Hydrogel through Host–Guest Interactions," *Angewandte Chemie International Edition,* vol. 54, pp. 8984-8987, 2015.

[81]   M. Diba, H. Wang, T. E. Kodger, S. Parsa, and S. C. Leeuwenburgh, "Highly Elastic and Self‑Healing Composite Colloidal Gels," *Advanced Materials,* vol. 29, 2017.

[82]   Z. Wei, J. H. Yang, Z. Q. Liu, F. Xu, J. X. Zhou, M. Zrínyi, *et al.*, "Novel Biocompatible Polysaccharide‑Based Self‑Healing Hydrogel," *Advanced Functional Materials,* vol. 25, pp. 1352-1359, 2015.

[83]   S. A. Odom, S. Chayanupatkul, B. J. Blaiszik, O. Zhao, A. C. Jackson, P. V. Braun, *et al.*, "A Self‑healing Conductive Ink," *Advanced Materials,* vol. 24, pp. 2578-2581, 2012.

[84]   Y. Cao, T. G. Morrissey, E. Acome, S. I. Allec, B. M. Wong, C. Keplinger, *et al.*, "A Transparent, Self‑Healing, Highly Stretchable Ionic Conductor," *Advanced Materials,* vol. 29, 2017.

[85]   E. D'Elia, S. Barg, N. Ni, V. G. Rocha, and E. Saiz, "Self‑Healing Graphene‑Based Composites with Sensing Capabilities," *Advanced Materials,* vol. 27, pp. 4788-4794, 2015.

[86]   C. Ji, N. Annabi, A. Khademhosseini, and F. Dehghani, "Fabrication of porous chitosan scaffolds for soft tissue engineering using dense gas CO< sub> 2</sub>," *Acta Biomaterialia,* vol. 7, pp. 1653-1664, 2011.

[87]   S. W. Choi, J. Xie, and Y. Xia, "Chitosan‑Based Inverse Opals: Three‑Dimensional Scaffolds with Uniform Pore Structures for Cell Culture," *Advanced materials,* vol. 21, pp. 2997-3001, 2009.

[88]   M. Pakravan, M.-C. Heuzey, and A. Ajji, "Core–shell structured PEO-chitosan nanofibers by coaxial electrospinning," *Biomacromolecules,* vol. 13, pp. 412-421, 2012.

[89]   B. Subia, J. Kundu, and S. Kundu, "Biomaterial scaffold fabrication techniques for potential tissue engineering applications," *Tissue engineering,* vol. 524, 2010.

[90] H. H. Xu and C. G. Simon Jr, "Fast setting calcium phosphate–chitosan scaffold: mechanical properties and biocompatibility," *Biomaterials,* vol. 26, pp. 1337-1348, 2005.

[91] H. Yamada and F. G. Evans, "Strength of biological materials," 1970.

[92] J. A. Genovese, C. Spadaccio, A. Rainer, and E. Covino, "Electrospun nanocomposites and stem cells in cardiac tissue engineering," in *Myocardial Tissue Engineering*, ed: Springer, 2011, pp. 215-242.

[93] R. James, U. S. Toti, C. T. Laurencin, and S. G. Kumbar, "Electrospun nanofibrous scaffolds for engineering soft connective tissues," in *Biomedical Nanotechnology*, ed: Springer, 2011, pp. 243-258.

[94] M. Pakravan, M.-C. Heuzey, and A. Ajji, "A fundamental study of chitosan/PEO electrospinning," *Polymer,* vol. 52, pp. 4813-4824, 2011.

[95] S. Heydarkhan-Hagvall, K. Schenke-Layland, A. P. Dhanasopon, F. Rofail, H. Smith, B. M. Wu*, et al.*, "Three-dimensional electrospun ECM-based hybrid scaffolds for cardiovascular tissue engineering," *Biomaterials,* vol. 29, pp. 2907-2914, 2008.

[96] R. Ravichandran, J. R. Venugopal, S. Sundarrajan, S. Mukherjee, R. Sridhar, and S. Ramakrishna, "Minimally invasive injectable short nanofibers of poly (glycerol sebacate) for cardiac tissue engineering," *Nanotechnology,* vol. 23, p. 385102, 2012.

[97] R. L. Truby and J. A. Lewis, "Printing soft matter in three dimensions," *Nature,* vol. 540, p. 371, 2016.

[98] D. B. Kolesky, R. L. Truby, A. S. Gladman, T. A. Busbee, K. A. Homan, and J. A. Lewis, "3D bioprinting of vascularized, heterogeneous cell‑laden tissue constructs," *Advanced materials,* vol. 26, pp. 3124-3130, 2014.

[99] J. T. Muth, D. M. Vogt, R. L. Truby, Y. Mengüç, D. B. Kolesky, R. J. Wood*, et al.*, "Embedded 3D printing of strain sensors within highly stretchable elastomers," *Advanced Materials,* vol. 26, pp. 6307-6312, 2014.

[100] B. G. Compton and J. A. Lewis, "3D‑printing of lightweight cellular composites," *Advanced materials,* vol. 26, pp. 5930-5935, 2014.

[101] L. L. Lebel, B. Aissa, M. A. E. Khakani, and D. Therriault, "Ultraviolet‑Assisted Direct‑Write Fabrication of Carbon Nanotube/Polymer Nanocomposite Microcoils," *Advanced Materials,* vol. 22, pp. 592-596, 2010.

[102] H. Lee and G. Kim, "Cryogenically fabricated three-dimensional chitosan scaffolds with pore size-controlled structures for biomedical applications," *Carbohydrate polymers,* vol. 85, pp. 817-823, 2011.

[103] H. Tao, B. Marelli, M. Yang, B. An, M. S. Onses, J. A. Rogers*, et al.*, "Inkjet printing of regenerated silk fibroin: From printable forms to printable functions," *Advanced Materials,* vol. 27, pp. 4273-4279, 2015.

[104] Y. Gu, W. Zhang, H. Wang, and W. Y. Lee, "Chitosan surface enhances the mobility, cytoplasm spreading, and phagocytosis of macrophages," *Colloids and Surfaces B: Biointerfaces,* vol. 117, pp. 42-50, 2014.

[105] T. Boland, T. Xu, B. Damon, and X. Cui, "Application of inkjet printing to tissue engineering," *Biotechnology journal,* vol. 1, pp. 910-917, 2006.

[106] P. L. Lewis, R. M. Green, and R. N. Shah, "3D-Printed Gelatin Scaffolds of Differing Pore Geometry Modulate Hepatocyte Function and Gene Expression," *Acta biomaterialia,* 2018.

[107] A. L. Rutz, K. E. Hyland, A. E. Jakus, W. R. Burghardt, and R. N. Shah, "A Multimaterial Bioink Method for 3D Printing Tunable, Cell‐Compatible Hydrogels," *Advanced Materials,* vol. 27, pp. 1607-1614, 2015.

[108] G. Siqueira, D. Kokkinis, R. Libanori, M. K. Hausmann, A. S. Gladman, A. Neels*, et al.*, "Cellulose nanocrystal inks for 3D printing of textured cellular architectures," *Advanced Functional Materials,* vol. 27, 2017.

[109] M. R. Sommer, M. Schaffner, D. Carnelli, and A. R. Studart, "3D printing of hierarchical silk fibroin structures," *ACS applied materials & interfaces,* vol. 8, pp. 34677-34685, 2016.

[110] L. Ouyang, C. B. Highley, C. B. Rodell, W. Sun, and J. A. Burdick, "3D printing of shear-thinning hyaluronic acid hydrogels with secondary cross-linking," *ACS Biomaterials Science & Engineering,* vol. 2, pp. 1743-1751, 2016.

[111] Q. Wu, M. Maire, S. Lerouge, D. Therriault, and M. C. Heuzey, "3D printing of microstructured and stretchable chitosan hydrogel for guided cell growth," *Advanced Biosystems,* vol. 1, 2017.

[112] T. H. Van Osch, J. Perelaer, A. W. de Laat, and U. S. Schubert, "Inkjet printing of narrow conductive tracks on untreated polymeric substrates," *Advanced Materials,* vol. 20, pp. 343-345, 2008.

[113] P. Calvert, "Inkjet printing for materials and devices," *Chemistry of materials,* vol. 13, pp. 3299-3305, 2001.

[114] D. F. D. Campos, A. Blaeser, M. Weber, J. Jäkel, S. Neuss, W. Jahnen-Dechent*, et al.*, "Three-dimensional printing of stem cell-laden hydrogels submerged in a hydrophobic high-density fluid," *Biofabrication,* vol. 5, p. 015003, 2013.

[115] K. Chizari, M. Arjmand, Z. Liu, U. Sundararaj, and D. Therriault, "Three-dimensional printing of highly conductive polymer nanocomposites for EMI shielding applications," *Materials Today Communications,* vol. 11, pp. 112-118, 2017.

[116] M. Gou, X. Qu, W. Zhu, M. Xiang, J. Yang, K. Zhang*, et al.*, "Bio-inspired detoxification using 3D-printed hydrogel nanocomposites," *Nature communications,* vol. 5, p. 3774, 2014.

[117] H. Chung and S. Das, "Functionally graded Nylon-11/silica nanocomposites produced by selective laser sintering," *Materials Science and Engineering: A,* vol. 487, pp. 251-257, 2008.

[118] S. R. Shin, R. Farzad, A. Tamayol, V. Manoharan, P. Mostafalu, Y. S. Zhang*, et al.*, "A Bioactive Carbon Nanotube‐Based Ink for Printing 2D and 3D Flexible Electronics," *Advanced Materials,* vol. 28, pp. 3280-3289, 2016.

[119] R. Liao, O. Pfister, M. Jain, and F. Mouquet, "The bone marrow—cardiac axis of myocardial regeneration," *Progress in cardiovascular diseases,* vol. 50, pp. 18-30, 2007.

[120] M. Gnecchi, H. He, N. Noiseux, O. D. Liang, L. Zhang, F. Morello, *et al.*, "Evidence supporting paracrine hypothesis for Akt-modified mesenchymal stem cell-mediated cardiac protection and functional improvement," *The FASEB Journal,* vol. 20, pp. 661-669, 2006.

[121] T. Shin'oka, G. Matsumura, N. Hibino, Y. Naito, M. Watanabe, T. Konuma, *et al.*, "Midterm clinical result of tissue-engineered vascular autografts seeded with autologous bone marrow cells," *The Journal of thoracic and cardiovascular surgery,* vol. 129, pp. 1330-1338, 2005.

[122] M. B. Pabbruwe, W. Kafienah, J. F. Tarlton, S. Mistry, D. J. Fox, and A. P. Hollander, "Repair of meniscal cartilage white zone tears using a stem cell/collagen-scaffold implant," *Biomaterials,* vol. 31, pp. 2583-2591, 2010.

[123] V. F. Segers and R. T. Lee, "Stem-cell therapy for cardiac disease," *Nature,* vol. 451, pp. 937-942, 2008.

[124] T. Eschenhagen and W. H. Zimmermann, "Engineering myocardial tissue," *Circulation research,* vol. 97, pp. 1220-1231, 2005.

[125] J. Westrich, P. Yaeger, C. He, J. Stewart, R. Chen, G. Seleznik, *et al.*, "Factors affecting residence time of mesenchymal stromal cells (MSC) injected into the myocardium," *Cell transplantation,* vol. 19, pp. 937-948, 2010.

[126] M. A. Laflamme and C. E. Murry, "Regenerating the heart," *Nature biotechnology,* vol. 23, pp. 845-856, 2005.

[127] C. A. DeForest and K. S. Anseth, "Advances in bioactive hydrogels to probe and direct cell fate," *Annual review of chemical and biomolecular engineering,* vol. 3, pp. 421-444, 2012.

[128] N. B. Shelke, R. James, C. T. Laurencin, and S. G. Kumbar, "Polysaccharide biomaterials for drug delivery and regenerative engineering," *Polymers for Advanced Technologies,* vol. 25, pp. 448-460, 2014.

[129] S. Van Vlierberghe, P. Dubruel, and E. Schacht, "Biopolymer-based hydrogels as scaffolds for tissue engineering applications: a review," *Biomacromolecules,* vol. 12, pp. 1387-1408, 2011.

[130] S. Pok, J. D. Myers, S. V. Madihally, and J. G. Jacot, "A multilayered scaffold of a chitosan and gelatin hydrogel supported by a PCL core for cardiac tissue engineering," *Acta biomaterialia,* vol. 9, pp. 5630-5642, 2013.

[131] N.-H. Chi, M.-C. Yang, T.-W. Chung, N.-K. Chou, and S.-S. Wang, "Cardiac repair using chitosan-hyaluronan/silk fibroin patches in a rat heart model with myocardial infarction," *Carbohydrate polymers,* vol. 92, pp. 591-597, 2013.

[132] M. N. Ravi Kumar, "A review of chitin and chitosan applications," *Reactive and functional polymers,* vol. 46, pp. 1-27, 2000.

[133] S. Dumitriu, "Polysaccharides as biomaterials," *Polymeric biomaterials,* pp. 1-61, 2001.

[134] H. Wang, X. Zhang, Y. Li, Y. Ma, Y. Zhang, Z. Liu, *et al.*, "Improved myocardial performance in infarcted rat heart by co-injection of basic fibroblast growth factor with temperature-responsive chitosan hydrogel," *The Journal of Heart and Lung Transplantation,* vol. 29, pp. 881-887, 2010.

[135] Q.-Z. Chen, S. E. Harding, N. N. Ali, A. R. Lyon, and A. R. Boccaccini, "Biomaterials in cardiac tissue engineering: ten years of research survey," *Materials Science and Engineering: R: Reports,* vol. 59, pp. 1-37, 2008.

[136] M. M. AYGEN and E. BRAUNWALD, "Studies on Starling's Law of the Heart VIII. Mechanical Properties of Human Myocardium Studied in Vivo," *Circulation,* vol. 26, pp. 516-524, 1962.

[137] S. J. Hollister, "Porous scaffold design for tissue engineering," *Nature materials,* vol. 4, pp. 518-524, 2005.

[138] G. C. Engelmayr, M. Cheng, C. J. Bettinger, J. T. Borenstein, R. Langer, and L. E. Freed, "Accordion-like honeycombs for tissue engineering of cardiac anisotropy," *Nature materials,* vol. 7, pp. 1003-1010, 2008.

[139] J. Guan, K. L. Fujimoto, and W. R. Wagner, "Elastase-sensitive elastomeric scaffolds with variable anisotropy for soft tissue engineering," *Pharmaceutical research,* vol. 25, pp. 2400-2412, 2008.

[140] E. Kang, Y. Y. Choi, S. K. Chae, J. H. Moon, J. Y. Chang, and S. H. Lee, "Microfluidic spinning of flat alginate fibers with grooves for cell‐aligning scaffolds," *Advanced Materials,* vol. 24, pp. 4271-4277, 2012.

[141] A. Chen, D. K. Lieu, L. Freschauf, V. Lew, H. Sharma, J. Wang*, et al.*, "Shrink‐film configurable multiscale wrinkles for functional alignment of human embryonic stem cells and their cardiac derivatives," *Advanced Materials,* vol. 23, pp. 5785-5791, 2011.

[142] J. Cao, C. Lu, J. Zhuang, M. Liu, X. Zhang, Y. Yu*, et al.*, "Multiple Hydrogen Bonding Enables the Self‐Healing of Sensors for Human‐Machine Interactions," *Angewandte Chemie,* vol. 129, pp. 8921-8926, 2017.

[143] Y. He, S. Liao, H. Jia, Y. Cao, Z. Wang, and Y. Wang, "A Self‐Healing Electronic Sensor Based on Thermal‐Sensitive Fluids," *Advanced Materials,* vol. 27, pp. 4622-4627, 2015.

[144] M. Amjadi, A. Pichitpajongkit, S. Lee, S. Ryu, and I. Park, "Highly stretchable and sensitive strain sensor based on silver nanowire–elastomer nanocomposite," *ACS nano,* vol. 8, pp. 5154-5163, 2014.

[145] Y. Qin, Q. Peng, Y. Ding, Z. Lin, C. Wang, Y. Li*, et al.*, "Lightweight, superelastic, and mechanically flexible graphene/polyimide nanocomposite foam for strain sensor application," *ACS nano,* vol. 9, pp. 8933-8941, 2015.

[146] G. Zhou, J.-H. Byun, Y. Oh, B.-M. Jung, H.-J. Cha, D.-G. Seong*, et al.*, "Highly sensitive wearable textile-based humidity sensor made of high-strength, single-walled carbon nanotube/poly (vinyl alcohol) filaments," *ACS applied materials & interfaces,* vol. 9, pp. 4788-4797, 2017.

[147] S. Ling, Z. Qin, C. Li, W. Huang, D. L. Kaplan, and M. J. Buehler, "Polymorphic regenerated silk fibers assembled through bioinspired spinning," *Nature communications,* vol. 8, p. 1387, 2017.

[148] S. Abdulla, T. L. Mathew, and B. Pullithadathil, "Highly sensitive, room temperature gas sensor based on polyaniline-multiwalled carbon nanotubes (PANI/MWCNTs)

nanocomposite for trace-level ammonia detection," *Sensors and Actuators B: Chemical,* vol. 221, pp. 1523-1534, 2015.

[149] Y. Yang, B. Zhu, D. Yin, J. Wei, Z. Wang, R. Xiong*, et al.*, "Flexible self-healing nanocomposites for recoverable motion sensor," *Nano Energy,* vol. 17, pp. 1-9, 2015.

[150] L. Kou, T. Huang, B. Zheng, Y. Han, X. Zhao, K. Gopalsamy*, et al.*, "Coaxial wet-spun yarn supercapacitors for high-energy density and safe wearable electronics," *Nature communications,* vol. 5, 2014.

[151] A. Ambrosi, J. G. S. Moo, and M. Pumera, "Helical 3D‑Printed Metal Electrodes as Custom‑Shaped 3D Platform for Electrochemical Devices," *Advanced Functional Materials,* vol. 26, pp. 698-703, 2016.

[152] H. Cheng, Y. Huang, Q. Cheng, G. Shi, L. Jiang, and L. Qu, "Self‑Healing Graphene Oxide Based Functional Architectures Triggered by Moisture," *Advanced Functional Materials,* vol. 27.